SPIN DYNAMICS OF PULSED NUCLEAR MAGNETIC DOUBLE RESONANCE IN SOLIDS

Thesis by

Michael Edward Stoll

In Partial Fulfillment of the Requirements

for the Degree of

Doctor of Philosophy

California Institute of Technology

Pasadena, California

1977

(Submitted May 16, 1977)

to my Mother

ACKNOWLEDGEMENTS

There are so many people to whom I am indebted, and I would like to express my sincerest appreciation to at least a few of them.

In particular, I would like to thank my advisor, Professor Robert W. Vaughan. He is a scientist of rare abilities, and it has been a pleasure knowing him, both in and out of the lab. His unbounded enthusiasm and talent have always served as a source of motivation, yet he has always taken great care to encourage creativity and given me the freedom to pursue ideas. I hope some measure of his successful approach to science has rubbed off on me.

Also let me extend my warmest appreciation to Dr. Alexander Vega. His collaboration on much of the work in this thesis was truly invaluable, and our many discussions, both scientific and otherwise, have been a real source of enjoyment.

I am indeed fortunate to have known Dr. Loren Schreiber. By his many probing questions and from many stimulating discussions with him, he taught me how to distill out the essentials of scientific problems. Also, let me thank Dr. Won Kyu Rhim for teaching me some of the fine art of multiple pulse spectroscopy during the time I spent with him at JPL. It has been a real pleasure to have Martin Chen as my close friend. Our numerous discussions till the wee hours of the morning will long be remembered.

My thanks go to John Yehle, also, for the excellent job he has done in designing and building much of the electronic equipment used for the experiments in this thesis. He is very representative of the

outstanding and friendly support personnel all over Caltech, who make the pursuit of science much easier and quite pleasant.

Let me also thank the rest of the Vaughan research group who have provided many stimulating ideas and good companionship during my stay here. Also, I particularly thank Sharon ViGario and Kathy Lewis, who typed this thesis.

A special word of thanks goes to my mother, who has always acted selflessly to make this a reality. Let me especially thank my fiancé, Vicki, who has at all times been patient, encouraging, and supportive.

Finally, I thank the California Institute of Technology for all of its financial support, but more importantly for providing me with the the proper environment in which to learn about and marvel at the wonder and the beauty of Physics.

ABSTRACT

In the first part of this thesis, experiments utilizing an NMR phase interferometric concept are presented. The spinor character of two-level systems is explicitly demonstrated by using this concept. Following this is the presentation of an experiment which uses this same idea to measure relaxation times of off-diagonal density matrix elements corresponding to magnetic-dipole-forbidden transitions in a ^{13}C-^{1}H, AX spin system. The theoretical background for these experiments and the spin dynamics of the interferometry are discussed also.

The second part of this thesis deals with NMR dipolar modulated chemical shift spectroscopy, with which internuclear bond lengths and bond angles with respect to the chemical shift principal axis frame are determined from polycrystalline samples. Experiments using benzene and calcium formate verify the validity of the technique in heteronuclear (^{13}C-^{1}H) systems. Similar experiments on powdered trichloroacetic acid confirm the validity in homonuclear (^{1}H-^{1}H) systems. The theory and spin dynamics are explored in detail, and the effects of a number of multiple pulse sequences are discussed.

The last part deals with an experiment measuring the ^{13}C chemical shift tensor in $K_2Pt(CN)_4Br_{0.3}\cdot 3H_2O$, a one-dimensional conductor. The ^{13}C spectra are strongly affected by ^{14}N quadrupolar interactions via the ^{13}C-^{14}N dipolar interaction. Single crystal rotation spectra are shown.

An appendix discussing the design, construction, and performance of a single-coil double resonance NMR sample probe is included.

TABLE OF CONTENTS

CHAPTER 1

GENERAL INTRODUCTION

Since its inception at the close of the Second World War, nuclear magnetic resonance (NMR) has been enormously successful both as a research tool and as an analytical tool in studies of liquids. This is primarily due to the observation of the effects of three interactions. The first is the Zeeman interaction, in which we place our sample containing the nuclei of spin I to be studied into a strong magnetic field, and the energy levels of the spin I are split into an equally spaced manifold of 2I + 1 levels. By applying radiation at the frequency corresponding to the energy difference of adjacent levels, we can cause transitions and hence do NMR spectroscopy. This characteristic frequency, called the Larmor frequency, is equal to $\gamma_I H_o$ (in radians per second), where γ_I is the magnetogyric ratio of the I spin and H_o is the strength of the magnetic field. The second interaction is the so-called chemical shift interaction, in which the I spins feel also the weak magnetic fields created by electron currents in the sample, thus slightly altering the effective resonant frequency of the I spins in a way characteristic of the particular solution being studied. The third interaction is the scalar or "J" coupling, in which our spin I interacts indirectly with another spin S through a quantum mechanical exchange interaction of a pair of shared electrons. This causes the NMR spectroscopic lines to be split characteristically of the particular sample, depending on which spins I are near to which spins S in the sample. These three interactions together can often serve to "fingerprint" a molecule, thus making liquid NMR a powerful analytical tool. In addition, by observing the characteristic times required by systems prepared in non-equilibrium states to relax to equilibrium (T_1, T_2, $T_{1\rho}$, etc.), investigators have been able to study random effects

such as molecular motions in the sample.

Unfortunately the successes of solid state NMR spectroscopy have not come so easily. The main problem is that there are other interactions in solids which effectively overwhelm the smaller chemical shift interaction. The primary offenders here are the direct nuclear dipole-dipole interaction and the quadrupole interaction. In the former we have a nucleus I interacting with the magnetic field created by another spin S. This effect is often orders of magnitude larger than the chemical shift effects. In the latter we have the quadrupole moment of a spin $I(I>\frac{1}{2})$ interacting with the gradients in the local electric field. This effect is usually an order of magnitude or more larger than the dipole-dipole interaction. In liquids both of these interactions are averaged to zero as the molecules and ions containing the spins tumble about randomly with characteristic times $\sim 10^{-11}$ sec. However, in solids where the nuclei are, for the most part, "nailed" in place, these effects give rise to broad, featureless lines which yield little information. However, if ways are devised to selectively either remove or utilize these larger interactions, the NMR studies of solids can provide information not even obtainable from NMR in liquids. For instance, the chemical shift interaction is known to be a tensor interaction, but due to the motion in liquids the only information available there is the trace of the tensor. In solids, contrastingly, all three principal components of the tensor are obtainable.

From the early 1950's to the late 1960's pioneering work was done in developing sample spinning [1, 2], continuous wave (CW) [3], and multiple pulse (MP) [4] techniques to remove interactions having the symmetry of the homonuclear dipole-dipole interaction, thus making it possible to narrow

the spectroscopic lines in solids by orders of magnitude. The MP techniques were even further refined [5], and the resulting linewidths decreased by another order of magnitude. Similar methods had been developed [6, 7] and were being perfected [8] which were useful in narrowing the NMR lines in solids which were broadened by heteronuclear dipole-dipole interactions. All of these techniques in solids were aimed at effectively removing or "averaging out" these larger dipole interactions in order to see the smaller chemical shift effects. Then, however, the concept was pursued of not just eliminating, but rather utilizing the dipole-dipole interaction quantitatively to obtain chemical shift information. This is where the present work of the author and collaborators comes into play. We have continued the progress by developing experiments designed to use the dipole-dipole interaction to effectively modulate the chemical shift interaction, thus allowing us to get at structural and perhaps motional parameters in polycrystalline solids. In the course of pursuing this research, we were carefully scrutinizing the dynamics of spin ½ systems in general, and out of this came a new generation of experiments which capitalize on often overlooked phase coherence in spin systems. These later techniques are applicable to liquids as well as solids, so in some sense this research has come full circle. The main common denominators of all the work in this thesis are the attempt to develop new insights into the dynamics of spin systems (basically spin ½) and the use of NMR to devise novel and potentially very useful methods of investigating materials. In all cases we have relied heavily on the strong scientific foundation laid by so many workers in the field of NMR over the years.

The work summarized in this thesis is divided into basically three parts. Although these parts were chronologically developed in reverse order, for

purposes of pedagogy they will presented as they are in this thesis.

The first part of the thesis, Chapters 2, 3, and 4, although developed most recently will be discussed first because it embodies in some ways the most simple and basic of the concepts in this thesis. It deals with a nuclear magnetic double resonance technique which utilizes phase interferometric spectroscopy. Essentially this means merely creating quantum mechanical phase coherence between two quantum states by irradiation at one frequency and then altering this phase coherence by application of radiation at a second frequency. In most double resonance experiments, the application of radiation to the second frequency is done in order to change the populations of the levels from the thermal equilibrium values [9] or to alter the actual energy level structure in a rotating frame [10]. Yet none of these conventional double resonance techniques makes use of phase information, thus ignoring a very important part of the quantum mechanics of spin systems. By utilizing this phase information we have been able to study the fundamental behavior under rotation of half-integral spin particles, as well as studying relaxation rates which are not normally seen. We feel also that this technique could be used to detect spins with low magnetogyric ratios, as well as having a number of other applications to spectroscopy.

In Chapter 2 the simple theoretical basis for this phase interferometry is briefly presented. Chapter 3 gives the results of an experiment designed to show the spinor character of a spin ½ nucleus using this same technique. This same experimental technique is again used in Chapter 4 to investigate the relaxation rates of transverse phase coherence corresponding to forbidden

transitions. This may prove to be a way to measure cross-correlations between fluctuating fields at different nuclear sites.

The second part of the thesis, Chapters 5 - 8, deals with a technique called dipolar modulation chemical shift spectroscopy. In this technique we allow the dipole interaction between spins to act for a time, τ, and then observe the conventional solid state chemical shift spectrum undulating predictably. Since both the chemical shift and dipolar interactions are orientationally dependent, we can actually determine structural information in polycrystalline materials. This eliminates the necessity of having single crystal samples and makes it possible to use NMR to obtain geometrical and perhaps motional information in such systems as catalysts and polymers, where there may be no long range ordering.

In Chapter 5 the general theoretical background for the dipolar modulated chemical shift experiments is presented. Both heteronuclear and homonuclear dipole interactions are considered, and a number of different MP cycles and their subsequent effects are discussed. Chapter 6 presents the results of the first examples of transfer of spin polarization under pulsed cycles. These experiments were the predecessors of the dipolar modulated experiments and gave the first indication of how to generalize the concept of the Hartmann-Hahn double resonance matching conditons [11] to pulsed experiments. In Chapter 7, Part One, we present the results of experiments on $^{13}C-^{1}H$ systems of polycrystalline benzene and calcium formate which demonstrate the feasibility of the heteronuclear dipolar modulated chemical shift technique. Chapter 7, Part Two, deals with further refinements on the benzene theoretical work and a way to get internuclear distances by using only

areas of spectra. Chapter 8 presents the results of an experiment utilizing homonuclear modulation of chemical shift spectra. This experiment, done in a polycrystalline sample of trichloracetic acid (TCAA), uses dipolar interactions between ^{1}H (proton) pairs to obtain structural information.

The third and final part of the thesis, Chapter 9, deals with a single crystal experiment in which the heteronuclear ^{13}C–^{14}N interaction was used to obtain chemical shift information in a one-dimensional conductor. The chemical shift, however, could not be determined without also calculating the effects of the ^{14}N quadrupole interaction. This effect should be of extreme importance whenever calculating dipolar effects for spins greater than ½. It should be pointed out here that only this last experiment deals with a spin which is greater than ½. In all of the earlier parts of this thesis, the results, unless explicitly stated as such, are only valid for spin ½ particles.

An appendix is also included which describes the design of the most crucial piece of equipment used in these experiments, a sample probe. This single coil, double resonance probe was specifically designed and built for the experiments described in this thesis.

References

1. E. R. Andrew and R. G. Eades, Proc. Roy. Soc. London, A216, 398 (1953).
2. I. J. Lowe, Phys. Rev. Lett. 2, 285 (1959).
3. M. Lee and W. I. Goldberg, Phys. Rev. A140, 1261 (1965).
4. J. S. Waugh, L. M. Huber, and U. Haeberlen, Phys. Rev. Lett. 20, 180 (1968).
5. W.-K. Rhim, D. D. Elleman, and R. W. Vaughan, J. Chem. Phys. 58, 1772 (1973).
6. L. R. Sarles and R. M. Cotts, Phys. Rev. 111, 853 (1958).
7. M. Mehring, A. Pines, W.-K. Rhim, and J. S. Waugh, J. Chem. Phys. 54 3239 (1971).
8. A. Pines, M. G. Gibby, and J. S. Waugh, J. Chem. Phys. 59, 569 (1973).
9. A. W. Overhauser, Phys. Rev. 89, 689 (1953).
10. R. Freeman and W. A. Anderson, J. Chem. Phys. 37, 2053 (1962).
11. S. R. Hartmann and E. L. Hahn, Phys. Rev. 128, 2042 (1962).

CHAPTER 2

BASIC THEORY FOR THE PHASE INTERFEROMETRIC EXPERIMENTS

I. INTRODUCTION

In this chapter we present very briefly the theory behind the phase interferometric experiments of Chapters 3 and 4. Actually, the underlying principles are explained in great detail in those chapters, so we shall concentrate here not on minor points, but rather on the one fundamental, simple concept that the experiments employ: the manipulation of quantum mechanical phase, and its subsequent detection through interferometry. Chapter 3 and 4 approach the theory with a density matrix formalism, which is especially well suited for spin systems in statistically mixed states. However, the phase effects we discuss have their origins in quantum probability and not statistical probability. Therefore we present the theory here in a different manner, which is chosen for its pedagogic rather than its pragmatic qualities. This method does not use density matrices, but rather considers the development of a pure state quantum mechanical wave function.

II. The Theory

The "bare-bones" theory requires three quantum mechanicals states, ϕ_1, ϕ_2, and ϕ_3. These states are not degenerate, and the corresponding transition frequencies ω_{12}, ω_{23}, and ω_{13} are all assumed to be inequivalent. We can write a general wavefunction, $\psi(t)$, as

$$\psi(t) = C_1(t)\phi_1 + C_2(t)\phi_2 + C_3(t)\phi_3 \qquad (1)$$

where the $C_i(t)$ are the complex amplitudes of the system to be found in the

various states ϕ_i.

We assume the following initial conditions

$$C_1(0) = 1$$
$$C_2(0) = C_3(0) = 0 \tag{2}$$

which means that at time t = 0, our system is in the state ϕ_1. We now wish to create quantum mechanical phase coherence between levels 1 and 2. This is done by applying radiation at the "resonant" frequency ω_{12}. We are careful in this experiment to not disturb the 1 - 3 or 2 - 3 transitions. For sake of simplicity we assume that this radiation is a 90° pulse, which means that our system now has an equal probability of being found in states ϕ_1 or ϕ_2. Another assumption we are making is that we are in the interaction frame of the main Hamiltonian giving rise to the energy level structure, and thus we will not "see" changes in the wavefunction due to this Hamiltonian. After the 90° pulse, which we assume is short, our "new" initial conditions, indicated by primes, are

$$C_1'(0) = C_2'(0) = \frac{1}{\sqrt{2}}$$
$$C_3'(0) = 0 \tag{3}$$

The system is now in a state which is a linear combination of states ϕ_1 and

ϕ_2. Furthermore, there is a definite phase coherence between these states, and we have chosen the difference in the phases of the two complex amplitudes to be zero. We can perhaps understand this better by noting explicitly that since the C_i are complex numbers, they can be written in the form

$$C_1 = A_1 e^{i\alpha} \tag{4}$$

$$C_2 = A_2 e^{i\beta}$$

$$C_3 = A_3 e^{i\gamma}$$

where the A_i are the strictly real and positive magnitudes of the complex numbers, and the α, β and γ are the phases.

Next we apply a second pulse of radiation to only the 2 - 3 transition, by applying radiation at the frequency ω_{23}. After a time τ of this irradiation our co-efficients are

$$C_1(\tau) = \frac{1}{\sqrt{2}} \tag{5}$$

$$C_2(\tau) = \frac{1}{\sqrt{2}} \cos(\Omega\tau)$$

$$C_3(\tau) = \frac{1}{\sqrt{2}} \sin(\Omega\tau)$$

where Ω is a constant depending on the amplitude and the other details of the radiation. Since application of this second pulse has not changed the phase

of C_1, we can observe the change in the phase of C_2 by comparison of the difference in the phases of C_1 and C_2 at time $t = 0$ and later at time $t = \tau$. Thus we have created phase coherence between levels 1 and 2, and then we have modified that coherence by irradiating the 2 - 3 transition. The coefficient C_1 serves as our reference in the detection of changes in C_2. The basis of all interferometric experiments in physics is that one cannot observe the overall phase of a quantum mechanical wavefunction, but one can observe relative phases of such wavefunctions. The experiments of Chapter 3 and 4 use this effect much more elaborately for a variety of purposes, but at the real heart of it is this one simple concept.

The only other point we should elaborate on is how C_1 is used as a reference to measure changes in C_2. We do this by observing the expectation value of some operator which connects ϕ_1 and ϕ_2. In the experiments of Chapters 3 and 4, this operator is the transverse magnetization; however, in the most general case, any such "off-diagonal" operator could be suitable. (For instance, one can envision optical experiments utilizing the observation of the electric field for the same purpose.) The result is that our expectation value will be proportional to the product $C_1C_2^*$ or its complex conjugate. Thus we actually measure the quantity $A_1A_2 \cos(\alpha - \beta)$, which enables us to see clearly how both the magnitude and phase of C_2 have changed. In the case of Equation 5 this means we are measuring the quantity $\frac{1}{2} \cos(\Omega\tau)$. This leads to linear oscillation of our observable as a function of τ. This linear oscillation, which arises from quantum mechanical probabilities, is seen in the experiments of Chapters 3 and 4, and it should not be confused with linear oscillations in the dipolar modulation experiments discussed in

Chapters 5, 6, 7 and 8, which arise from purely statistical probabilities.

The quintessence of the following two chapters is this one simple phase interferometric concept. We reserve the explanations of the intimate details of the particular experiments for later discussion in those chapters.

CHAPTER 3

EXPLICIT DEMONSTRATION OF SPINOR CHARACTER FOR A SPIN ½ NUCLEUS USING NUCLEAR MAGNETIC DOUBLE RESONANCE PHASE INTERFEROMETRY

(Chapter 3 is essentially an article by M. E. Stoll, A. J. Vega, and R. W. Vaughan, entitled "Explicit Demonstration of Spinor Character for a Spin ½ Nucleus Via NMR Interferometry". This article has been submitted for publication to Physical Review A.)

It has long been known that a particle of half-integral spin (a fermion) exhibits spinor character, which means that it changes the sign of its quantum mechanical wavefunction upon a 2π rotation, and that the phase factor comes back to itself only after a 4π rotation. A particle of integral spin (a boson) does not exhibit this behavior, and its phase factor comes back to itself in a 2π rotation. While any number of experiments done over the years implicitly illustrate this concept, the first explicit demonstration came in 1975 when Werner, et al.[1] clearly showed the spinor nature of neutrons. Such experiments had been suggested and discussed earlier (1967) by Bernstein[2] and by Aharonov and Susskind[3]. We would like to present here the results of a somewhat analogous nuclear magnetic double resonance experiment which graphically shows the spinor character of a spin ½ particle by observing the behavior under rotation of a pseudo-two-level system. A similar technique could easily be used to study spinor character for spin 3/2, 5/2, etc., by observing the behavior under rotation of pseudo-4, 6, etc., level systems. Non-spinor character of spin 1, 2, etc., could be studied by choosing pseudo-3,5, etc., level systems. In addition, this experiment embodies concepts which could be exploited in a variety of spectroscopic areas.

To observe spinor character, one must observe the phase of a wavefunction. However, this is difficult because any measurement involves $\psi^*\psi$, and thus the overall phase is unobservable. The only way for us to "see" the phase is then by some form of interferometry, i.e., by determination of the phase difference between the amplitude to be in the given state and the amplitude to be in some reference state. In order to measure this phase difference we must measure a physical observable whose operator connects these same states, and furthermore, we must initially prepare the system in a linear combination of these states. Thus, it is in the off-diagonal elements of the density matrix that such relative phase information is found and by doing experiments involving such off-diagonal elements that

one can observe spinor character. Many previous experiments involving off-diagonal matrix elements then can be used as implicit evidence of this behavior. For example, the precession of a spin ½ particle in a strong magnetic field furnishes such implicit evidence.

In the neutron experiment of Werner[1], et al., the relative phase information was extracted by splitting a neutron beam into two parts and observing how the diffraction pattern changed upon application of a 2π rotation to one of these parts. The change in the "beating" pattern then signaled the change in the phase. In our experiment we have used the NMR analogue of interferometry. For a spin in a strong magnetic field to have a transverse component of observable magnetization, it must not be in an eigenstate of the Zeeman Hamiltonian. In fact, the direction that the magnetization points in the x-y plane (the external field is assumed along z) is the direct manifestation of the phase difference between the various levels.

For the particular case of a spin ½ particle in a static magnetic field directed along the z-direction, one has a two-level system where the spin wavefunction, ψ, can be written as

$$\psi = a\, e^{i\phi_a}\, \alpha + b\, e^{i\phi_b}\, \beta$$

where α and β are the eigenstates with quantized angular momentum along the z-axis ($+\frac{1}{2}\hbar$ and $-\frac{1}{2}\hbar$, respectively). The complex coefficients, $ae^{i\phi_a}$ and $be^{i\phi_b}$, are amplitudes for eigenstates α and β, respectively, where a and b are chosen as real numbers with the normalization constraint, $a^2 + b^2 = 1$. The z-component of the magnetization is $M_z \propto (a^2 - b^2)$, while the transverse components are $M_x \propto ab\cos(\phi_a - \phi_b)$ and $M_y \propto ab\sin(\phi_a - \phi_b)$, and thus it is apparent that observation of the transverse magnetization furnishes the phase difference,

$\phi_a - \phi_b$, but the absolute phases, i.e., either ϕ_a or ϕ_b, are not determinable. In order to perform the nuclear magnetic interferometric measurement, it is necessary to "split" the spin into two components, each of which is a two-level system and then to selectively perform a rotation on only one part. Then by observing the interference between the two components both before and after the rotation one can determine the overall change in phase of the rotated component simply by using the phase of the unrotated component as a reference. This "splitting" was accomplished in the neutron experiment by splitting the neutron beam and spatially isolating it into two components which could be selectively rotated, and the beams were then spatially recombined to observe the interference. However, in the present experiment it was not necessary to split and isolate the spin spatially since we could use the presence of a second, different, spin to alter slightly the energy levels and thus accomplish the "splitting" energetically, rather than spatially. That is, by choosing a system with coupled pairs of spins, I and S, one naturally has a "split" system of two components; one consisting of the states α and β for the S spin with the I spin in the α eigenstate, and a second component consisting of the eigenstates α and β for the S spin with the I spin in the β eigenstate. The coupling between the I and S spins causes the transition frequencies of the S spin to be different for these two components, and thus it is possible to selectively rotate only one component and observe the interference effects.

The chemical system we chose for the demonstration was 91% ^{13}C-enriched sodium formate ($NaCHO_2$) dissolved in D_2O with a small amount of ^1H impurity. The ^1H (I spin) and ^{13}C (S spin) nuclei in the formate ion form a coupled system of two spin ½ particles, and their energy levels are as shown in Figure 1. The allowed transitions for the ^1H between levels 1-3 and 2-4

are inequivalent due to the presence of the secular part of a scalar coupling of the form $J \underset{\sim}{I} \cdot \underset{\sim}{S}$, where J is the coupling constant. The inequivalent ^{13}C transitions are between levels 1-2 and 3-4. This J coupling splits the spectroscopic lines and thus allows one to selectively irradiate transitions.

The rf pulsing scheme is illustrated in Figure 2. The experiment itself consisted of two parts. In the first part, we took a normal ^{1}H Fourier-transform echo spectrum of our liquid sample. This consisted of applying a short (2 μsec) $\pi/2$ pulse to all the ^{1}H transitions. A short (4 μsec) ^{1}H π pulse was applied at a time ΔT to create a spin echo at time $2\Delta T$ ($t = 0$). This was convenient for reasons to be explained later. The time decay was then recorded from $t = 0$ and Fourier transformed to yield the top spectrum in Figure 3. (Note that in this first part we have irradiated no ^{13}C transitions.) In this ^{1}H spectrum the symmetric doublet results from the scalar coupling between ^{1}H and ^{13}C in the 91% of the formate ions which are isotopically enriched with ^{13}C. The splitting here has a value of $J = 195$ Hz. The small peak at the center of mass of the doublet results from the ^{1}H nuclei in the remaining 9% of the formate ions which contain spinless ^{12}C nuclei. The large peak on the far right results from the ^{1}H nuclei in the small amount of HDO in the D_2O solvent.

In the second part of the experiment we repeated the scheme of the first part but with one important addition. After the initial ^{1}H $\pi/2$ pulse we applied a long ($\tau = 26$ msec) low-power, selective, ^{13}C 2π pulse to only one of the the ^{13}C transitions (the ^{13}C rotating field equaled approximately 10% of the separation of the ^{13}C lines). As before we recorded the spin echo and Fourier transformed it to get the bottom spectrum shown in Figure 3. We can see that the application of the selective 2π pulse to only one of the

^{13}C transitions caused the inversion of the peaks due to the ^{1}H coupled to the ^{13}C in the formate ions. This fact is the direct result of the fact that the ^{13}C is a two-level system and that two-level systems behave as spinors under rotation. (Note that the ^{1}H peaks due to the ^{1}H not coupled to the ^{13}C did not invert.) To understand this, one can refer to the energy level diagram in Figure 1. The effect of the initial $\pi/2$ pulse applied to the ^{1}H 1-3 and 2-4 transitions was to place the ^{1}H spins in linear combinations of the eigenstates spinup and down (α and β) with a definite phase difference between them. This means that one has created linear combinations of the states 1 and 3 and also of the states 2 and 4 (see Figure 1). Let the phases of the amplitudes of the four states be ϕ_1, ϕ_2, ϕ_3, and ϕ_4. The sizes of the ^{1}H doublet peaks are then proportional to $\cos(\phi_1 - \phi_3)$ and $\cos(\phi_2 - \phi_4)$. The phase difference between 1 and 3 and between 2 and 4 was then modified by the application of a selective 2π pulse to only the 3-4 ^{13}C transition. (A 2π pulse on the 3-4 transition is defined in the conventional way as one which causes $\cos(\phi_3 - \phi_4)$ to undergo one full cycle, i.e., $\Delta(\phi_3 - \phi_4) = 2\pi$.) However, one wishes to know by how much ϕ_3 and ϕ_4 have changed individually. Since no radiation was applied to the 1-2 transition, ϕ_1 and ϕ_2 have not been altered, and since the size of the ^{1}H doublet lines are a measure of $\cos(\phi_1 - \phi_3)$ and $\cos(\phi_2 - \phi_4)$, one can use the fact that both ^{1}H spectral lines inverted (see bottom spectrum in Figure 3) to indicate that both ϕ_3 and ϕ_4 have each changed by π, i.e., a clear demonstration of spinor character.

With respect to more minor experimental details, a spin echo was used on the proton system to furnish ^{1}H spectra that could be directly compared. Had we not refocused the ^{1}H magnetization with the π pulse, we could have observed only the portion of the free-induction decay remaining after the end of the rather long, selective pulse applied to the ^{13}C system, and this would have

produced anomalous effects, making comparison of the ^{1}H spectra more complicated. We set the length of the selective ^{13}C pulse experimentally by observing the ^{13}C NMR signal from a different sample containing an unsplit ^{13}C spectrum.

We note that the two peaks of the doublet in the bottom spectrum of Figure 3 do not have quite the same amplitude. This effect does not have a trivial explanation, and it appears that the difference in amplitude is due to relaxation. When a spin system has been prepared in a state not in thermal equilibrium, as ours has been, the various density matrix elements relax with characteristic times. The diagonal elements relax with time constants which are normally called T_1. A recent publication shows a clever way to measure all of these diagonal relaxation times, in the same system as we are using[4]. Off-diagonal elements relax with time constants called T_2. Usually, only relaxation times of off-diagonal elements corresponding to magnetic-dipole-allowed transitions contribute (e.g., T_2 of the ^{13}C is the relaxation time of elements 12 and 34, while the proton T_2 is that of elements 13 and 24). However, in this experiment, during the long 2π pulse, the spin system spends part of its time in states that are linear combinations of states 1 and 4 and states 2 and 3. These correspond to magnetic-dipole-forbidden transitions. The amplitudes of the two inverted lines in Figure 3 are therefore partially determined by the relaxation rates of the normally not observable elements 14 and 23. Since the two peaks of the doublet have different amplitudes, these two T_2's are not equal. (The 14 and 23 relaxation rates are of special interest since they can depend on the cross-correlation between the fluctuating local fields at the two nuclei.) Thus, we are now able to map out all the relaxation times of the complete density matrix of a system like

this. We will discuss this somewhat specialized spectroscopic idea in great detail in a later paper.

As mentioned earlier, this technique could be generalized to show explicitly the behavior of spins greater than ½ under rotation. As an example, we could consider a system where a spin 1 (e.g., ^{2}H, ^{6}Li, ^{14}N) is scalar coupled to a spin ½ (e.g., ^{1}H, ^{13}C, free electron). Provided the three energy levels of the spin 1 were equally spaced, we could accomplish a rotation of the nucleus as a whole by irradiating at the single resonance frequency. The presence of the spin ½ would split this resonance line into a doublet, and the spin ½ spectrum would be a triplet. By first applying a $\pi/2$ pulse to all of the three spin ½ transitions and then selectively applying a 2π pulse to only one of the lines in the spin 1 doublet, one would see the spin ½ triplet <u>not</u> invert but rather remain upright. A selective π pulse should cause an inversion, however. This is because a spin 1 does not exhibit spinor character. Thus, by choosing systems carefully, one should be able to examine spins with many different numbers of levels, and thus observe the spinor or non-spinor behavior of these systems. It is, in fact, just a property of Hilbert space that systems having an even number of levels behave as spinors and systems with odd numbers of levels behave as non-spinors. Would, for instance, in the above example the three levels of the spin 1 not be equally spaced due to quadrupolar interaction, then only transitions between one pair of levels might be irradiated by one pulse, and this two-level system would behave as a spinor. So it is because fermions have an even number of levels and bosons have an odd number that they behave as they do. A demonstration of the spinor behavior for a ^{13}C as we have shown, is in fact valid as a demonstration for all two-level systems, of which spin ½ particles are particular examples.

Although used here for the demonstration of the spinor character of a spin ½ nucleus, the basic interferometric spectroscopic technique demonstrated here should have much wider applicability. In general, it is applicable whenever we have a system with two or more inequivalent transitions having one quantum mechanical level in common. An obvious application could involve indirect detection of low magnetogyric ratio spins, where this technique can have a signal-to-noise advantage over schemes which depend on diagonal elements of the density matrix, since the ^{1}H spectrum is totally inverted independent of the ratio of the two magnetogyric ratios (related phase effects have been observed in a different context by Ferretti and Ernst[5]). The scheme can, in addition, be applied to a variety of spin systems; for example, inequivalent transitions with a common level could be formed by interaction of two nuclear spins, by electron-nuclear spin interactions, or by magnetic dipole and electric quadrupole interactions of a particle with spin greater than ½.[6] With only slight additional complication, one can envision experiments developed using concepts of recently published schemes for extracting geometrical and orientational information in polycrystalline solids[7,8], which would allow one to obtain comparable information on such quantities as the electric field gradient at a nuclear site.

References

1. S. A. Werner, R. Colella and A. W. Overhauser, and C. F. Eagen, Phys. Rev. Lett. 35, 1053 (1975).
2. H. J. Bernstein, Phys. Rev. Lett. 18, 1102 (1967).
3. Y. Aharonov and L. Susskind, Phys. Rev. 158, 1237 (1967).
4. C. L. Mayne, D. W. Alderman, and D. M. Grant, J. Chem. Phys. 63, 2514 (1975).
5. J. A. Ferretti and R. R. Ernst, J. Chem. Phys. 65, 4283 (1976).
6. Recent reports of a multiple step excitation in ^{27}Al involve establishment of phase coherence of forbidden transitions; see H. Hataraka, T. Terao, and T. Hashi, J. Phys. Soc. Japan 39, 835 (1975); H. Hataraka and T. Hashi, ibid 39, 1139 (1975).
7. M. E. Stoll, A. J. Vega, and R. W. Vaughan, J. Chem. Phys. 65, 4093 (1976).
8. M. E. Stoll, A. J. Vega, and R. W. Vaughan, Proceedings of the XIXth Congress Ampere, Heidelberg, 1976.

Figure Captions

Figure 1. Energy level diagram for two weakly coupled inequivalent spin ½ particles (^{13}C, ^{1}H) in a strong magnetic field. The α and β represent the two eigenstates spin up and spin down of the spin ½ particle. The first Greek letter represents the state of the ^{1}H spin and the second represents the state of the ^{13}C spin, so the two ^{1}H transitions are shown with single arrows while the two ^{13}C transitions are shown with double arrows. The numbers 1, 2, 3, 4 are used to refer to the various energy levels or to the eigenstates to which they correspond. The relative Zeeman energies for ^{1}H (56.4 MHz) and ^{13}C (14.2 MHz) have been drawn to scale, but the effects of the weak coupling have been greatly exaggerated for emphasis.

Figure 2. Radiofrequency pulse sequence used. A $\pi/2$ pulse and a π pulse were applied to the ^{1}H transitions and the resulting spin echo was recorded from time t = 0 for Fourier transformation. The spectrum was obtained first with no ^{13}C irradiation (τ = 0) and second with a selective 2π pulse (τ = 26 msec) applied to only one ^{13}C transition.

Figure 3. ^{1}H Fourier transform NMR spectra explicitly showing spinor character of a spin ½ particle. The top spectrum involved no ^{13}C irradiation while the bottom spectrum utilized a selective 2π pulse applied to only one ^{13}C transition. The splitting of 195 Hz is between the two peaks of the doublet due to weak scalar coupling of the ^{1}H and ^{13}C in the formate ions containing ^{13}C. The small peak at the center of the doublet is due to ^{1}H in formate ions containing ^{12}C, while the large peak at the far right is due to the small amount of ^{1}H in the solvent.

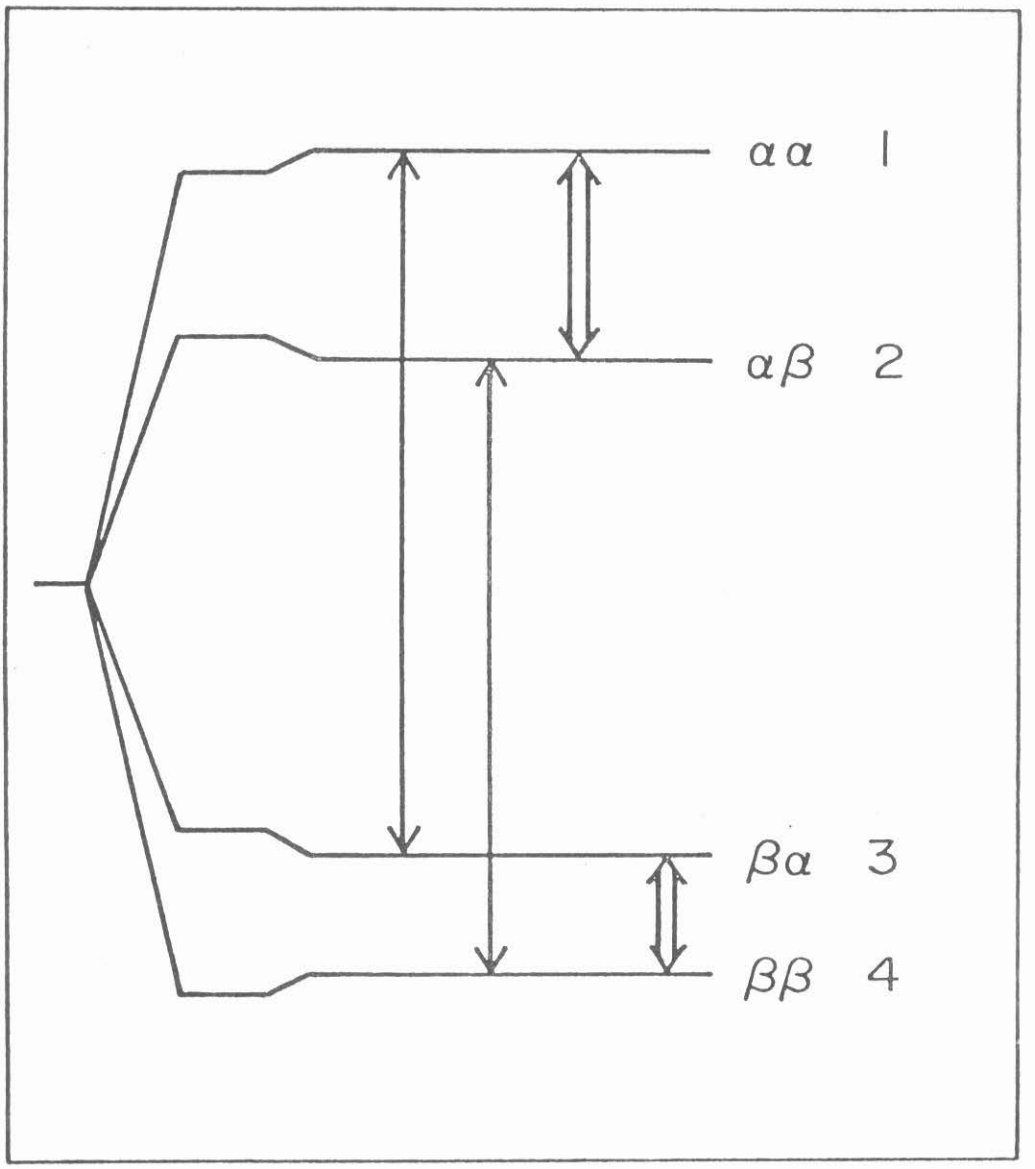

Fig. 1

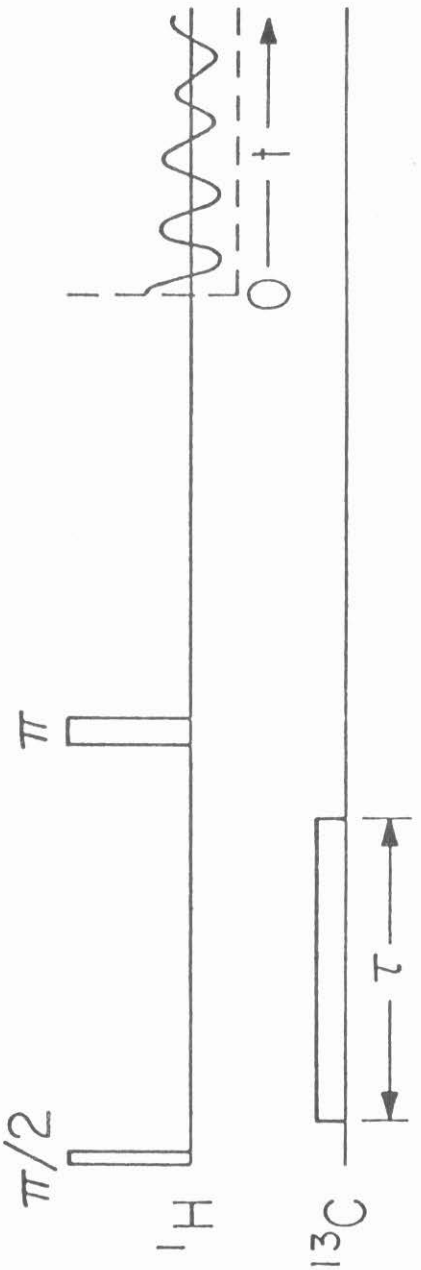

Fig. 2

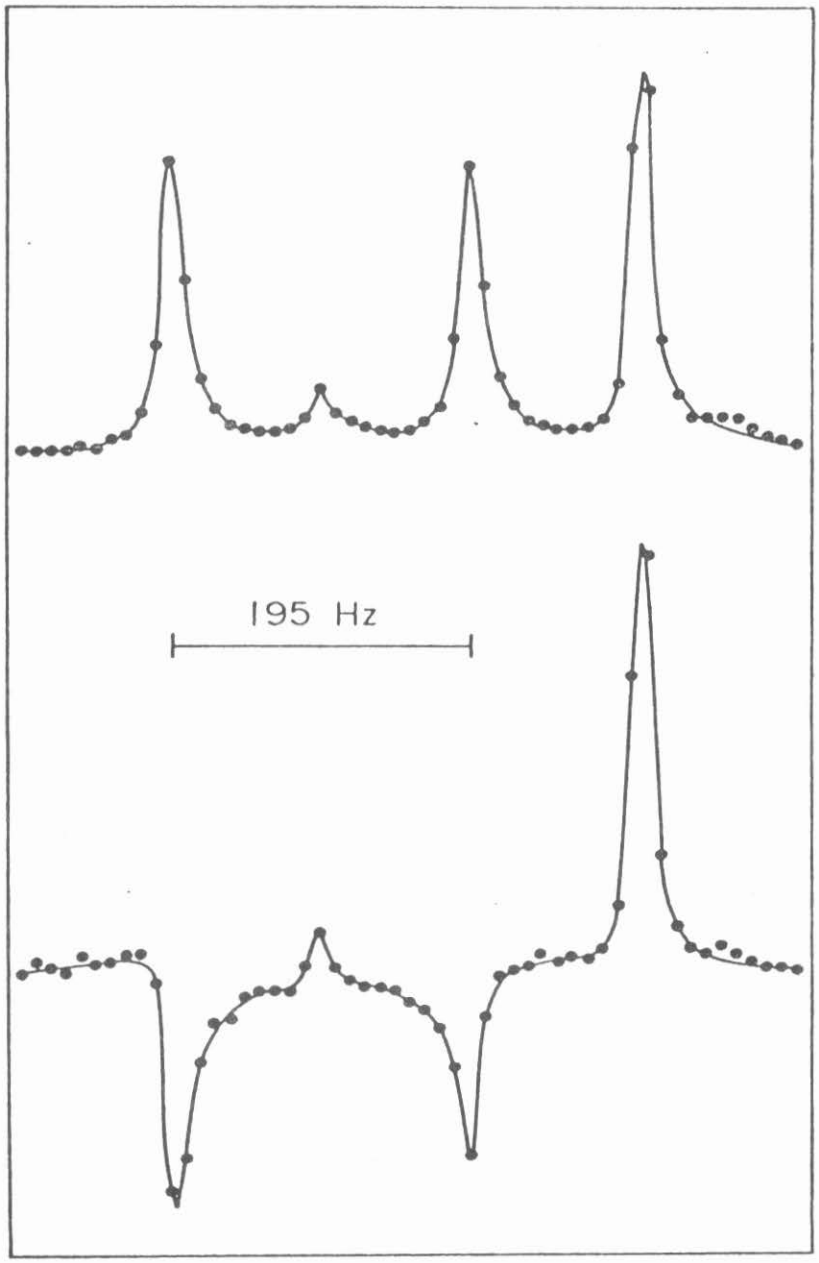

Fig. 3

CHAPTER 4

NUCLEAR MAGNETIC DOUBLE RESONANCE PHASE INTERFEROMETRY: RELAXATION TIMES FOR DIPOLAR FORBIDDEN TRANSITIONS AND OFF-RESONANCE EFFECTS IN AN AX SPIN SYSTEM

(Chapter 4 is essentially an article by M. E. Stoll, A. J. Vega, and R. W. Vaughan, entitled "Double Resonance Interferometry: Relaxation Times for Dipolar Forbidden Transitions and Off-Resonance Effects in an AX Spin System". This article has been submitted for publication to the Journal of Chemical Physics.)

I. INTRODUCTION

This paper presents a detailed analysis of the application of a recently presented interferometric spectroscopic technique[1] to a model AX spin system. The density matrix for such a coupled spin ½ system is a four-by-four matrix, and when such a spin system in a strong magnetic field is prepared in a nonequilibrium state, the subsequent relaxation of the system to thermal equilibrium can be described by the decay of the elements of the density matrix, where the diagonal elements relax with characteristic time constants, called T_1's, and the off-diagonal elements relax with characteristic time constants called T_2's[2,3]. The determination of all of the T_1's requires a sequence of experiments, and this has been discussed recently in detail for an AX system by Mayne, Alderman, and Grant[4], while measurement of the off-diagonal relaxation rates corresponding to magnetic-dipole-allowed transitions involves application of a standard Carr-Purcell sequence. This leaves off-diagonal rates corresponding to magnetic-dipole-forbidden transitions to be measured, and the present paper presents a simple method for direct measurement of these remaining relaxation rates. These rates are of particular interest since they can contain cross-correlation information about the fluctuating fields at the sites of the coupled A and X nuclei. In our review of the literature we have found no reports of previous efforts to measure these relaxation rates in coupled spin ½ systems, although we do want to call attention to an effort to detect such dipolar-forbidden transitions by a multiple step excitation process, and that effort involved a spin 5/2 nucleus, ^{27}Al in Al_2O_3[5].

In addition, the analysis of off-resonance phase effects measured in the spectra demonstrate that one can use such an interferometric scheme to measure indirectly the resonance frequency of one of the coupled nuclei by observation of

the spectra of only the second nucleus. The limiting precision of such an indirect measurement will be shown to be equivalent to that of a direct measurement. This could be of use when the magnetogyric ratios of the two coupled spins differ by a large amount, and the direct observation of the nucleus with the smaller magnetogyric ratio is made difficult by poor signal-to-noise conditions.

II. DESCRIPTION AND EXPLANATION OF THE EXPERIMENT

A. General Description

The system we chose for this experiment was a conventional AX(^{13}C - ^{1}H) system where both nuclei are spin ½. The ^{13}C (S spin) and ^{1}H (I spin) were in a liquid and were weakly coupled to each other via a scalar coupling of the form $J \underset{\sim}{I} \cdot \underset{\sim}{S}$. Since the sample was in a strong magnetic field, oriented along the z-axis, only the secular part of the scalar interaction, $J I_z S_z$, contributed to first order to the energy level spacings for this system. An appropriate energy-level diagram is shown in Figure 1. The four levels are the eigenstates of the Zeeman Hamiltonian corresponding to $\alpha\alpha$, $\alpha\beta$, $\beta\alpha$, and $\beta\beta$, where the α and β represent the spin "up" and "down" states with the z-component of angular momentum equal to $\frac{1}{2}\hbar$ and $-\frac{1}{2}\hbar$, and the first Greek letter refers to the I spin while the second refers to the S spin. Note that the secular part of the scalar interaction alters the energy levels slightly (exaggerated considerably in Figure 1 for purposes of explanation), thus giving rise to four inequivalent magnetic-dipole-allowed transitions. The ^{1}H NMR spectrum is a doublet corresonding to transitions 1-3 and 2-4 (single arrows), and the ^{13}C spectrum is also a doublet corresponding to transitions 1-2and 3-4 (double arrows). This doublet splitting is crucial for the present experiment since it enables us to selectively irradiate certain transitions.

The experiment is shown schematically in Figure 2. First, we apply a nonselective $\pi/2$ pulse (2 μsec) to both the proton transitions. Then immediately after the $\pi/2$ pulse we apply a low-power, selective pulse of length τ to only one of the ^{13}C transitions. At a time ΔT after the original proton $\pi/2$ pulse we apply another nonselective π pulse (4 μsec) to both proton transitions, causing a proton spin echo to be formed at time $2\Delta T$. The decay taken from time t = 0

(at the middle of the echo) is recorded for Fourier transformation (FT). The five spectra shown in Figure 3 are such FT spectra for values of τ = 0, 28, 56, 84, and 112 msec. The top spectrum, for which τ = 0, corresponds to a conventional spin echo pulsed NMR-FT proton spectrum. The sample was a solution of 91% ^{13}C-enriched sodium formate ($NaCHO_2$) dissolved in D_2O with a small amount of ^1H impurity. It is the ^1H and the ^{13}C in the enriched formate ions that comprise our AX spin system and give rise to the symmetric proton doublet split by J = 195 Hz. The small peak at the center of the doublet is due to the protons in the 9% of the formate ions containing spinless ^{12}C. The large peak on the far left is due to the small amount of proton impurity in the D_2O. When preparing the solution, no efforts were made to remove dissolved oxygen.

When looking at the spectra of Figure 3, two effects stand out. First, we see that the amplitude of the formate doublet actually goes to zero, then negative, back to zero, and finally positive again. Secondly, the amplitudes of both members of the doublet do not remain the same. The former effect can be explained completely by the spin dynamics of the system[1] while the latter effect can be explained only by invoking relaxation phenomena. Therefore, in order to understand the results of this experiment, we must theoretically understand the spin dynamics of such a system first without, and later with, relaxation effects taken into account.

B. Spin Dynamics Ignoring Off-Resonance and Relaxation Effects

We first examine the spin dynamics of our experiment, ignoring relaxation effects as well as effects of the ^{13}C selective pulse being "off-resonance." There are, in fact, two such off-resonance effects to be ignored. The first is the possibility of the selective r.f. radiation being at a slightly different frequency from the ^{13}C transition frequency. The second is the possibility

that although the selective radiation is weak, it still is strong enough to somewhat disturb the other ^{13}C transition.

Before we apply the first pulse, we assume that our spin system is in thermal equilibrium and that it can be described by the following 4 x 4 density matrix:

$$\rho_{equil} = \begin{bmatrix} A & 0 & 0 & 0 \\ 0 & B & 0 & 0 \\ 0 & 0 & C & 0 \\ 0 & 0 & 0 & D \end{bmatrix} \qquad (1)$$

where the basis states are chosen to be the states 1, 2, 3, and 4 of Figure 1 ($\alpha\alpha$, $\alpha\beta$, $\beta\alpha$, and $\beta\beta$, respectively). Note that the off-diagonal matrix elements are zero, meaning there is no statistical phase coherence in the system and, furthermore, in the high temperature approximation

$$A - B = C - D \qquad (2)$$

As usual, the observable ^{1}H and ^{13}C magnetizations are proportional to the expectation values of the dimensionless spin operators, I and S. The expectation values for I and S corresponding to the various observable magnetizations are related to the density matrix elements as follows:

$$\begin{aligned} \langle I_x \rangle_{13} &= \text{Re } \rho_{13} \quad , \quad \langle I_x \rangle_{24} = \text{Re } \rho_{24} \\ \langle I_y \rangle_{13} &= -\text{Im } \rho_{13} \quad , \quad \langle I_y \rangle_{24} = -\text{Im } \rho_{24} \\ \langle I_z \rangle_{13} &= \tfrac{1}{2}(\rho_{11} - \rho_{33}) \quad , \quad \langle I_z \rangle_{24} = \tfrac{1}{2}(\rho_{22} - \rho_{44}) \\ \langle S_x \rangle_{12} &= \text{Re } \rho_{12} \quad , \quad \langle S_x \rangle_{34} = \text{Re } \rho_{34} \end{aligned} \qquad (3)$$

$$\langle S_y \rangle_{12} = -\mathrm{Im}\,\rho_{12} \quad , \quad \langle S_y \rangle_{34} = -\mathrm{Im}\,\rho_{34}$$

$$\langle S_z \rangle_{12} = \tfrac{1}{2}(\rho_{11} - \rho_{22}) \quad , \quad \langle S_z \rangle_{34} = \tfrac{1}{2}(\rho_{33} - \rho_{44})$$

Because of the hermiticity of the density matrix, $\mathrm{Re}\rho_{ij} = \mathrm{Re}\rho_{ji}$ and $\mathrm{Im}\rho_{ij} = -\mathrm{Im}\rho_{ji}$. The subscripts refer to particular levels between which transitions give rise to observable magnetization. Because of the scalar splitting, we can distinguish between the transverse magnetization $\langle I_x \rangle_{13}$ and $\langle I_x \rangle_{24}$, etc. Each corresponds to one of the peaks of the doublet. However, since we do not know the sign of J, we do not know which magnetization corresponds to which peak. Fortunately, this is no serious drawback, and we will say more about this point later in the paper.

Initially, since the off-diagonal elements are zero, there is no transverse magnetization. The purpose of the proton $\pi/2$ is then to create some transverse magnetization and phase coherence. After the $\pi/2$ pulse, (assumed to be along the x-axis of the proton rotating frame), we have the following matrix, making use of Equation (2) and ignoring effects due to the finite width of the pulse:

$$\rho(0) = \begin{bmatrix} \frac{1}{2}(A+C) & 0 & \frac{1}{2}i(A-C) & 0 \\ 0 & \frac{1}{2}(B+D) & 0 & \frac{1}{2}i(A-C) \\ -\frac{1}{2}i(A-C) & 0 & \frac{1}{2}(A+C) & 0 \\ 0 & -\frac{1}{2}i(A-C) & 0 & \frac{1}{2}(B+D) \end{bmatrix} \qquad (4)$$

The Hamiltonian acting on the system during the weak ^{13}C pulse is (for $\hbar = 1$):

$$H = \omega_I I_z + \omega_S S_z + J I_z S_z + 2\omega_1 S_x \cos \omega t \qquad (5)$$

where we have chosen the pulse to be along the x-axis of the ^{13}C rotating frame. The frequencies ω_I and ω_S are the Larmor frequencies of the ^1H and ^{13}C, ω is the frequency of the ^{13}C pulse, $2\omega_1$ is its amplitude, and J is the scalar coupling in radians per second. We now analyze this by transforming to a doubly rotating frame in which the Hamiltonian is static, by choosing to go to the interaction frame of:

$$H_o = \omega S_z + \omega_p I_z \qquad (6)$$

where ω_p is the reference frequency of the phase detector we used to detect the proton traverse magnetization. After transforming to this frame we have the following Hamiltonian

$$H' = \Delta\omega I_z + \tfrac{1}{2} J S_z + J I_z S_z + \omega_1 S_x$$

$$\Delta\omega = \omega_I - \omega_p \qquad (7)$$

$$\omega_S - \omega = \tfrac{1}{2} J$$

ignoring the counter-rotating r.f. component as usual. The density matrix ρ is also taken to be in this same rotating frame, and for the sake of simplicity we will not use any special notation to indicate this. Equation (4) is still correct because we have assumed the lab frame and the interaction frame to be coincident before the $\pi/2$ pulse, and we are justifiably assuming the pulse is short enough to ignore effects during the pulse. The density matrix evolves in time according to the Liouville equation:

$$\frac{d}{dt}\rho = i\,[\rho, H'] \tag{8}$$

Using Equations (7) we have the following matrix for H':

$$H' = \begin{bmatrix} \frac{1}{2}(J+\Delta\omega) & \frac{1}{2}\omega_1 & 0 & 0 \\ \frac{1}{2}\omega_1 & -\frac{1}{2}(J-\Delta\omega) & 0 & 0 \\ 0 & 0 & -\frac{1}{2}\Delta\omega & \frac{1}{2}\omega_1 \\ 0 & 0 & \frac{1}{2}\omega_1 & -\frac{1}{2}\Delta\omega \end{bmatrix} \tag{9}$$

The first kind of previously mentioned off-resonance effect was ignored when we chose $\omega - \omega_S = \frac{1}{2} J$, from Equations (7), because the ^{13}C radiation is being applied right "on" one of the resonances of the doublet. The second kind of off-resonance effect is ignored by assuming that

$$J >> \tfrac{1}{2}\omega_1 \text{ or } |H'_{11} - H'_{22}| >> H'_{12} \tag{10}$$

This approximation means that the r.f. perturbation is so weak that it does not mix levels 1 and 2, thus we set $H'_{12} = H'_{21} = 0$. However, levels 3 and 4 are still very strongly mixed by the ^{13}C pulse.

Because this experiment involves observing only the I transverse magnetization, Equations (3) show that it is sufficient to calculate only ρ_{13} and ρ_{24} (or ρ_{31} and ρ_{42}), and thus we shall only worry about determining these matrix elements. Using Equations (8) and (9) we can write the following differential equations, and their initial conditions using Equation (4):

$$\dot{\rho}_{13} = -i\ (\tfrac{1}{2}J + \Delta\omega)\ \rho_{13} + i\ \tfrac{1}{2}\omega_1\ \rho_{14}$$

$$\dot{\rho}_{14} = -i\ (\tfrac{1}{2}J + \Delta\omega)\ \rho_{14} + i\ \tfrac{1}{2}\ \omega_1\ \rho_{13}$$

$$\dot{\rho}_{24} = \ i\ (\tfrac{1}{2}J - \Delta\omega)\ \rho_{24} + i\ \tfrac{1}{2}\ \omega_1\ \rho_{23} \qquad (11)$$

$$\dot{\rho}_{23} = \ i\ (\tfrac{1}{2}J - \Delta\omega)\ \rho_{23} + i\ \tfrac{1}{2}\ \omega_1\ \rho_{24}$$

$$\rho_{13}\ (0) = \rho_{24}\ (0) = \tfrac{1}{2}\ i\ (A - C)$$

$$\rho_{14}\ (0) = \rho_{23}\ (0) = 0$$

Solving these equations, we can determine the relevant matrix elements at the end of the ^{13}C pulse of length τ

$$\rho_{13}\ (\tau) = \tfrac{1}{2}\ i\ (A - C)\ e^{-i(\frac{1}{2}J + \Delta\omega)\tau} \cos(\tfrac{1}{2}\ \omega_1\tau)$$

$$\rho_{24}\ (\tau) = \tfrac{1}{2}\ i\ (A - C)\ e^{i(\frac{1}{2}J - \Delta\omega)\tau} \cos(\tfrac{1}{2}\ \omega_1\tau) \qquad (12)$$

The time evolution of the density matrix from the time τ through the π proton pulse at ΔT, which we take to be along the x-axis of the proton rotating frame, and finally up to the middle of the echo at $2\Delta T$, is quite straightforward to calculate, and we merely state the pertinent results:

$$\rho_{31}\ (2\Delta T) = e^{i(\frac{1}{2}J + \Delta\omega)\tau}\ \rho_{13}\ (\tau)$$

$$\rho_{42}\ (2\Delta T) = e^{-i(\frac{1}{2}J - \Delta\omega)\tau}\ \rho_{24}\ (\tau) \qquad (13)$$

Thus, from Equations (12) and (13), we have

$$\rho_{31}\ (2\Delta T) = \tfrac{1}{2}\ i\ (A - C)\ \cos\ (\tfrac{1}{2}\omega_1\tau)$$
$$\rho_{42}\ (2\Delta T) = \tfrac{1}{2}\ i\ (A - C)\ \cos\ (\tfrac{1}{2}\omega_1\tau) \qquad (14)$$

We can then use Equations (3) to compute the transverse proton magnetization of the two peaks in the ^1H doublet

$$\langle I_y\ (2\Delta T)\rangle_{13} = \langle I_y\ (2\Delta T)\rangle_{24} = \langle I_y\ (2\Delta T)\rangle_{\tau=0}\ \cos\ (\tfrac{1}{2}\omega_1\tau)$$
$$\langle I_x\ (2\Delta T)\rangle_{13} = \langle I_x\ (2\Delta T)\rangle_{24} = 0 \qquad (15)$$

where $\langle I_y(2\Delta T)\rangle_{\tau=0}$ is just the magnitude of the transverse magnetization at $2\Delta T$ (the middle of the echo) for the case in which $\tau = 0$ (no ^{13}C irradiation). Thus, we see that the effect of our selective ^{13}C pulse is to cause the proton magnetization to oscillate sinusoidally with a frequency of $\frac{1}{2}\omega_1$. So by choosing the length of τ to correspond to a normal 2π pulse ($\omega_1\tau = 2\pi$) we see that effect is to multiply the amplitude of the proton doublet by $\cos(\pi) = -1$. This effect is the manifestation of the spinor character of the pseudo-two-level system composed of levels 3 and 4, and this phenomenon has been discussed in detail elsewhere[1]. The spectra in Figure 3 were taken for values of τ corresponding to values of $\omega_1\tau = 0, \pi, 2\pi, 3\pi$, and 4π. Note that after a full 4π rotation the phase of the proton magnetization has come back to itself again, which is further consistent with spinor behavior. Thus, we can see that this idealized spin dynamical approach can at least explain the oscillatory behavior in Figure 3. However, we need to understand quantitatively the amplitudes of both members of the doublet, and this can only be done by appealing to relaxation effects.

By examining Equations (15), one notes that the magnetization linearly oscillates rather than precesses. By looking at Equations (11) we see that the matrix elements ρ_{13} and ρ_{14} are coupled, as well as ρ_{24} and ρ_{23}. Solving for ρ_{14} would show that $\rho_{14} \propto \sin(\frac{1}{2}\omega_1\tau)$; therefore, we see that ρ_{13} and ρ_{14} are mutually oscillating and when one has a maximum, the other is zero, and vice versa. According to the definition of the density matrix:

$$\rho_{ij} = \overline{C_i\, C_j^*} \tag{16}$$

where C_i and C_j are the complex quantum mechanical amplitudes for the system to be in the states i and j, and the bar represents the mixed state which results from taking a statistical ensemble average over the system. Thus, we see that when $\rho_{14} \neq 0$, statistically our system is in a linear combination of states 1 and 4. This, in turn, means that there is phase coherence or "magnetization" corresponding to the forbidden transition 1-4. The reason we do not see this magnetization is twofold. First of all, since it is magnetic-dipole-forbidden, the process is second order and the probability of the transition is correspondingly low. Secondly, the 1-4 transition frequency is at about $\omega_I + \omega_S$, and we would have to make our phase detection reference frequency ω_p closer to this "double quantum" frequency in order to observe this magnetization. Similarly, ρ_{24} and ρ_{23} form a complementary pair of oscillating variables, and $\rho_{23} \neq 0$ implies phase coherence between the levels 2 and 3, which corresponds to a magnetic-dipole-forbidden "flip-flop" transition. In anticipation of our later discussion of relaxation effects, we mention that if the off-diagonal element ρ_{14} relaxes with a different rate than ρ_{13}, we would expect the amplitude of the 1-3 peak of the doublet to be different from the prediction of Equations (15). This is because for $\tau \neq 0$, the system has a probability of being in a linear combination of states 1 and 4 as well

as 1 and 3. Thus, the ratio of $<I_y(2\Delta T)>$ to $<I_y(2\Delta T)>_{\tau=0}$ could be either smaller or larger than that predicted by Equations (15), depending on whether or not the relaxation rate of ρ_{14} is faster or slower than the relaxation rate of ρ_{13}. Again, similar statements can be made about the rates of ρ_{24} and ρ_{23}. Thus, by attempting to quantitatively fit the amplitudes of the peaks of the formate doublet for different values of τ, we can in fact determine the relaxation rates of the density matrix elements ρ_{14} and ρ_{23}. In the next section we pursue the effects of being "off-resonance" on the ^{13}C frequency, while still ignoring relaxation. We will see that these "off-resonance" effects cannot explain the fact that the doublet does not remain symmetric.

C. Spin Dynamics Including Off-Resonance Effects but Ignoring Relaxation Effects

As mentioned earlier, there are two important "off-resonance" effects of the selective ^{13}C pulse to be considered. These both fall naturally out of the mathematics, if we choose the proper interaction frame. We start with the same Hamiltonians as those in Equations (5) and (6); however, we will choose our frequency of ^{13}C irradiation, ω, slightly differently. In this case Equations (7) must be modified so that now after transformation to the interaction frame, we have the following remaining Hamiltonian:

$$H' = \Delta\omega\ I_z + (\tfrac{1}{2}J + \delta\omega)\ S_z + J\ I_z\ S_z + \omega_1\ S_x$$

$$\Delta\omega = \omega_I - \omega_p \qquad (17)$$

$$\omega_S - \omega = \tfrac{1}{2}J + \delta\omega$$

Therefore $\delta\omega$ is just the difference in frequency between the applied ^{13}C radiation frequency and the frequency of the one member of the doublet we are

intending to irradiate, and thus $\delta\omega$ measures an "off-resonance" effect. Using Equations (17) we can now write the matrix representing H'

$$H' = \begin{bmatrix} \frac{1}{2}(J+\delta\omega+\Delta\omega) & \frac{1}{2}\omega_1 & 0 & 0 \\ \frac{1}{2}\omega_1 & -\frac{1}{2}(J+\delta\omega-\Delta\omega) & 0 & 0 \\ 0 & 0 & \frac{1}{2}(\delta\omega-\Delta\omega) & \frac{1}{2}\omega_1 \\ 0 & 0 & \frac{1}{2}\omega_1 & -\frac{1}{2}(\delta\omega+\Delta\omega) \end{bmatrix} \qquad (18)$$

We can examine the other type of ^{13}C "off-resonance" effect by <u>not</u> making the assumption of Equation (10). Therefore, we are saying our ^{13}C radiation is substantial enough to somewhat disturb the other member of the ^{13}C doublet. Thus, it is no longer necessary to assume that $J >> \frac{1}{2}\omega_1$, and we are <u>not</u> so far "off-resonance" from the other ^{13}C transition that it is irrelevant. So proceeding with this in mind, we can use Equation (18) and the Liouville Equation (8) to get the following set of coupled differential equations:

$$\begin{aligned} \dot{\rho}_{13} &= -i\,(\tfrac{1}{2}J + \Delta\omega)\,\rho_{13} + i\,\tfrac{1}{2}\omega_1\,(\rho_{14} - \rho_{23}) \\ \dot{\rho}_{14} &= -i\,(\tfrac{1}{2}J + \Delta\omega + \delta\omega)\,\rho_{14} + i\,\tfrac{1}{2}\omega_1\,(\rho_{13} - \rho_{24}) \\ \dot{\rho}_{24} &= i\,(\tfrac{1}{2}J - \Delta\omega)\,\rho_{24} + i\,\tfrac{1}{2}\omega_1\,(\rho_{23} - \rho_{14}) \\ \dot{\rho}_{23} &= i\,(\tfrac{1}{2}J - \Delta\omega + \delta\omega)\,\rho_{23} + i\,\tfrac{1}{2}\omega_1\,(\rho_{24} - \rho_{13}) \end{aligned} \qquad (19)$$

The initial conditions for ρ_{13}, ρ_{14}, ρ_{24}, and ρ_{23} are identical to those in Equations (11). The solution of this set of equations is rather tedious, but the important matrix elements can be shown to be:

$$\rho_{13}(\tau) = \tfrac{1}{2}(A-C)\, e^{-i\Delta\omega\tau}\{i(a\cos\Omega_+\tau + c\cos\Omega_-\tau) + (b\sin\Omega_+\tau + d\sin\Omega_-\tau)\}$$

$$\rho_{24}(\tau) = \tfrac{1}{2}(A-C)\, e^{-i\Delta\omega\tau}\{i(a\cos\Omega_+\tau + c\cos\Omega_-\tau) - (b\sin\Omega_+\tau + d\sin\Omega_-\tau)\} \tag{20}$$

where we have

$$\Omega_\pm = \frac{1}{\sqrt{2}}\{(\tfrac{J}{2})^2 + (\tfrac{J}{2}+\delta\omega)^2 + \omega_1^2 \pm [(\tfrac{J}{2})^4 + (\tfrac{J}{2}+\delta\omega)^4 + \omega_1^4 - 2(\tfrac{J}{2})^2(\tfrac{J}{2}+\delta\omega)^2 + 2(\tfrac{J}{2})^2\omega_1^2 + 2\omega_1^2(\tfrac{J}{2}+\delta\omega)^2]^{\frac{1}{2}}\}^{\frac{1}{2}} \tag{21}$$

where Ω_+ refers to the top sign and Ω_- refers to the bottom sign. Also, we have the following values for a, b, c, and d in Equations (20):

$$a = \frac{\Omega_-^2 - (\frac{J}{2})^2}{\Omega_-^2 - \Omega_+^2}$$

$$c = \frac{(\frac{J}{2})^2 - \Omega_+^2}{\Omega_-^2 - \Omega_+^2} \tag{22}$$

$$b = \frac{(\frac{J}{2})[\Omega_-^2 - (\frac{J}{2})^2 - \omega_1^2]}{\Omega_+(\Omega_-^2 - \Omega_+^2)}$$

$$d = \frac{(\frac{J}{2})[(\frac{J}{2})^2 + \omega_1^2 - \Omega_+^2]}{\Omega_-(\Omega_-^2 - \Omega_+^2)}$$

The following relations also hold true

$$a + c = 1$$

$$\Omega_+ b + \Omega_- d = \frac{J}{2} \tag{23}$$

After the ^{13}C pulse ends, the density matrix evolution is identical to that in Equations (13). Then using Equations (13), (20), and (3) we compute the proton transverse magnetization at $2\Delta T$ to be

$$\langle I_y(2\Delta T)\rangle_{13} = \langle I_y(2\Delta T)\rangle_{24} = \langle I_y(2\Delta T)\rangle_{\tau=0} \{(b \sin \Omega_+\tau + d \sin \Omega_-\tau)\sin(\tfrac{J}{2}\tau) + (a \cos \Omega_+\tau + c \cos \Omega_-\tau) \cos (\tfrac{J}{2} \tau) \}$$

$$\langle I_x(2\Delta T)\rangle_{13} = -\langle I_x(2\Delta T)\rangle_{24} = \langle I_y(2\Delta T)\rangle_{\tau=0} \{(b \sin \Omega_+\tau + d \sin \Omega_-\tau)\cos(\tfrac{J}{2}\tau) - (a \cos \Omega_+\tau + c \cos \Omega_-\tau) \sin (\tfrac{J}{2} \tau) \} \quad (24)$$

where $\langle I_y(2\Delta T)\rangle_{\tau=0}$ is again the amplitude of either of the peaks of the doublet for the case where $\tau = 0$. Notice that the y-components of the magnetization of the proton doublet are identical, while the x-components merely differ by a sign.

Careful examination of Equations (24) tells us several important things. First of all, we see that neither of the ^{13}C "off-resonance" effects we have considered can possibly lead to the discrepancy in the amplitudes of the peaks in the doublet of the spectra in Figure 3. Any such off-resonance effects may alter the overall amplitudes of the peaks as well as introduce dispersion to the peaks, via the x-components, but the two peaks must remain mirror images of each other in the spectrum. Because of this, we can then rule out magnetic field inhomogeneity as a possible cause of that discrepancy. Magnetic field inhomogeneity can be treated by summing a distribution of peaks being off-resonance by different amounts. However, any distribution of frequency would still lead to overall lineshapes for the two peaks which are mirror images of each other, thus ruling this effect out as a possible

explanation. Also we can precisely determine $\delta\omega$, and consequently, the resonance frequency of the ^{13}C line by observing the effects of dispersion on the lineshape.

The full behavior of the functions in Equations (24) is quite involved. However, we can look at certain limiting cases to separate the two kinds of off-resonance effects. To try to understand the first type of off-resonance effect where the ^{13}C radiation is slight "off" the intended frequency, we can take the limit of Equations(24) in the case where we assume the approximation in Equations (10) to be valid. In this case Equations (24) become:

$$\langle I_y(2\Delta T)\rangle_{13} = \langle I_y(2\Delta T)\rangle_{24} = \langle I_y(2\Delta T)\rangle_{\tau=0} \{\cos\left(\tfrac{1}{2}\sqrt{\omega_1^2 + \delta\omega^2}\,\tau\right)\cos\left(\frac{\delta\omega\tau}{2}\right) + \frac{\delta\omega}{\sqrt{\omega_1^2 + \delta\omega^2}}\sin\left(\tfrac{1}{2}\sqrt{\omega_1^2 + \delta\omega^2}\,\tau\right)\sin\left(\frac{\delta\omega\tau}{2}\right)\}$$

(25)

$$\langle I_x(2\Delta T)\rangle_{13} = -\langle I_x(2\Delta T)\rangle_{24} = \langle I_y(2\Delta T)\rangle_{\tau=0} \{\cos\left(\tfrac{1}{2}\sqrt{\omega_1^2 + \delta\omega^2}\,\tau\right)\sin\left(\frac{\delta\omega\tau}{2}\right) - \frac{\delta\omega}{\sqrt{\omega_1^2 + \delta\omega^2}}\sin\left(\tfrac{1}{2}\sqrt{\omega_1^2 + \delta\omega^2}\,\tau\right)\cos\left(\frac{\delta\omega\tau}{2}\right)\}$$

For the case where $\delta\omega << \omega_1$, we see that Equations (25) are the same as those of Equations (15) except that there is a phase error of $\delta\omega\tau/2$ introduced into the peaks. Thus, both peaks have the same amount of dispersion mixed in, and the sign of that dispersion is opposite for the two peaks. We note that we can use this effect to our advantage in determining the position of the ^{13}C resonances. We could arbitrarily increase τ until any ^{13}C off-resonance, $\delta\omega$, no matter how small, would lead to noticeable phase changes in the proton spectrum;

however, an upper limit on τ, equal to approximately the inverse of the ^{13}C linewidth, effectively limits the resolution of $\delta\omega$ to the ^{13}C linewidth. Thus, this indirect method of determining the position of the ^{13}C resonance seems to be superior, in this case, to other methods such as spin tickling[6], whose resolution is ultimately limited by the proton rather than the ^{13}C linewidth.

The second type of off-resonance effect, in which we take into account the effect of weakly irradiating the other member of the ^{13}C doublet, can be examined by assuming that

$$\delta\omega = 0 \tag{26}$$

but not making the assumption of Equations(10). Taking the subsequent limiting case of Equations(24) expanded to second order in the parameter $x = \omega_1/J$, we have the following

$$\begin{aligned}
\langle I_y(2\Delta T)\rangle_{13} = \langle I_y(2\Delta T)\rangle_{24} = \langle I_y(2\Delta T)\rangle_{\tau=0} \{ & \cos(\tfrac{1}{2}\omega_1\tau)\,[\cos[(\tfrac{1}{2}\omega_1\tau)(\tfrac{1}{2}x)] \\
& -\tfrac{1}{2}x^2 \sin[(\tfrac{J}{2}\tau)(1+\tfrac{1}{2}x^2)] \sin(\tfrac{J}{2}\tau)\,] \\
& + x \sin(\tfrac{1}{2}\omega_1\tau) \sin[(\tfrac{J}{2}\tau)(1+\tfrac{1}{2}x^2)] \cos(\tfrac{J}{2}\tau)\,\}
\end{aligned} \tag{27}$$

$$\begin{aligned}
\langle I_x(2\Delta T)\rangle_{13} = -\langle I_x(2\Delta T)\rangle_{24} = \langle I_y(2\Delta T)\rangle_{\tau=0} \{ & \cos(\tfrac{1}{2}\omega_1\tau)\,[\sin[(\tfrac{1}{2}\omega_1\tau)(\tfrac{1}{2}x)] \\
& -\tfrac{1}{2}x^2 \sin[(\tfrac{J}{2}\tau)(1+\tfrac{1}{2}x^2)] \cos(\tfrac{J}{2}\tau)\,] \\
& - x \sin(\tfrac{1}{2}\omega_1\tau) \sin[(\tfrac{J}{2}\tau)(1+\tfrac{1}{2}x^2)] \sin(\tfrac{J}{2}\tau)\,\}
\end{aligned}$$

Thus, we see for the case of $x \ll 1$ (or $\omega_1 \ll J$) that Equations (27) are the same as Equation (15) except that there is a phase error of $(\omega_1\tau/2)\cdot(x/2)$ introduced into the peaks. Thus, again both peaks have equal and opposite

amounts of dispersion mixed in. If we intend to use the first type of off-resonance effect to find the ^{13}C resonance position by observing the amount of dispersion mixed in, we must take into account also this other phase error due to the second type of off-resonance effect. This does not hurt our resolution of the ^{13}C resonant frequency, but it does mean that we must subtract off this second effect. Although we do not show the results here, computer calculations of Equations (24) indicate that if both types of off-resonance effects are present simultaneously and they are both small, their phase errors will, in fact, merely add linearly rather than combine in some more complicated manner.

Thus, it seems that the detailed spin dynamics of the experiment, taking off-resonance effects into account, seem to provide the necessary insight to use this technique as a very accurate, indirect method of determining the ^{13}C resonant frequency. However, only in the next section, where we investigate the effects of relaxation, can we quantitatively fit the measured peak amplitude to theoretical calculations.

D. Spin Dynamics Including Relaxation Effects but Ignoring Off-Resonance Effects

In order to make the relaxation calculation more tractable and more easily interpretable, we have chosen to ignore both types of ^{13}C off-resonance effects in this section. According to Redfield's theory of relaxation[2], we can include relaxation effects by assuming that we have a modified Liouville equation:

$$\frac{d}{dt}\rho_{mn} = i[\rho, H']_{mn} - \frac{1}{T_{mn}}\rho_{mn} \qquad (m \neq n) \qquad (28)$$

Since the relaxation times are long compared to 1/J, we can assume that the damping term in Equation (28) for off-digonal matrix elements depends only

on the same matrix element appearing on the left-hand side of Equation (28). Each different matrix element, ρ_{mn}, however, is assigned its own rate constant, $1/T_{mn}$. This condition of $T_{mn} >> 1/J$ merely means that we do, in fact, have a well-resolved proton doublet to begin with. Furthermore, the requirement is that the real relaxation time $T_{mn} >> 1/J$ and not the apparent $T_{mn}^{*} >> 1/J$ where T_{mn}^{*} is the decay constant taking magnetic field inhomogeneity into account. Thus, this criterion is easily satisfied in our experiment. Next, by using Equations (28) and also Equations (11), which are the ones appropriate for ignoring off-resonance effects, we can determine the following differential equations:

$$\begin{aligned}
\dot{\rho}_{13} &= -i\,(\tfrac{1}{2}J + \Delta\omega)\rho_{13} + i\,\tfrac{1}{2}\omega_1\,\rho_{14} - \frac{1}{T_{13}}\,\rho_{13} \\
\dot{\rho}_{14} &= -i\,(\tfrac{1}{2}J + \Delta\omega)\rho_{14} + i\,\tfrac{1}{2}\omega_1\,\rho_{13} - \frac{1}{T_{14}}\,\rho_{14} \\
\dot{\rho}_{24} &= \;\;i\,(\tfrac{1}{2}J - \Delta\omega)\rho_{24} + i\,\tfrac{1}{2}\omega_1\,\rho_{23} - \frac{1}{T_{24}}\,\rho_{24} \\
\dot{\rho}_{23} &= \;\;i\,(\tfrac{1}{2}J - \Delta\omega)\rho_{23} + i\,\tfrac{1}{2}\omega_1\,\rho_{24} - \frac{1}{T_{23}}\,\rho_{23}
\end{aligned} \tag{29}$$

Again, the initial conditions are the same as in Equations (11). The relevant matrix elements can then be determined to be

$$\begin{aligned}
\rho_{13}(\tau) = \tfrac{1}{2}i(A-C)\; & e^{-i(\frac{1}{2}J+\Delta\omega)\tau}\; e^{-\frac{1}{2}(\frac{1}{T_{13}} + \frac{1}{T_{14}})\tau} \\
& \times \left\{\cos\left[\tfrac{1}{2}\sqrt{\omega_1^{\,2} - \left(\frac{1}{T_{13}} - \frac{1}{T_{14}}\right)^2}\;\tau\right] + \frac{\frac{1}{T_{14}} - \frac{1}{T_{13}}}{\sqrt{\omega_1^{\,2} - \left(\frac{1}{T_{13}} - \frac{1}{T_{14}}\right)^2}}\right. \\
& \left. \sin\left[\tfrac{1}{2}\sqrt{\omega_1^{\,2} - \left(\frac{1}{T_{13}} - \frac{1}{T_{14}}\right)^2}\;\tau\right]\right\}
\end{aligned} \tag{30}$$

$$\rho_{24}(\tau) = \tfrac{1}{2}i(A-C)\, e^{i(\frac{1}{2}J-\Delta\omega)\tau}\, e^{-\frac{1}{2}(\frac{1}{T_{24}} + \frac{1}{T_{23}})\tau}$$

$$\times \{\cos[\tfrac{1}{2}\sqrt{\omega_1^2 - (\tfrac{1}{T_{24}} - \tfrac{1}{T_{23}})^2}\,\tau] + \frac{(\frac{1}{T_{23}} - \frac{1}{T_{24}})}{\sqrt{\omega_1^2 - (\frac{1}{T_{24}} - \frac{1}{T_{23}})^2}}$$

$$\sin[\tfrac{1}{2}\sqrt{\omega_1^2 - (\tfrac{1}{T_{24}} - \tfrac{1}{T_{23}})^2}\,\tau]\}$$

As in the other cases, the Equations (13) for the evolution of the density matrix after the ^{13}C pulse are still applicable. Then by using Equations (13), (30), and (3), we get

$$\langle I_y(2\Delta T)\rangle_{13} = \langle I_y(2\Delta T)\rangle_{\tau=0}\, e^{-\frac{1}{2}(\frac{1}{T_{14}} - \frac{1}{T_{13}})\tau} \{\cos[\tfrac{1}{2}\sqrt{\omega_1^2 - (\tfrac{1}{T_{14}} - \tfrac{1}{T_{13}})^2}\,\tau]$$

$$+ \frac{(\frac{1}{T_{14}} - \frac{1}{T_{13}})}{\sqrt{\omega_1^2 - (\frac{1}{T_{14}} - \frac{1}{T_{13}})^2}} \sin[\tfrac{1}{2}\sqrt{\omega_1^2 - (\tfrac{1}{T_{14}} - \tfrac{1}{T_{13}})^2}\,\tau]\} \qquad (31)$$

$$\langle I_y(2\Delta T)\rangle_{24} = \langle I_y(2\Delta T)\rangle_{\tau=0}\, e^{-\frac{1}{2}(\frac{1}{T_{23}} - \frac{1}{T_{24}})\tau} \{\cos[\tfrac{1}{2}\sqrt{\omega_1^2 - (\tfrac{1}{T_{23}} - \tfrac{1}{T_{24}})^2}\,\tau]$$

$$+ \frac{(\frac{1}{T_{23}} - \frac{1}{T_{24}})}{\sqrt{\omega_1^2 - (\frac{1}{T_{23}} - \frac{1}{T_{24}})^2}} \sin[\tfrac{1}{2}\sqrt{\omega_1^2 - (\tfrac{1}{T_{23}} - \tfrac{1}{T_{24}})^2}\,\tau]\}$$

$$\langle I_x(2\Delta T)\rangle_{13} = \langle I_x(2\Delta T)\rangle_{24} = 0$$

where we note that $\langle I_y(2\Delta T)\rangle_{\tau=0}$ now implicitly includes an overall relaxation term $\exp(-2\Delta T/T_{13})$.

After examination of Equations (31), we see that the effects of the relaxation are three-fold. First, we see that there is an exponential damping or increasing of the amplitude of the peak, depending on the difference of the two relaxation rates. For the case of $\langle I_y(2\Delta T)\rangle_{13}$ we see that the crucial quantity is $(1/T_{14} - 1/T_{13})$. If the two time constants T_{14} and T_{13} are equal, then we see no effects and the magnetization is the same as that in Equation (15). If, however $T_{14} < T_{13}$, then there will be a damping of the amplitude; and if $T_{13} < T_{14}$, then there will be an increase in the peak's amplitude. The second effect of the relaxation is to alter the oscillation frequency; however, this effect is second order in the parameter $R_{13} = (1/T_{14} - 1/T_{13})/\omega_1$. The third effect of the relaxation is to introduce a first order (in R_{13}) term which oscillates like sine rather than cosine. The main effect it has is to uniformly translate the zero-crossings of the amplitudes as it effectively introduces an overall phase error into the oscillating term. This phase of the oscillation is not to be confused with the dispersion - related phase discussed extensively in Section II C of this paper. Although we have not calculated in detail the effects of relaxation and ^{13}C off-resonance effects simultaneously, we feel that we can safely predict the results for small off-resonance parameters by a linear combination of the dispersion phase errors predicted by Equations (25) and (27) and the magnetization predicted by Equations (31).

Fitting the measured amplitude of the peak to the theoretical Equations (31) can yield a value for R_{13}, and knowing ω_1 and T_{13}, this will then yield the relaxation time T_{14}. A similar procedure for the other peak will subsequently yield T_{23} if we know T_{24}. It seems reasonable to assume that

$$T_{13} = T_{24} = (T_2)_I \tag{32}$$

where this just means that the relaxation time constants of the two members of the proton doublet (corresponding to the allowed transitions 1-3 and 2-4) are the same. Furthermore, since these are just the conventional proton T_2's of such a system, we call these times $(T_2)_I$.

In the next section we quantitatively compare theory and experiment and determine values for T_{14} and T_{23}. We also look briefly at some data which show off-resonance effects discussed in Section II C.

III. PRESENTATION AND DISCUSSION OF RESULTS

A. Relaxation Data

In this section we first compare the spin dynamical theory including relaxation, of Section II D, to experimental data. First, we need to rewrite Equations (31) in a slightly more usable form

$$\frac{\langle I_y(2\Delta T)\rangle_{13}}{\langle I_y(2\Delta T)\rangle_{\tau=0}} = e^{-\frac{1}{2}\theta R_{13}}\left\{\cos\left(\tfrac{1}{2}\theta\sqrt{1-R_{13}^2}\right) + \frac{R_{13}}{\sqrt{1-R_{13}^2}}\sin\left(\tfrac{1}{2}\theta\sqrt{1-R_{13}^2}\right)\right\}$$

$$\frac{\langle I_y(2\Delta T)\rangle_{24}}{\langle I_y(2\Delta T)\rangle_{\tau=0}} = e^{-\frac{1}{2}\theta R_{24}}\left\{\cos\left(\tfrac{1}{2}\theta\sqrt{1-R_{24}^2}\right) + \frac{R_{24}}{\sqrt{1-R_{24}^2}}\sin\left(\tfrac{1}{2}\theta\sqrt{1-R_{24}^2}\right)\right\} \tag{33}$$

where we have now normalized the amplitude of each peak to the value for the case of $\tau = 0$. The parameters in Equations (33) have the following values

$$\theta = \omega_1\tau$$

$$R_{13} = \frac{1}{\omega_1}\left(\frac{1}{T_{14}} - \frac{1}{T_{13}}\right) = \frac{1}{\omega_1}\left(\frac{1}{T_{14}} - \left(\frac{1}{T_2}\right)_I\right) \tag{34}$$

$$R_{24} = \frac{1}{\omega_1}\left(\frac{1}{T_{23}} - \frac{1}{T_{24}}\right) = \frac{1}{\omega_1}\left(\frac{1}{T_{23}} - \left(\frac{1}{T_2}\right)_I\right)$$

The assumption of Equation (32) has been used to justify the substitutions for T_{13} and T_{24} in Equations (34) above.

In Figure 4 we have plotted experimental data and the theoretical Equations (33) for various values of the R parameters. Figure 4A shows the experimentally measured amplitude of the peak of the proton formate doublet which was not attenuated for long values of τ (the right-most member of the doublet in Figure 3). Figure 4B shows the experimental amplitudes of the other peak of the doublet which was strongly attenuated for long values of τ (the left-most member of the doublet in Figure 3). In both Figures 4A and B the ratios of the amplitudes of the doublet peaks to the amplitude for the special case of $\tau = 0$ were plotted in order to facilitate direct comparison with Equations (33). Amplitudes were determined from areas of the experimental peaks, and normalization was accomplished by comparison of the ^{1}H impurity peak. The triangles indicate data points for experiments where the echo time, $2\Delta T$, was chosen to be 90 msec while the circles indicate data points for experiments where $2\Delta T$ was chosen to be 280 msec. In all experiments, the same value for the strength of the ^{13}C r.f. pulse, ω_1, was used.

The question now arises as to which of the theoretical Equations (33) corresponds to which of the doublet peaks. The ambiguity arises because we do not know the absolute sign of J; hence, we cannot be sure which of the proton transitions, 1-3 or 2-4, is the lower frequency transition. We have the possibilities of irradiating either the high or low frequency member of the ^{13}C doublet, and the system might react with attenuation of either the high or low frequency member of the proton doublet. Analysis reveals that we can unambiguously assign T_{14} and T_{23}, but we cannot determine the sign of J. Let us consider the four cases of irradiating the high ^{13}C (hi_S) or

low ^{13}C (lo_S) transitions, and observing attenuation of the high ^1H (hi_I) or low ^1H (lo_I) transitions. It turns out that hi_S - hi_I and lo_S - lo_I both predict that $T_{23} < (T_2)_I$, while hi_S - lo_I and lo_S - hi_I predict that $T_{14} < (T_2)_I$. In our case, we experimentally observed only hi_S - hi_I and lo_S - lo_I so we know that $T_{23} < (T_2)_I$.

By the discussion of the preceding paragraph, we now can determine values for R from the data in Figure 4 without worrying about the subscripts on R. Figure 4A has two theoretical curves drawn for R = 0 (solid line) and R = 0.02 (dashed line) from Equations 33. From these curves we determine that R = .01 ± .01. The value for R and the error limits are somewhat subjectively determined by noting that the curves for R = 0 and for R = .02 seem to nicely bound the scatter in the data. In Figure 4B we have drawn theoretical curves for R = .20 (solid line), R = .18 (dashed line), and R = .22 (dotted line). The curve for R = .20 fits the experimental data best, and the curves for R = .18 and R = .22 bound the scatter in the data rather well. So from this we conclude that R = .20 ± .02 for Figure 4B.

We determined ω_1 from the zero crossing of the experimental data in Figure 4A to be $\omega_1/2\pi$ = 17.9 Hz. This procedure is convenient since, for this unattenuated peak, relaxation effects are small and Equations (33) become equivalent to Equations(15). Another option to determine the value for ω_1 would be to measure the length of a 2π pulse by actually observing the ^{13}C magnetization. By conventional methods we measured $(T_2)_I$ to be 160 msec. Thus, from Figure 4A the value of R = .01 ± .01 means that T_{14} = 140 ± 20 msec. The value of R = .20 ± .02 from Figure 4B means that T_{23} = 35 ± 3 msec. Although not crucial to the experiment, for general information we measured the $(T_2)_S$ (this is the ^{13}C T_2) to be 480 msec, the $(T_1)_I$ (normal proton T_1)

to be 4.2 sec, and $(T_1)_S$ (normal ^{13}C T_1) to be 8.7 sec. All of these times are shorter than would be expected in a system purged of dissolved oxygen.

Using this method, it is now possible to directly measure all of the relaxation rates pertaining to the off-diagonal density matrix elements of such a system. In our case the only four unique non-zero rates have the time constants $(T_2)_I$, $(T_2)_S$, T_{14}, and T_{23}. The full Redfield theory[2] says that the general relaxation of the density matrix is of the form

$$\frac{d}{dt} \rho_{mn} = - \sum_{ij} R_{mnij} \rho_{ij} \tag{35}$$

where the R_{mnij} is a super-matrix. Thus, the relaxation of a particular element of the density matrix in general depends on the values of other elements as well. However, according to our assumption of Equation (28), the relaxation of each off-diagonal element depends only on its own value. This is not the case for diagonal elements even if we still assume that the relaxation times are long compared to 1/J. A recent paper of Mayne, et al.[4] shows a very pretty experiment, performed on the same chemical system we used, which measures all of the elements of the super-relaxation rate matrix, R_{mnij}, which pertain to diagonal elements of the density matrix. So, by performing experiments like these as well as the experiments described here, it is possible to map out the values of the entire 16 x 16 relaxation matrix for this AX system. Generalized versions of this phase interferometric spin spectroscopic technique are easy to generate for more complicated systems such as AX_2, etc.

If the decay times of the peaks had been long compared to the length of our ^{13}C pulse (as might have been the case had we removed dissolved oxygen), there would have been several alternatives. First of all, we could have just increased the time τ until relaxation effects were noticeable. Care should

be used in choosing the proper ω_1 because if during the time τ the value of cos $(\omega_1\tau/2)$ undergoes many cycles, then the inhomogeneity of the ^{13}C r.f. magnetic field (ω_1/γ_S) could cause the proton magnetization to dephase, thus giving rise to an effective decay rate which could interfere with the measurement of the relaxation decay. This will not be a problem if the following criterion is maintained

$$\frac{\Delta\omega_1}{\omega_1} \ll R \tag{36}$$

where R is the dimensionless parameter of Equations (34). The symbol $\Delta\omega_1$ stands for the variation of the ^{13}C r.f. perturbation across the sample, so $\Delta\omega_1/\omega_1$ is the fractional r.f. inhomogeneity, determined by the geometry of the r.f. coil. A second alternative to the initial problem would be to stop the ^{13}C pulse at a time when the proton magnetization has completely disappeared. This would correspond to values of $\theta = \omega_1\tau = \pi, 3\pi, 5\pi$, etc. At that time the state of the system would have ρ_{14} and ρ_{23} as the only non-zero off-diagonal matrix elements, and the system would relax with the corresponding times T_{14} and T_{23}. After waiting some appropriately long time one would "retrieve" the proton magnetization by the application of another selective ^{13}C pulse. Measurement of the magnetization would then yield the desired relaxation times. A method similar to this last suggestion was used in a quadrupolar system by Hatanaka, et al.[5] to measure off-diagonal forbidden transition relaxation rates for spin 5/2 nuclei, ^{27}Al in Al_2O_3. Of these two methods the former should work in all cases, while the later is applicable only when

$$J \gg \left(\frac{1}{T_{ij}} - \left(\frac{1}{T_2}\right)_I \right) \qquad \text{for } i,j = 1,4 \text{ and } 2,3 \tag{37}$$

B. Qualitative Off-Resonance Data

In this section we very briefly present two spectra showing some of the off-resonance effects of the spin dynamics described in Section II, C. Figure 5 contains spectra taken for $\omega_1\tau = 2\pi$ in which the ^{13}C radiation is slightly off-resonance. Both types of off-resonance effects contribute to these spectra. For the value of ω_1 stated earlier, we have the important parameter of Equation (27), $x = .092$. This means that if the ^{13}C offset frequency, $\delta\omega$, is zero, there will be an apparent phase error of about 8^o due to the second type of off-resonance effect. The first kind of off-resonance effect then predicts that irradiating the ^{13}C line at $\delta\omega/2\pi = .8$ Hz should produce spectra with no dispersion present. This can be estimated by setting the apparent phase errors from Equations (25) and (27) equal to each other to get

$$\delta\omega = \frac{\omega_1^2}{2J} \tag{38}$$

Thus, we speak of this ^{13}C irradiation frequency as being the apparent resonance frequency.

Figures 5A and B show spectra taken for the values of the ^{13}C irradiation frequency above and below, respectively, the apparent resonance frequency. These spectra were taken 10 Hz apart, so we would expect to see a phase difference of $\frac{1}{2}\,\delta\omega\tau$ equal to about 101^o. It is difficult to determine from the spectra exactly what the phase errors are because this was not done with a high resolution spectrometer, and thus the dispersion phase signals can overlap somewhat. However, we can still estimate that Figure 5A is about 4 Hz above the apparent resonance frequency and Figure 5B is about 6 Hz below, corresponding to phase errors of $+40^o$ and -60^o. Very accurate measurements could, in principle, be made to very precisely determine the apparent ^{13}C resonance frequency.

IV. IMPLICATIONS OF THE EXPERIMENT

We discuss here two important applications of the experiment described in the foregoing sections. One of these is the precise determination of ^{13}C resonance frequencies through the observation of changes in the ^{1}H spectrum, as described in Section II, C. Since the sensitivity of the technique does not depend on the magnetogyric ratio, γ_S, of the S spins it potentially is a highly desirable method for the detection of low-γ spin resonances. The only condition for being able to perform the experiment is that the doublet of the S-spectrum is well resolved, and under the reasonable assumption that J as well as the linewidth (due to field inhomogeneity) is proportional to γ_S, it is clear that the magnitude of γ_S does not impose any limitation on the applicability of the method. The other main application is the measurement of T_2's associated with forbidden transitions, in our case T_{23} and T_{14}. Although we will not give an extensive treatment of the various relaxation mechanisms that possibly might prevail, we wish to illustrate the particular significance of these relaxation times by the following very simple model. Suppose that the spin relaxation of an AX system is caused by randomly fluctuating local fields ΔH_I and ΔH_S at the sites of the nuclei I and S, respectively, and let us assume that these fields are parallel to the external Zeeman field. Defining $\Delta\omega_I(t) = \gamma_I \Delta H_K(t)$ and $\Delta\omega_S(t) = \gamma_S \Delta H_S(t)$, we then have for the fluctuating random Hamiltonian

$$H'(t) = \Delta\omega_I(t)\, I_z + \Delta\omega_S(t)\, S_z \qquad (39)$$

Since only diagonal elements are involved in $H'(t)$, the relaxation rates of the various off-diagonal density matrix elements are given by[3]

$$\frac{1}{T_{mn}} = \overline{(H'_n - H'_m)^2}\,\tau \tag{40}$$

where the bar denotes the ensemble average and τ is the correlation time of the fluctuations. Hence, we find for this simple model

$$\begin{aligned}
\left(\frac{1}{T_2}\right)_I &= \frac{1}{T_{13}} = \frac{1}{T_{24}} = \overline{\Delta\omega_I^2}\,\tau \\
\left(\frac{1}{T_2}\right)_S &= \frac{1}{T_{12}} = \frac{1}{T_{34}} = \overline{\Delta\omega_S^2}\,\tau \\
\frac{1}{T_{23}} &= \left(\overline{\Delta\omega_I^2} + \overline{\Delta\omega_S^2} - \overline{2\Delta\omega_I\Delta\omega_S}\right)\tau \\
\frac{1}{T_{14}} &= \left(\overline{\Delta\omega_I^2} + \overline{\Delta\omega_S^2} + \overline{2\Delta\omega_I\Delta\omega_S}\right)\tau
\end{aligned} \tag{41}$$

While the normal relaxation times depend on $\overline{\Delta\omega_I^2}$ and $\overline{\Delta\omega_S^2}$, which measure the strengths of the fluctuating fields, the times T_{23} and T_{14} are in addition related to $\overline{\Delta\omega_I\,\Delta\omega_S}$. Thus, measurement of the T_2's of forbidden transitions provides information about the cross-correlation between the two local fields. One should be aware that this result strongly depends on the particular relaxation mechanism chosen. For instance, fluctuating fields perperdicular to the Zeemen field with very short correlation times give rise to uniform relaxation rates for all the off-diagonal elements of the density matrix,

$$\left(\frac{1}{T_2}\right)_I = \left(\frac{1}{T_2}\right)_S = \frac{1}{T_{23}} = \frac{1}{T_{14}} = \tfrac{1}{2}\left(\overline{\Delta\omega_I^2} + \overline{\Delta\omega_S^2}\right)\tau \tag{42}$$

Nevertheless, we feel that the physical picture emerging from the first example will have general implications, and that knowledge of relaxation times like T_{23} and T_{14} will be of help in the determination of the detailed nature of molecular motions, such as anisotropic tumbling.

Furthermore, the phase interferometric technique is in general applicable whenever we have a system with two or more inequivalent transitions having one quantum mechanical level in common. It can, for instance, be applied to systems consisting of two coupled nuclear spins, a nucleus and a free electron,or a nucleus with quadrupolar interaction.

REFERENCES

1. M. E. Stoll, A. J. Vega, and R. W. Vaughan, submitted to Physical Review A.
2. A. G. Redfield, IBM J. Res. Develop. 1, 19 (1957); "Advances in Magnetic Resonance"(ed. by J. S. Waugh), Vol. 1, p. 1, Academic Press, New York, 1965.
3. A. Abraham, "Principles of Nuclear Magnetism" Chapter 8, Oxford, Clarendon, 1961.
4. C. L. Mayne, D. W. Alderman, and D. M. Grant, J. Chem. Phys. 63, 2514 (1975).
5. H. Hatanaka, T. Terao, and T. Hashi, J. Phys. Soc. Japan 39, 835 (1975).
6. R. Freeman and W. A. Anderson, J. Chem. Phys. 37, 2053 (1962).

FIGURE CAPTIONS

Figure 1. Energy level diagram for an AX spin system. The α and β represent the two eigenstates spin up and spin down of the spin ½ particle. The first Greek letter represents the state of the ^{1}H spin and the second represents the state of the ^{13}C spin, so that two ^{1}H transitions are shown with single arrows, while the two ^{13}C transitions are shown with double arrows. The numbers 1, 2, 3, 4 are used to refer to the various energy levels or to the eigenstates to which they correspond. The relative Zeeman energies for ^{1}H (56.4 MHz) and ^{13}C (14.2 Mhz) have been drawn to scale, but the effects of the weak coupling have been greatly exaggerated for emphasis.

Figure 2. Radio frequency pulse sequence used. A $\pi/2$ pulse is applied to both ^{1}H transitions. Then a selective pulse of length τ is applied to only one of the ^{13}C transitions. A π pulse is then applied to both ^{1}H transitions at a time ΔT after the $\pi/2$ pulse, which creates a spin echo at a time $2\Delta T$ after the $\pi/2$ pulse. The signal is recorded from $2\Delta T(t = 0)$, defined to be the middle of the echo for Fourier transformation.

Figure 3. Proton phase interferometric spectra for different values of τ. The doublet split by 195 Hz is due to the ^{1}H coupled to the ^{13}C in those formate ions containing ^{13}C. The small peak at the center of the doublet is due to the ^{1}H in the formate ions containing spinless ^{12}C, while the large peak on the far left is due to the small amount of ^{1}H impurity in the solvent. The five spectra are for values of τ = 0, 28, 56, 84, and 112 msec, corresponding to values of $\omega_1\tau = 0^{o}$, 180^{o}, 360^{o}, 540^{o}, and 720^{o}.

Figure 4. Comparison of experimental and theoretical values of the amplitudes of the peaks of the proton doublet vs. the value of $\theta = \omega_1\tau$. The amplitudes of the peaks are plotted on the vertical axis, normalized to the peak amplitude for the special case of $\tau = 0$. The value of $\omega_1\tau$ (in degrees) is plotted on the horizontal axis. The triangles indicate experimental data for which the echo time ($2\Delta T$) was 90 msec, and the circles are for $2\Delta T$ = 280 msec. In all cases the same value of ω_1 = 112 rad/sec was used.

A. This solid line corresponds to the theory for the value of the parameter R = 0. The dashed line represents the theory for R = .02.

B. The solid line represents theory for R = .20, the dashed line is R = .18, and the dotted line is R = .22.

Figure 5. Proton phase interferometric spectra (for $\theta = \omega_1\tau = 360^o$) showing ^{13}C off-resonance effects.

A. This spectrum was taken with the ^{13}C irradiation about 4 Hz above the apparent ^{13}C resonance, thus the doublet shows a phase error of about + 40^o.

B. This spectrum was taken with the ^{13}C irradiation about 6 Hz below the apparent ^{13}C resonance, thus the doublet shows a phase error of about - 60^o.

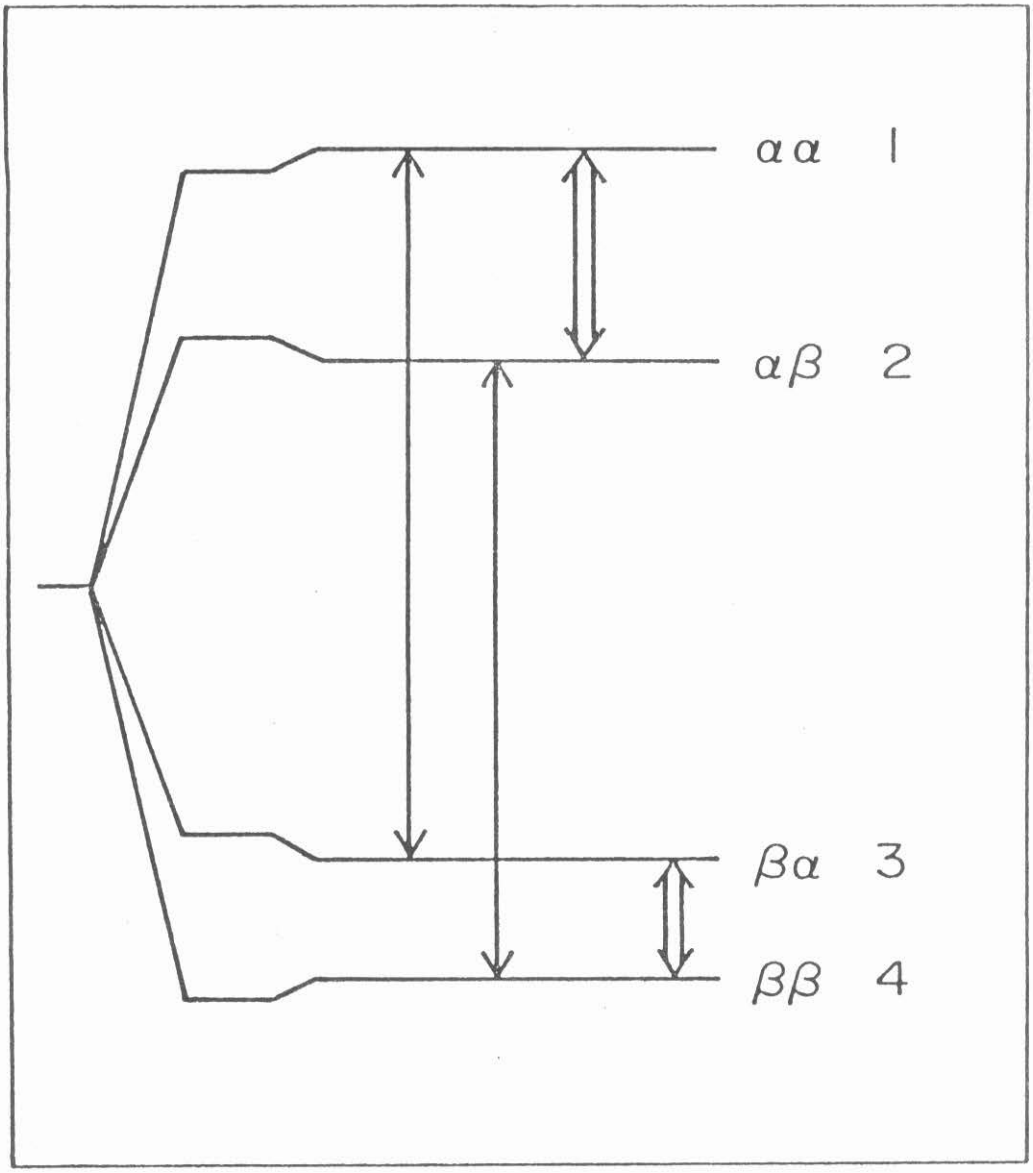

Fig. 1

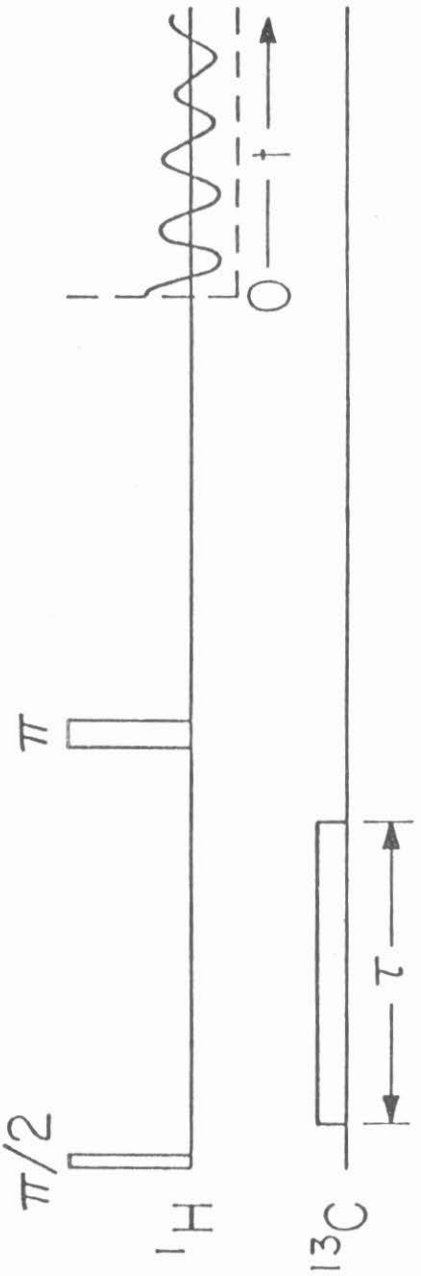

Fig. 2

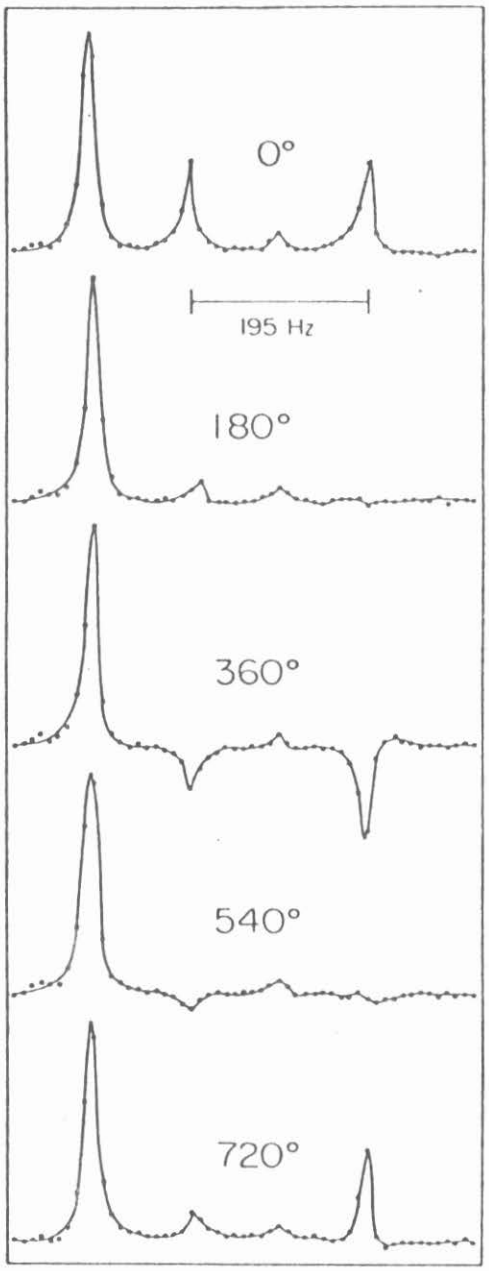

Fig. 3

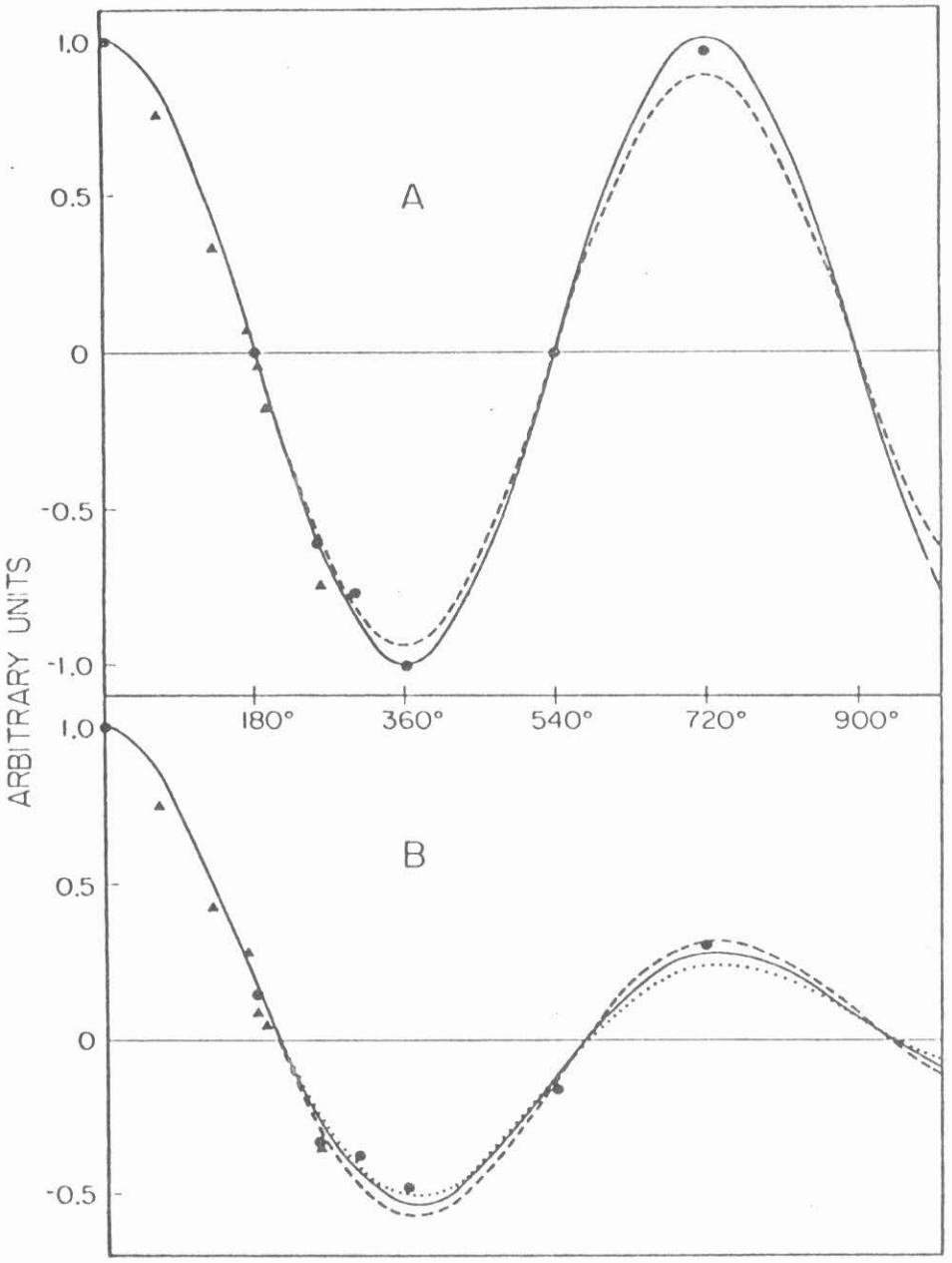

Fig. 4

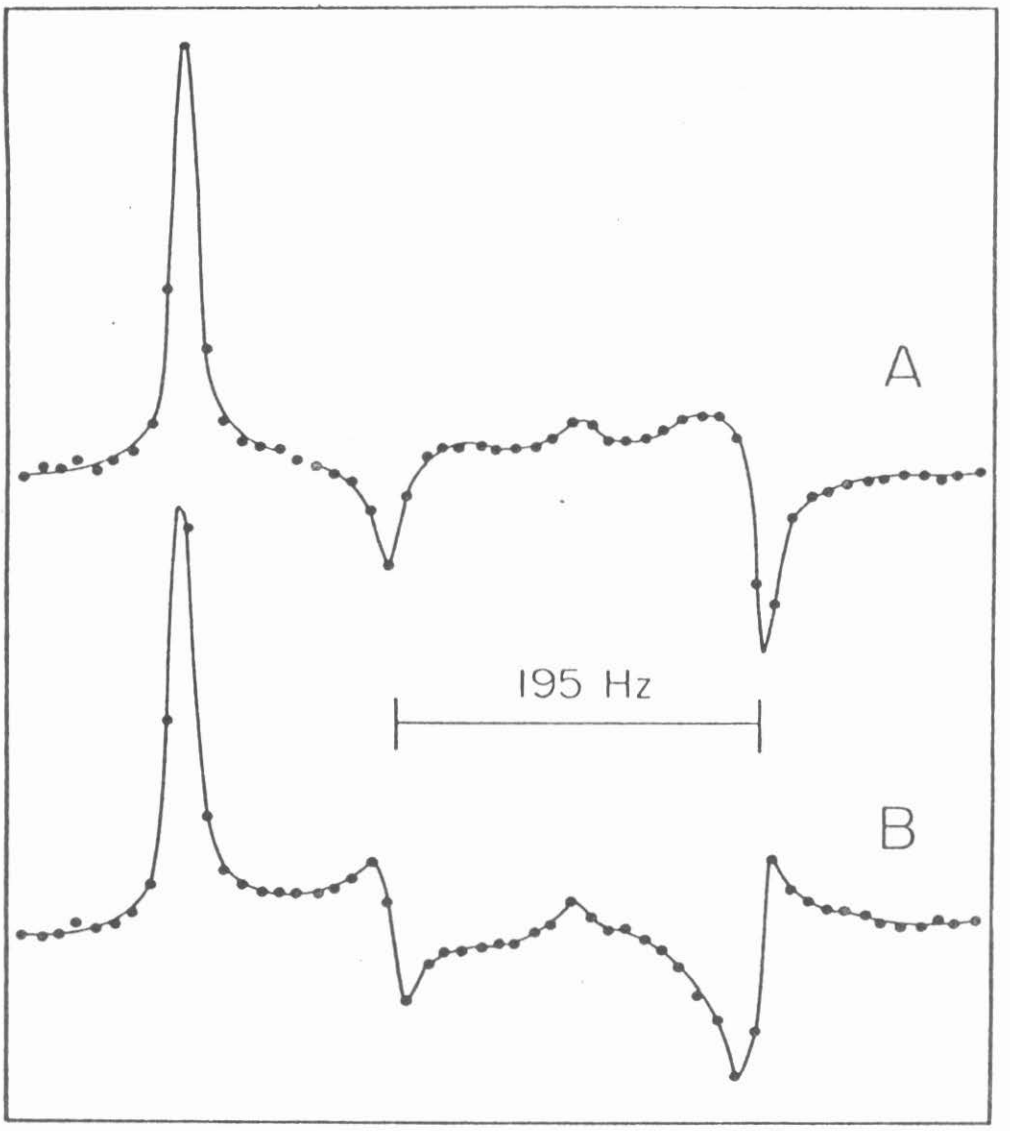

Fig. 5

CHAPTER 5

BASIC THEORY FOR THE EXPERIMENTS UTILIZING DIPOLAR OSCILLATIONS

I. Introduction

Beginning with the cross-polarization decoupling experiments of Pines, et al.[1], there has been renewed interest in nuclear magnetic double resonance experiments. There had been, for quite a while in fact, interest in liquid NMR experiments utilizing CW techniques like the nuclear Overhauser effect (NOE)[2] and spin-tickling[3]; however, this resurgence was focused on pulsed methods in solids which utilized the dipole-dipole interaction.

Our particular thrust in this area was aimed at developing such pulsed NMR experiments which could yield geometrical and perhaps motional information in polycrystalline materials. Chapters 7 and 8 describe experiments which do just that by using the heteronuclear and homonuclear dipole interactions, respectively. (Chapter 7 uses systems containing ^{13}C - ^{1}H, and Chapter 8 uses a ^{1}H - ^{1}H system.) Chapter 6 describes an important set of experiments which set the stage for the work of the subsequent two chapters. It is the purpose of this chapter to examine the theory, in detail, of the spin dynamics of the dipole-dipole interaction, in order to facilitate understanding of the experiments in Chapters 6, 7, and 8 of this thesis.

II. Spin Dynamics of the Heteronuclear Dipolar Hamiltonian

A. Theoretical

By spin dynamics, we mean the actual time development of a quantum mechanical system. This means, essentially, that we are interested in the solution to the time-dependent Schroedinger equation rather than the time-independent Schroedinger equation. So, since we want to solve this equation, let us first look at the actual Hamiltonian involved.

Two spins interact via the direct dipole-dipole Hamiltonian

$$H_{IS} = \frac{\gamma_I \gamma_S}{r^3} \left(\underset{\sim}{I} \cdot \underset{\sim}{S} - 3(\underset{\sim}{I} \cdot \hat{r})(\underset{\sim}{S} \cdot \hat{r}) \right) \qquad (1)$$

where r is the distance between the two spins, γ_I and γ_S are the magnetogyric ratios of the spins I and S, $\underset{\sim}{I}$ and $\underset{\sim}{S}$ are dimensionless spin angular momentum operators, $\hat{r}$ is the unit vector pointing in the direction from I to S, and factors of $\hbar$ are ignored. Since we are doing these experiments in a large magnetic field, H_o (about 14 kG) along the z-axis, we have a large Zeeman interaction

$$H_z = \omega_I I_z + \omega_S S_z \qquad (2)$$

where $\omega_I = \gamma_I H_o$ and $\omega_S = \gamma_S H_o$. Since the dipolar fields are only on the order of 10G, the Zeeman interaction is much larger, and we keep only the secular part of H_{IS}, that part which commutes with H_z. When $|\omega_I - \omega_S| >> \omega_D$, where ω_D is the dipolar frequency, we speak of "inequivalent" spins I and S. In this case, the secular or truncated dipolar Hamiltonian is

$$H_{IS(secular)} = \frac{\gamma_I \gamma_S}{r^3} (1 - 3\cos^2\theta) I_z S_z \qquad (3)$$

where θ is the angle between $\underset{\sim}{r}$ and the z-axis. From now on when we refer to H_{IS}, we will mean this secular Hamiltonian. If all we needed was to calculate the dynamics of this $I_z S_z$ Hamiltonian, our job would be easy, but unfortunately it is not quite so simple. In the actual experiments we apply periodic and cyclic radiation to the spin system and observe it stroboscopically at certain points in time. To do the time development correctly, we use the Magnus formalism[4]. To lowest order of approximation, this is just average Hamiltonian theory[5,6]. (We do not consider higher-order approximation in

this work, for the most part.) Thus, application of the radiation modifies the average dipolar Hamiltonian in the interaction frame of the radiation so that we no longer have just the form $I_z S_z$.

We now consider the general forms of all such interactions for our two spins I and S. For simplicity of calculation, we will assume $I = \frac{1}{2}$ and $S = \frac{1}{2}$, and thus all of our theory will only be applicable for spin $\frac{1}{2}$ particles. Since we have two spin $\frac{1}{2}$ particles, we can describe our system with a set of four basis states, which we will choose as $\alpha\alpha$, $\alpha\beta$, $\beta\alpha$, and $\beta\beta$ or 1, 2, 3, and 4. The α and β refer to states having a z-component of angular momentum of $+\frac{1}{2}$ and $-\frac{1}{2}$, and the first Greek letter refers to the I spin while the second refers to S. Thus, we can describe our system with a 4 x 4 density matrix. Any Hamiltonian that acts in this space can be written as a linear combination of a set of 16 matrices. One can consider SU4 symmetry or many other schemes to choose these 16 matrices, but we feel that the easiest and most straightforward concept is to consider the direct product symmetry of two SU2 groups and to incorporate the concept of irreducible tensors. This is essentially a sophisticated way of referring to a very obvious and simple idea which says that any Hamiltonian, $H_{\text{general IS}}$, which operates on these two spins is of the form

$$H_{\text{general IS}} = a + \sum_i b_i I_i + \sum_j c_j S_j + \sum_{mn} d_{mn} I_m S_n \qquad (4)$$

where i, j, m, and n are summed over values of 1, 2, and 3 corresponding to x, y, and z, and a, b_i, c_j, and d_{mn} are constants.

Note that we have a total of 16 constants which are the coefficients of the 16 matrices. A slight rewriting emphasizes the irreducible tensor idea

$$H_{\text{general IS}} = a + \underset{\sim}{b} \cdot \underset{\sim}{I} + \underset{\sim}{c} \cdot \underset{\sim}{S} + e\, \underset{\sim}{I} \cdot \underset{\sim}{S} + \underset{\sim}{f} \cdot (\underset{\sim}{I} \times \underset{\sim}{S}) + \underset{\sim}{g} \cdot (\underset{\sim\sim}{IS}) \cdot \underset{\sim}{h} \qquad (5)$$

where a, $\underset{\sim}{b}$, $\underset{\sim}{c}$, e, $\underset{\sim}{f}$, $\underset{\sim}{g}$, and $\underset{\sim}{h}$ are a set of 17 constants, of which only 16 are independent. The symbol $(\underset{\sim}{\underset{\sim}{IS}})$ in Equation 5 is understood to be the symmetric dyadic

$$(\underset{\sim}{I}\ \underset{\sim}{S}) = \begin{bmatrix} I_x S_x & \frac{I_x S_y + I_y S_x}{2} & \frac{I_x S_z + I_z S_x}{2} \\ \frac{I_x S_y + I_y S_x}{2} & I_y S_y & \frac{I_y S_z + I_z S_y}{2} \\ \frac{I_x S_z + I_z S_x}{2} & \frac{I_y S_z + I_z S_y}{2} & I_z S_z \end{bmatrix} \tag{6}$$

By setting Equations 4 and 5 equal to each other we get the following relation

$$d_{ij} = \tfrac{1}{2}(g_i h_j + g_j h_i) + \delta_{ij}\, e + \sum_k \varepsilon_{ijk}\, f_k \tag{7}$$

Equation 5 shows the irreducible tensor character clearly because the $\underset{\sim}{I} \cdot \underset{\sim}{S}$ term will transform like the zeroth-order spherical harmonic, the $\underset{\sim}{I} \times \underset{\sim}{S}$ term will transform like the first-order spherical harmonics, and the $(\underset{\sim}{\underset{\sim}{IS}})$ term will transform like the second-order spherical harmonics.

All of this is fine for the consideration of the general form for our average Hamiltonian; however, it is not extremely useful in actual calculations. It seems as though a difficult calculation is not assuaged by the pressure of more sophisticated mathematics in this case. In addition, this formalism can obscure the physical interpretation of the experiments somewhat. So we shall attack the problem of the spin dynamics of such Hamiltonians by explicit calculation with particular representative Hamiltonians. It turns out that any average Hamiltonian can cause really only four types of physical phenomena: 1) no behavior at all, 2) precession of magnetization, 3) linear oscillation of magnetization, and 4) transfer of magnetization between the

I and S spins.

This first phenomenon is not as trivial as it might at first seem to be. In order to cause no change in the spin system, we need to have an average Hamiltonian in which all the constants except "a" of Equation 4 are zero. We focus in particular on making the $d_{mn} = 0$. Since we are starting out with $H_{IS} \propto I_z S_z$, this means we must manipulate the Hamiltonian in the interaction frame of the radiation to average to zero. This is the "decoupling" criterion in which $\overline{H}^{(o)}_{IS} = 0$, where the bar and the superscript zero indicate the zeroth order term of the Magnus expansion, which is the average Hamiltonian. In the experiments of Hartmann and Hahn[7], a well-known double resonance matching condition was introduced. This was essentially just a condition which gave $\overline{H}^{(o)}_{IS}$ a particular form which caused mutual effects between the spins. The proper generalization of this condition is that the two spins will be coupled whenever $\overline{H}^{(o)}_{IS} \neq 0$[8].

The second phenomenon is precession of magnetization. For instance, suppose we have an average Hamiltonian of the form:

$$\overline{H}^{(o)} = bI_z + cS_z \tag{8}$$

To calculate the dynamics of this situation we use the Liouville equation for the evolution of the density matrix viewed stroboscopically in the interaction frame [5,6]

$$\dot{\rho} = i\,[\rho, \overline{H}^{(o)}] \tag{9}$$

Since $\overline{H}^{(o)}$ is not explicitly a function of time, the solution for $\rho(t)$ is straightforward

$$\rho(t) = e^{-i\overline{H}^{(o)}t}\,\rho(0)\,e^{+i\overline{H}^{(o)}t} \tag{10}$$

We have merely to use this to calculate the magnetization from the following equation

$$\langle M(t)\rangle = \mathrm{tr}\,(\rho(t)\,M) \tag{11}$$

where $M = I_x, I_y, I_z, S_x, S_y, S_z$.

All of our initial states in these experiments correspond to spin systems either in thermal equilibrium, thus having magnetization along the z-axis, or with some non-zero transverse magnetization, created by a very short r.f. pulse. Thus, we have, in general, for spin ½ particles

$$\rho(0) = 1 + K_{I_x} I_x + K_{I_y} I_y + K_{I_z} I_z + K_{S_x} S_x + K_{S_y} S_y + K_{S_z} S_z \tag{12}$$

Using Equations 10 and 12 we have

$$\begin{aligned}\rho(t) = 1 &+ K_{I_x} (I_x \cos(bt) + I_y \sin(bt)) \\ &+ K_{I_y} (I_y \cos(bt) - I_x \sin(bt)) \\ &+ K_{I_z} I_z \\ &+ K_{S_x} (S_x \cos(ct) + S_y \sin(ct)) \\ &+ K_{S_y} (S_y \cos(ct) - S_x \sin(ct))\end{aligned} \tag{13}$$

So we then observe magnetization calculated from Equation 11

$$\langle I_x(t)\rangle = \langle I_x\rangle_o \cos(bt) - \langle I_y\rangle_o \sin(bt)$$

$$\langle I_y(t)\rangle = \langle I_y\rangle_o \cos(bt) + \langle I_x\rangle_o \sin(bt)$$

$$\langle I_z(t)\rangle = \langle I_z\rangle_o$$

$$\langle S_x(t)\rangle = \langle S_x\rangle_o \cos(ct) - \langle S_y\rangle_o \sin(ct) \tag{14}$$

$$\langle S_y(t)\rangle = \langle S_y\rangle_o \cos(ct) + \langle S_x\rangle_o \sin(ct)$$

$$\langle S_z(t)\rangle = \langle S_z\rangle_o$$

where the subscript zero refers to values at t = 0. Thus we see the x- and y-magnetizations precess about the z-axis, but the z-magnetization is static. Any Hamiltonian of the form

$$\overline{H}^{(o)} = \underset{\sim}{b} \cdot \underset{\sim}{I} + \underset{\sim}{c} \cdot \underset{\sim}{S} \tag{15}$$

will exhibit such precession of the I and S magnetizations. There is always some general transformation of coordinates which can bring it to the form of Equation 8.

The third kind of phenomenon is linear oscillation of the magnetization. The Hamiltonian causing this behavior is of the form

$$\overline{H}^{(o)}_{IS} = B\, I_z\, S_z \tag{16}$$

In order to calculate the effects of these and later Hamiltonians, we rely heavily on the following relations which hold true only for spin ½ particles

$$I_x^2 = I_y^2 = I_z^2 = \tfrac{1}{4}$$

$$I_x I_y = -\, I_y I_x = \tfrac{1}{2}\, i\, I_z$$

$$I_y I_z = -\, I_z I_y = \tfrac{1}{2}\, i\, I_x \tag{17}$$

$$I_z I_x = -\, I_x I_z = \tfrac{1}{2}\, i\, I_y$$

We can use Equations 17 to calculate

$$e^{iBtI_zS_z} = \cos(\tfrac{1}{4}Bt) + 4\,i\,I_z\,S_z \sin(\tfrac{1}{4}Bt) \tag{18}$$

From Equations 10, 12, 16, and 18 we have

$$\begin{aligned}\rho(t) = 1 &+ K_{I_x}\{I_x \cos(\tfrac{1}{2}Bt) + 2\,I_y\,S_z \sin(\tfrac{1}{2}Bt)\}\\ &+ K_{I_y}\{I_y \cos(\tfrac{1}{2}Bt) - 2\,I_x\,S_z \sin(\tfrac{1}{2}Bt)\}\\ &+ K_{I_z}\,I_z\\ &+ K_{S_x}\{S_x \cos(\tfrac{1}{2}Bt) + 2\,S_y\,I_z \sin(\tfrac{1}{2}Bt)\}\\ &+ K_{S_y}\{S_y \cos(\tfrac{1}{2}Bt) - 2\,S_x\,I_z \sin(\tfrac{1}{2}Bt)\}\\ &+ K_{S_z}\,S_z\end{aligned} \tag{19}$$

Using Equations19 and 11 we get

$$\begin{aligned}\langle I_x(t)\rangle &= \langle I_x\rangle_o \cos(\tfrac{1}{2}Bt)\\ \langle I_y(t)\rangle &= \langle I_y\rangle_o \cos(\tfrac{1}{2}Bt)\\ \langle I_z(t)\rangle &= \langle I_z\rangle_o\\ \langle S_x(t)\rangle &= \langle S_x\rangle_o \cos(\tfrac{1}{2}Bt)\\ \langle S_y(t)\rangle &= \langle S_y\rangle_o \cos(\tfrac{1}{2}Bt)\\ \langle S_z(t)\rangle &= \langle S_z\rangle_o\end{aligned} \tag{20}$$

So we see that the $I_z\,S_z$ Hamiltonian causes x and y components of I and S magnetization to linearly oscillate rather than precess, as was the case

for simply I_z or S_z Hamiltonians. This can be explained in terms of a very physical model which we shall introduce later in this chapter. Any Hamiltonian of the form

$$\bar{H}^{(o)}_{IS} = (d_1 I_x + d_2 I_y + d_3 I_z)\cdot(d_4 S_x + d_5 S_y + d_6 S_z) \tag{21}$$

can be brought by a transformation to the form of Equation 16; thus, all such Hamiltonians cause such oscillatory behavior.

The fourth kind of behavior is transfer of magnetization between the I and S spins. The Hamiltonian causing such transfer is of the form

$$\bar{H}^{(o)}_{IS} = B I_z S_z + C I_y S_y \tag{22}$$

In the course of the calculation we make important use of the fact that for spin ½ particles

$$[I_z S_z, I_y S_y] = 0 \tag{23}$$

and thus

$$e^{i(BtI_z S_z + CtI_y S_y)} = e^{iBtI_z S_z} e^{iCtI_y S_y} \tag{24}$$

From Equations 24, 22, 12, and 10, we find

$$\begin{aligned}\rho(t) = 1 &+ K_{I_x}\{I_x \cos(\tfrac{1}{2}Bt)\cos(\tfrac{1}{2}Ct) + 2I_y S_z \sin(\tfrac{1}{2}Bt)\cos(\tfrac{1}{2}Ct) \\ &\quad + S_x \sin(\tfrac{1}{2}Bt)\sin(\tfrac{1}{2}Ct) - 2I_z S_y \cos(\tfrac{1}{2}Bt)\sin(\tfrac{1}{2}Ct)\} \\ &+ K_{I_y}\{I_y \cos(\tfrac{1}{2}Bt) - 2 I_x S_z \sin(\tfrac{1}{2}Bt)\} \\ &+ K_{I_z}\{I_z \cos(\tfrac{1}{2}Ct) + 2 I_x S_y \sin(\tfrac{1}{2}Ct)\}\end{aligned} \tag{25}$$

$$+ K_{S_x} \{S_x \cos(\tfrac{1}{2} Bt) \cos(\tfrac{1}{2} Ct) + 2 S_y I_z \sin(\tfrac{1}{2} Bt) \cos(\tfrac{1}{2} Ct)$$
$$+ I_x \sin(\tfrac{1}{2} Bt) \sin(\tfrac{1}{2} Ct) - 2 S_z I_y \cos(\tfrac{1}{2} Bt) \sin(\tfrac{1}{2} Ct)\}$$
$$+ K_{S_y} \{S_y \cos(\tfrac{1}{2} Bt) - 2 S_x I_z \sin(\tfrac{1}{2} Bt)\}$$
$$+ K_{S_z} \{S_z \cos(\tfrac{1}{2} Ct) + 2 S_x I_y \sin(\tfrac{1}{2} Ct)\}$$

And then from Equation 11 we find

$$\begin{aligned}
\langle I_x(t)\rangle &= \langle I_x\rangle_o \cos(\tfrac{1}{2} Bt) \cos(\tfrac{1}{2} Ct) + \langle S_x\rangle_o \sin(\tfrac{1}{2} Bt) \sin(\tfrac{1}{2} Ct) \\
\langle I_y(t)\rangle &= \langle I_y\rangle_o \cos(\tfrac{1}{2} Bt) \\
\langle I_z(t)\rangle &= \langle I_z\rangle_o \cos(\tfrac{1}{2} Ct) \\
\langle S_x(t)\rangle &= \langle S_x\rangle_o \cos(\tfrac{1}{2} Bt) \cos(\tfrac{1}{2} Ct) + \langle I_x\rangle_o \sin(\tfrac{1}{2} Bt) \sin(\tfrac{1}{2} Ct) \\
\langle S_y(t)\rangle &= \langle S_y\rangle_o \cos(\tfrac{1}{2} Bt) \\
\langle S_z(t)\rangle &= \langle S_z\rangle_o \cos(\tfrac{1}{2} Ct)
\end{aligned} \tag{26}$$

These equations show that a Hamiltonian of the form of Equation 22 causes x-magnetization to be transferred oscillatorily between the I and S spins, while y- and z-magnetization merely oscillates as in the third phenomenon. For the simple case of B = C,

$$\begin{aligned}
\langle I_x(t)\rangle &= \langle I_x\rangle_o \tfrac{1}{2} (1 + \cos(Bt)) + \langle S_x\rangle_o \tfrac{1}{2} (1 - \cos(Bt)) \\
\langle S_x(t)\rangle &= \langle S_x\rangle_o \tfrac{1}{2} (1 + \cos(Bt)) + \langle I_x\rangle_o \tfrac{1}{2} (1 - \cos(Bt))
\end{aligned} \tag{27}$$

and we observe that the magnetization oscillates between the I and S spins

with a frequency of B.

A slightly more general form of the Hamiltonian

$$\overline{H}^{(o)}_{IS} = B\, I_z\, S_z + C\, I_y\, S_y + D\, I_x\, S_x \tag{28}$$

ultimately leads to

$$\begin{aligned}
\langle I_x(t)\rangle &= \langle I_x\rangle_o \cos(\tfrac{1}{2}Bt)\cos(\tfrac{1}{2}Ct) + \langle S_x\rangle_o \sin(\tfrac{1}{2}Bt)\sin(\tfrac{1}{2}Ct)\\
\langle I_y(t)\rangle &= \langle I_y\rangle_o \cos(\tfrac{1}{2}Bt)\cos(\tfrac{1}{2}Dt) + \langle S_y\rangle_o \sin(\tfrac{1}{2}Bt)\sin(\tfrac{1}{2}Dt)\\
\langle I_z(t)\rangle &= \langle I_z\rangle_o \cos(\tfrac{1}{2}Ct)\cos(\tfrac{1}{2}Dt) + \langle S_z\rangle_o \sin(\tfrac{1}{2}Ct)\sin(\tfrac{1}{2}Dt)\\
\langle S_x(t)\rangle &= \langle S_x\rangle_o \cos(\tfrac{1}{2}Bt)\cos(\tfrac{1}{2}Ct) + \langle I_x\rangle_o \sin(\tfrac{1}{2}Bt)\sin(\tfrac{1}{2}Ct)\\
\langle S_y(t)\rangle &= \langle S_y\rangle_o \cos(\tfrac{1}{2}Bt)\cos(\tfrac{1}{2}Dt) + \langle I_y\rangle_o \sin(\tfrac{1}{2}Bt)\sin(\tfrac{1}{2}Dt)\\
\langle S_z(t)\rangle &= \langle S_z\rangle_o \cos(\tfrac{1}{2}Ct)\cos(\tfrac{1}{2}Dt) + \langle I_z\rangle_o \sin(\tfrac{1}{2}Ct)\sin(\tfrac{1}{2}Dt)
\end{aligned} \tag{29}$$

So we see that this form of the Hamiltonian causes oscillatory transfer of x, y, and z components of magnetization.

These four effects represent the only types of behavior that a coupled spin ½ system can exhibit. Of course, complications can arise when there are Hamiltonians of several different types acting simultaneously. These problems become very complicated and unless specific experiments warrant it, examination of such situations should be avoided. In the crucial experiment described in Chapter 7, the Hamiltonian is of the form:

$$\overline{H}^{(o)} = B\, I_z\, S_z + C\, S_z + D\, I_z \tag{30}$$

This form is particularly simple because all the terms mutually commute. This means that we could compute the effects of all three separately, with

no real increase in work. Also, since we were observing transverse magnetization of the S spins, we were able to remove all the effects due to the C S_z term with a normal spin echo, leaving only the effects of the B I_z S_z term.

An idea we plan to try soon is to use a phase-altered multiple pulse cycle to create a Hamiltonian of the form

$$\bar{H}^{(o)} = B\ I_z\ S_z + D\ I_z + E\ I_y \tag{31}$$

This will lead to

$$\begin{aligned}
&\frac{\langle S_x(t)\rangle}{\langle S_x\rangle_o} = c\cos\left(\tfrac{1}{2}(\omega_+ - \omega_-)\,t\right) + d\cos\left(\tfrac{1}{2}(\omega_+ + \omega_-)\,t\right)\\
&\omega_\pm = \sqrt{(\tfrac{1}{2}B \pm D)^2 + E^2}\\
&c = \frac{1}{4}\,\frac{\{E^2 - ((\tfrac{1}{2}B + D) - \omega_+)\,((\tfrac{1}{2}B - D) + \omega_-)\}^2}{\{\omega_+^{\,2} - \omega_+(\tfrac{1}{2}B + D)\}\{\omega_-^{\,2} + \omega_-(\tfrac{1}{2}B - D)\}}\\
&d = 1 - c
\end{aligned} \tag{32}$$

For the limiting case that D = 0, Equation 32 becomes

$$\frac{\langle S_x(t)\rangle}{\langle S_x\rangle_o} = \frac{E^2}{E^2 + (\tfrac{1}{2}B)^2} + \frac{(\tfrac{1}{2}B)^2}{E^2 + (\tfrac{1}{2}B)^2}\cos\left(\sqrt{(\tfrac{1}{2}B)^2 + E^2}\ \ t\right) \tag{33}$$

This shows that if $\frac{1}{2}B \gg E$, then the magnetization oscillates with essentially the frequency $\frac{1}{2}B$, and if $E \gg \frac{1}{2}B$, then it does not oscillate. This is possibly very useful because we would like to observe oscillations in the magnetization due to the B I_z S_z term. However, if we have one S spin and more than one I spin in our system, we can get destructive interference due to the various local fields the I spins create at the site of the S spin. But by choosing the size of E to be small compared to $\frac{1}{2}B$ for some of the I

spins and large compared to $\frac{1}{2}B$ for other I spins, we hope to essentially remove the effects of distant I spins while only slightly modifying the effects of close I spins in a predictable manner, thus giving us better "resolution" in determining dipolar frequencies in solids.

The problem of one S spin and more than one I spin is, in general, not an easy one to handle. The first two phenomena described earlier, decoupling and precession of magnetization, are straightforward to adapt to more than one I spin; however, the situation is more difficult for the oscillation and transfer phenomena. For a system of one spin of type S and N spins of type I, we consider the following average Hamiltonian

$$\bar{H}_{IS}^{(o)} = \sum_{j=1}^{N} B_j \, I_{jz} \, S_z \tag{34}$$

This leads to the following

$$\begin{aligned}
\langle I_{jx}(t)\rangle &= \langle I_{jx}\rangle_o \cos(\tfrac{1}{2} B_j t) \\
\langle I_{jy}(t)\rangle &= \langle I_{jy}\rangle_o \cos(\tfrac{1}{2} B_j t) \\
\langle I_{jz}(t)\rangle &= \langle I_{jz}\rangle_o \\
\langle S_x(t)\rangle &= \langle S_x\rangle_o \prod_{j=1}^{N} \cos(\tfrac{1}{2} B_j t) \\
\langle S_y(t)\rangle &= \langle S_y\rangle_o \prod_{j=1}^{N} \cos(\tfrac{1}{2} B_j t) \\
\langle S_z(t)\rangle &= \langle S_z\rangle_o
\end{aligned} \tag{35}$$

So for the linear oscillating case, we see that each I magnetization oscillates only with its own dipolar frequency and "sees" only the S spin and not other I spins. However, the S magnetization oscillates as the product of cosines

of all of the dipolar frequencies, thus giving rise to sum and difference frequencies of the various dipolar frequencies present.

The extension of the transfer phenomenon to more than one I spin is even more difficult. For the system of one S spin and two I spins consider the Hamiltonian

$$\bar{H}_{IS}^{(o)} = B_1(I_{1z}\, S_z + I_{1y}\, S_y) + B_2(I_{2z}\, S_z + I_{2y}\, S_y) \tag{36}$$

The resulting time development of the magnetization is very complex and we state the results only for the case

$$\begin{aligned} \rho(0) &= 1 + K_{Ix}(I_{1x} + I_{2x}) \\ \langle I_{1x}\rangle_o &= \langle I_{2x}\rangle_o \equiv \langle I_x\rangle_o \end{aligned} \tag{37}$$

In this case we find that

$$\begin{aligned} \langle I_{1x}(t)\rangle &= \langle I_x\rangle_o \{1 + \tfrac{1}{2} \frac{B_1^2}{B_1^2 + B_2^2} (\cos(\sqrt{B_1^2 + B_2^2}\, t) - 1)\} \\ \langle I_{2x}(t)\rangle &= \langle I_x\rangle_o \{1 + \tfrac{1}{2} \frac{B_2^2}{B_1^2 + B_2^2} (\cos(\sqrt{B_1^2 + B_2^2}\, t) - 1)\} \\ \langle S_x(t)\rangle &= \langle T_x\rangle_o \tfrac{1}{2} \{1 - \cos(\sqrt{B_1^2 + B_2^2}\, t)\} \end{aligned} \tag{38}$$

so the x-magnetization of both I spins is transferred to the S spin, and the frequency of the transfer back and forth is $\sqrt{B_1^2 + B_2^2}$. The effect of two I spins is to mix the frequencies B_1 and B_2 in a complex manner. For three or more I spins and one S spin the situation gets pretty hopeless. It is for this reason that in the experiments of Chapter 7, we created a Hamiltonian of the form $I_z\, S_z$ and not $I_z\, S_z + I_y\, S_y$. Use of the former allows relatively

simple interpretation of the dipolar oscillations, while use of the latter makes interpretation difficult if not impossible for a number of I spins.

It is instructive to consider the meaning of the terms in Equations 19 and 25 which are bilinear in I and S. These do not correspond to observable magnetization of either the I or S spin. For instance, the term $2 I_y S_z \sin(\frac{1}{2}Bt)$ in Equation 19 corresponds to $\langle I_y S_z \rangle \neq 0$. But $\langle I_z S_z \rangle$ is not equal to $\langle I_y \rangle \langle S_z \rangle$. This term corresponds to a correlation between I_y and S_z, and essentially it means that there is a probability of finding the magnetization of the I spin along the y-axis while finding the magnetization of the coupled S spin along the z-axis. It is a type of cross-product ordering which essentially creates a certain right or left "handedness" between the I and S spins. As might be expected, this order is related to entropy, and the observable magnetization is also a kind of order which is related to entropy. For systems like ours in which we have only a few spins interacting and we do an exact quantum mechanical calculation, we must expect the entropy of the system to be constant. We can use the equation for the entropy, S, as a function of time

$$S(t) = -k_{Boltzmann} \text{ tr } \{\rho(t) \ln(\rho(t))\} \qquad (39)$$

to show that only if these nonobservable terms are taken into account do we have constant entropy. So the entropy is maintained, but it is passed back and forth between the Zeeman order and the heteronuclear dipolar order.

One can use this insight to create a very physical picture of what is occurring in these systems. We can understand an $I_z S_z$ Hamiltonian by assuming that the I spin sees a small magnetic field along the z-axis created by the S spin and vice versa. The I spin precesses about this magnetic field, but

since at normal temperatures half of the S spins are in the "spin up" and half are in the "spin down" state, then half of the I spins precess clockwise and half precess counterclockwise. This leads to a net linear oscillation of the I magnetization due to rotating and counter-rotating components. Thus, there is a correlation between the I magnetization and the S magnetization, and it is precisely this correlation that the nonobservable terms of the density matrix signify. However, this linear oscillation arises from a statistical probability of having initial quantum states "up" and "down", as opposed to arising from a quantum mechanical probability, as the linear oscillations of Chapters 3 and 4 did. Theoretically, one could cool down the spin system to the point where the high temperature Boltzmann approximations are no longer valid, and one could observe net precession as well as linear oscillation, since the rotating and counter-rotating components would no longer be present in equal measure.

B. Experimental

We now discuss briefly some actual pulse sequences which create the various types of Hamiltonians discussed in the theoretical section. We will consider two basic categories: 1) those which do not decouple I spins from each other, and 2) those which do decouple I spins from each other. If we want to see the undulations due to the various I-S Hamiltonians of the last section, we must have uncoupled I-S spin pairs. But if there are many such I-S pairs which are strongly coupled to each other via an I-I interaction, then the S will interact with a many-body "bath" of I spins instead. This situation is not desirable if we are trying to measure the dipolar undulation frequencies due to a single I-S pair. Thus, in Chapter 6 we did experiments of both types 1) and 2) in order to see the effects of this

I-I decoupling. In Chapter 7 we did experiments decoupling I spins in order to accurately measure dipolar oscillation. Chapter 8 contains a homonuclear version of a dipolar oscillation experiment in which we did not decouple spins but merely chose a system having already isolated I-I pairs.

The first type of experiment we consider is that in which I-I interactions are not suppressed. Figure 1 shows several pulse sequences which could be applied to the I and S spins. Table 1 summarizes the various average Hamiltonians which result from application of these pulse sequences. Note that all of these cause either no change, linear oscillation, or oscillatory transfer as discussed in the theoretical section. One of the experiments of Chapter 6 involved transfer of polarization by the application of a cycle like that of Figure 1B to both I and S spin systems.

The second type of experiment we consider is that in which I-I interactions are suppressed. Figure 2 shows an eight-pulse cycle[9] applied to the I spins while any of five different cycles is applied to the S spins. This I cycle very effectively removes I-I interactions, thus allowing us to clearly see effects of the I-S Hamiltonian. One of the experiments in Chapter 6 involved the application of the eight-pulse cycle to the I spins while applying S3 to the S spins. This caused an oscillatory transfer of magnetization between I and S. The experiments of Chapter 7 involved applying S5 to the S spins. This meant merely applying the eight-pulse cycle to the I spins and doing nothing to the S spins. The resulting Hamiltonian can be transformed to the form $I_z S_z$, and thus it leads to linear oscillation of the magnetization. Another way to achieve similar results would be by application of S2. The sequence S4 is very intriguing because it would transfer any component of magnetization while suppressing I-I and

S-S interactions. We usually have not worried about suppressing S-S interactions due to the normally low isotopic abundance of the S species. The application of S1 not only suppresses I-I interaction but also removes the I-S interaction. This could prove useful in an experiment similar to that of Chapter 7, except that we would observe the I spins instead of the S spins. This would mean that instead of conventional heteronuclear CW decoupling, we would employ a pulsed decoupling like S1, which at the same time suppresses I-I interactions.

Figure 3 shows the first experimental evidence we found of dipolar oscillation. We applied the eight-pulse cycle to the spins (^{19}F) while doing nothing to the S spins (^{207}Pb), which is S5 of Figure 2. Figure 3 is the Fourier transformation of the dipolar oscillations of the ^{19}F signal. Note that there are "sidebands" at the dipolar frequency. These represent ^{19}F next to ^{207}Pb, while the large center peak represents ^{19}F next to spinless ^{206}Pb or ^{208}Pb.

The pioneering CW off-resonance, magic-angle decoupling experiments of Hester, et al.[10,11] utilize an average Hamiltonian of the form:

$$\bar{H}_{IS}^{(o)} = B \quad \frac{1}{3}\left(I_z - \frac{1}{\sqrt{2}} I_x\right) S_z + \frac{1}{\sqrt{6}} I_y S_y \tag{40}$$

which can be transformed into the form

$$\bar{H}_{IS}^{(o)} = B \frac{1}{\sqrt{6}} \left(I_z S_z + I_y S_y\right) \tag{41}$$

Thus, we see that these experiments involve oscillatory transfer of I and S magnetization, while at the same time suppressing I-I interactions. Later work of Hester, et al.[12] done independently of and simultaneously with the dipolar oscillation experiments of this thesis, utilize a four-pulse cycle to suppress I-I interactions while maintaining an I-S interaction of the form

$$\bar{H}^{(o)}_{IS} = B \frac{1}{3} (I_z + I_x + I_y) S_z \qquad (42)$$

These experiments exhibit linear oscillation rather than oscillatory transfer of magnetization.

The classic CW technique of cross-polarization developed by Hartmann and Hahn[7] and used to enhance signal-to-noise by Pines, et al.[1], is used in a great variety of experiments, including those in Chapter 7. In this technique the I-I interaction is not suppressed, and the average Hamiltonian is of the form

$$\bar{H}^{(o)}_{IS} = \frac{B}{2} (I_z S_z + I_y S_y) \qquad (43)$$

Thus, magnetization is transferred between the I and S spins, but no oscillations are seen because the I spins act as a "bath." The I and S magnetizations quickly reach a steady state value in which both spin baths have the same "temperature." Oscillatory transfer may be seen in rare cases where the I spins are isolated[13].

III. Spin Dynamics of the Homonuclear Dipolar Hamiltonian

For the case of the homonuclear dipolar Hamiltonian, we consider spins I and S to be "equivalent." By this we mean that $|\omega_I - \omega_S| \ll \omega_D$, where ω_D is the dipolar frequency, and ω_I and ω_S are defined by Equation 2. For purposes of clarity, we now set $I = I_1$ and $S = I_2$, since both spins are of the same species. The secular part of the dipolar Hamiltonian now becomes

$$H_{II(secular)} = \tfrac{1}{2} \frac{\gamma_I^2}{r^3} (1 - 3\cos^2\theta) (3 I_{1z} I_{2z} - \underset{\sim}{I}_1 \cdot \underset{\sim}{I}_2) \qquad (44)$$

If we allow this Hamiltonian to operate without application of any radiation, the average Hamiltonian is then of the form

$$\bar{H}^{(o)}_{II} = B (3 I_{1z} I_{2z} - \underset{\sim}{I}_1 \cdot \underset{\sim}{I}_2) \qquad (45)$$

Starting with a density matrix of the form

$$\rho(o) = 1 + K_x (I_{1x} + I_{2x}) + K_y (I_{1y} + I_{2y}) + K_z(I_{1z} + I_{2z})$$

$$\langle I_{1x}\rangle_o = \langle I_{2x}\rangle_o \equiv \langle I_x\rangle_o$$

$$\langle I_{1y}\rangle_o = \langle I_{2y}\rangle_o \equiv \langle I_y\rangle_o \qquad (46)$$

$$\langle I_{1z}\rangle_o = \langle I_{2z}\rangle_o \equiv \langle I_z\rangle_o$$

we find the time development of the density matrix to be

$$\rho(t) = 1 + K_x \{(I_{1x} + I_{2x}) \cos (\tfrac{3}{2} Bt) + 2 (I_{1y} I_{2z} + I_{1z} I_{2y}) \sin (\tfrac{3}{2} Bt)\}$$
$$+ K_y \{(I_{1y} + I_{2y}) \cos (\tfrac{3}{2} Bt) - 2 (I_{1x} I_{2z} + I_{1z} I_{2x}) \sin (\tfrac{3}{2} Bt)\} \qquad (47)$$
$$+ K_z \{I_{1z} + I_{2z}\}$$

This finally leads to equations for the magnetization

$$\langle I_{1x}(t)\rangle = \langle I_{2x}(t)\rangle = \langle I_x\rangle_o \cos (\tfrac{3}{2} Bt)$$

$$\langle I_{1y}(t)\rangle = \langle I_{2y}(t)\rangle = \langle I_y\rangle_o \cos (\tfrac{3}{2} Bt) \qquad (48)$$

$$\langle I_{1z}(t)\rangle = \langle I_{2z}(t)\rangle = \langle I_z\rangle_o$$

So we see that the average Hamiltonian of Equation 45 leads to linear oscillation of magnetization, analogous to the $I_z S_z$ case for the heteronuclear experiments. Note also the nonobservable cross-product order terms in Equation 47. These terms are necessary to conserve entropy, and they indicate a correlation between the two spins I_1 and I_2, just as similar terms did for the case of I and S spins.

Chapter 8 discusses an experiment in which a system with isolated I-I spin pairs was allowed to evolve under the influence of the average Hamiltonian of Equation 45. This homonuclear dipolar oscillation was used to extract geometrical information in a polycrystalline solid, in an analogous manner to the heteronuclear dipolar oscillation experiments of Chapter 7.

REFERENCES

1. A. Pines, M. G. Gibby, and J. S. Waugh, J. Chem. Phys. 59, 569 (1973).

2. A. W. Overhauser, Phys Rev. 89, 689 (1953).

3. R. Freeman and W. A. Anderson, J. Chem. Phys. 37, 2053 (1962).

4. Wilhelm Magnus, Commun. Pure Appl. Math. 7, 649 (1954).

5. U. Haeberlen and J. S. Waugh, Phys. Rev. 175, 453 (1968).

6. W.-K. Rhim and D. D. Elleman, L. B. Schreiber and R. W. Vaughan, J. Chem. Phys. 60, 4595 (1974).

7. S. R. Hartmann and E. L. Hahn, Phys. Rev. 128, 2042 (1962).

8. M. E. Stoll, A. J. Vega, and R. W. Vaughan, J. Chem. Phys. 65, 4093 (1976).

9. W.-K. Rhim, D. D. Elleman, and R. W. Vaughan, J. Chem. Phys. 58, 1772 (1973).

10. R. K. Hester, J. L. Ackerman, V. R. Cross, and J. S. Waugh, Phys. Rev. Lett. 34, 993 (1975).

11. R. K. Hester, V. R. Cross, J. L. Ackerman, and J. S. Waugh, J. Chem. Phys. 63, 3606 (1975).

12. R. K. Hester, J. L. Ackerman, B. L. Neff, and J. S. Waugh, Phys. Rev. Lett. 36, 1081 (1976).

13. L. Müller, A. Kumar, T. Baumann, and R. R. Ernst, Phys. Rev. Lett. 32, 1402 (1974).

TABLE CAPTION

Table 1. Table of average Hamiltonians resulting from the application of various pulse cycles of Figure 1 to the I and S spins. The letters A, B, C, D, and E on the left refer to which cycle of Figure 1 is being applied to the spins. The frequency B in the average Hamiltonians is just the normal dipolar frequency.

Table 1

Sequence Applied to I Spins	Sequence Applied to S Spins	Average Hamiltonian
A	A	
B	B	
C	C	$\frac{1}{2}B(I_zS_z + I_yS_y)$
D	D	
E	E	
A	B	$\frac{1}{2}BI_zS_z$
B	C	
D	E	$\frac{1}{2}BI_yS_y$
B	E	
C	E	$\frac{1}{4}B(I_zS_z + I_yS_y)$
B	D	
C	D	$\frac{1}{4}BI_y(S_y - S_z)$
A	E	$\frac{1}{4}B(I_y + I_z)S_z$
A	C	
A	D	0

FIGURE CAPTIONS

Figure 1. Various pulse cycles to be applied to I and S spins, which do not suppress I-I interactions. The five cycles, A-E, are composed entirely of 90° pulses. The letters x and $\bar{x}$, etc., refer to the phase of the r.f. pulse, with the x and $\bar{x}$ indicating pulses 180° out of phase.

Figure 2. Various pulse cycles to be applied to I and S spins, which do suppress I-I interactions. The eight-pulse cycle, designated by I, is applied to the I spins while simultaneously one of the five cycles, S1-S5, is applied to the S spins. All pulses are 90°, and the x and $\bar{x}$, etc., refer to the phases of the r.f. pulses. The average Hamiltonians are also listed.

Figure 3. Fourier transform spectrum of ^{19}F dipolar oscillation due to the effects of ^{207}Pb in a single crystal of β-PbF_2. The ^{19}F-^{19}F interaction was suppressed by applying an eight-pulse cycle to the ^{19}F, and the ^{19}F-^{207}Pb interaction was maintained by applying no radiation to the ^{207}Pb. The center peak is due to ^{19}F near spinless ^{206}Pb and ^{208}Pb. The sidebands are due to the dipolar oscillation of the ^{19}F near ^{207}Pb.

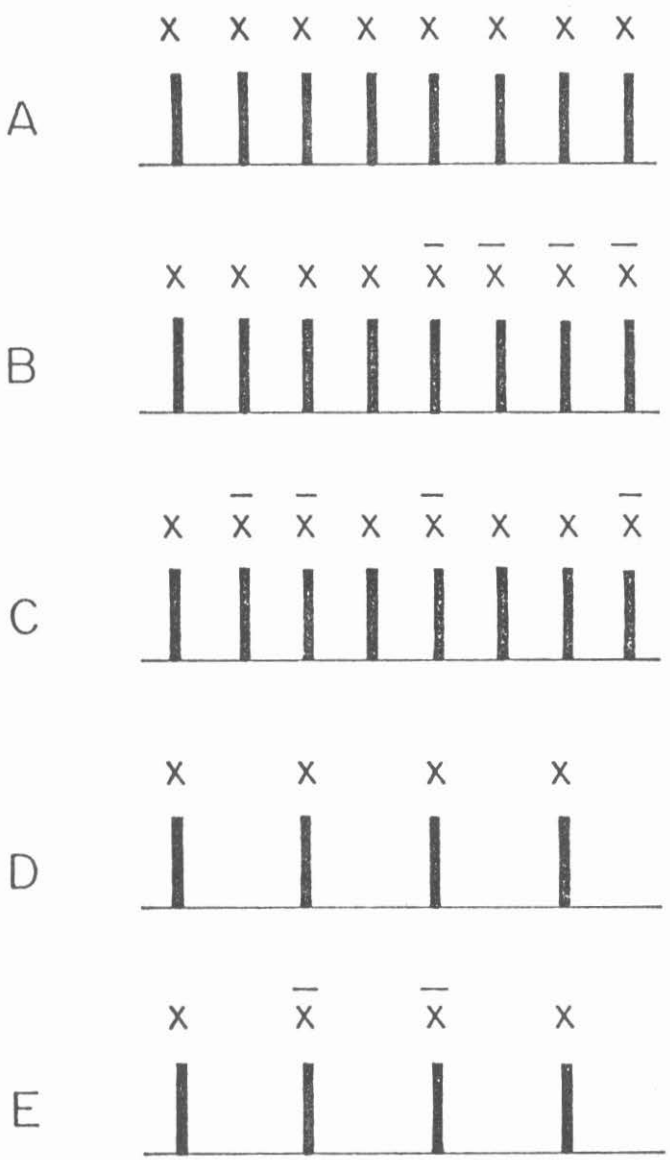

Fig. 1

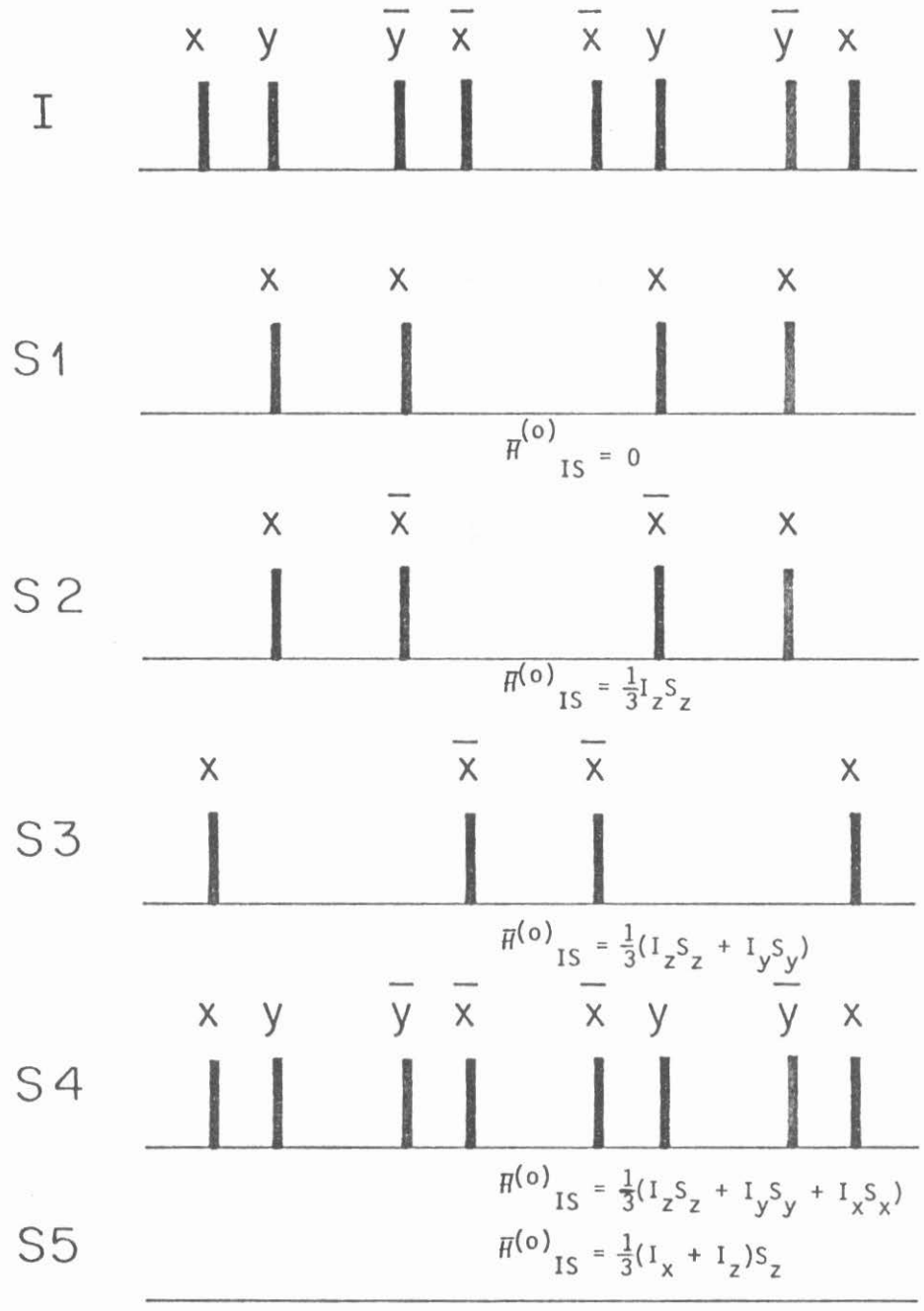
x y $\bar{y}$ $\bar{x}$ $\bar{x}$ y $\bar{y}$ x
I
x x x x
S1
$\bar{H}^{(o)}_{IS} = 0$
x $\bar{x}$ $\bar{x}$ x
S2
$\bar{H}^{(o)}_{IS} = \frac{1}{3} I_z S_z$
x $\bar{x}$ $\bar{x}$ x
S3
$\bar{H}^{(o)}_{IS} = \frac{1}{3}(I_z S_z + I_y S_y)$
x y $\bar{y}$ $\bar{x}$ $\bar{x}$ y $\bar{y}$ x
S4
$\bar{H}^{(o)}_{IS} = \frac{1}{3}(I_z S_z + I_y S_y + I_x S_x)$
S5
$\bar{H}^{(o)}_{IS} = \frac{1}{3}(I_x + I_z) S_z$

Fig. 2

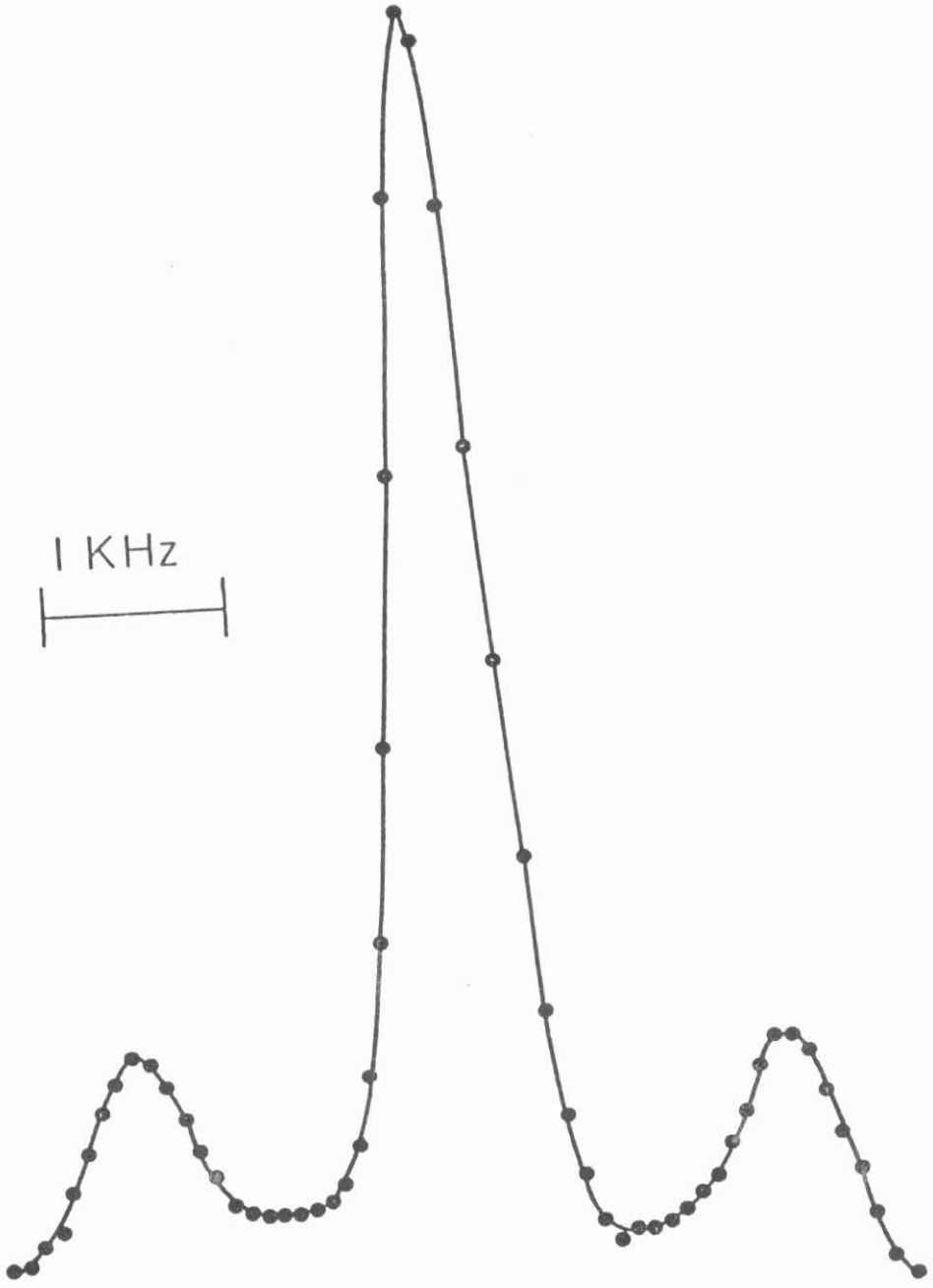

Fig. 3

CHAPTER 6

EXPERIMENTAL HETERONUCLEAR DIPOLAR SPIN DYNAMICS USING MULTIPLE PULSE DOUBLE RESONANCE

(Chapter 6 is essentially an article by M. E. Stoll, W.-K. Rhim, and R. W. Vaughan, entitled "Heteronuclear Spin Dynamics Using Multiple Pulse NMR Techniques". This article was published in the Journal of Chemical Physics, Vol. 64, No. 11, p. 4808, June 1, 1976.)

Polarization transfer between two spin systems, first demonstrated by Hartmann and Hahn (1), has been exploited recently (2) to enhance the signal-to-noise ratio in detection of rare spin species, and such polarization transfer can have an oscillatory character containing structural information (3). It has been recently demonstrated by Hester, et al (4) that detailed structural information can be extracted if the resolution of the dipolar spectrum is enhanced by suppressing the homonuclear dipolar interactions during the cross-polarization process.

It is the purpose of this Communication to demonstrate that heteronuclear polarization transfer can be induced and controlled under pulsed NMR conditions in contrast to the above measurement which used continuous irradiation. In particular, both a pulsed version of the original Hartmann-Hahn experiment is demonstrated, and a multiple pulse sequence is used to demonstrate simultaneous transfer of polarization and suppression of homonuclear dipolar interactions. The extension of the use of multiple pulse techniques into this domain furnishes an increased flexibility for design of double resonance experiments to furnish electronic, structural, and dynamical information. For example, the multiple pulse sequence used here has been the most effective means so far demonstrated (5) to suppress homonuclear dipolar interactions. The results in Figure 1 indicate the capability of pulsed techniques to induce heteronuclear polarization transfer both with (Fig. 1A and 1C) and without (Fig. 1B) suppression of homonuclear dipolar broadening. While extensive dipolar oscillations are not expected within βPbF_2 due to indirect Pb-F-Pb interactions, results of the suppression of homonuclear dipolar interactions are evident in these spectra.

For the decays illustrated in Figure 1A, an eight-pulse cycle (6) (t_{cycle} = 48 microseconds) was applied to the ^{19}F (I spins) while simultaneously applying a cycle of four 90^{o} pulses to the ^{207}Pb (S spins) within a βPbF_2 single crystal (7). This four-pulse cycle consisted of applying 90^{o}_{x} pulses coincident with each x pulse of the eight-pulse cycle, and 90^{o}_{-x} pulses coincident with the -x pulses (all orientational information (x,y,z) refers to directions in the appropriate rotating reference frame). The zeroth order average Hamiltonian for the I-S dipolar interaction in the interaction frame of the rf is covariant to that of Hartmann and Hahn (1) and is:

$$\overline{H}^{(0)}_{IS} = \sum_{im} \frac{\gamma_I \gamma_S \hbar^2}{3r_{im}^3} (1 - 3\cos^2\theta_{im}) (I_{z_i} S_{z_m} + I_{y_i} S_{y_m})$$

and thus one would expect only the x-spin polarization to be transferable from one spin system to the other.

In order to produce a graphic demonstration of the versatility available with these techniques, a phase alteration (6,8) was introduced into the x-pulse of the eight-pulse cycle to cause the I magnetization to precess in the x-z plane. The transverse components of the magnetization parallel to the x-axis in both I and S spin systems are observed at the end of successive cycles and illustrated in Figure 1A. As evidence of intimate and prolonged contact of the two spin species, the S spin polarization in the x-direction is observed to follow the component of the I spin polarization in the x-direction with a time lag of approximately 50 microseconds. (An analysis of this data is being used to furnish a precise characterization of the transfer process (9).) Note that while the oscillatory curve observed for the I spin

polarization is due to the precession of the magnetization, the oscillatory behavior observed for the S spin system is due to an actual change in magnitude of the S spin polarization.

Figures 1B and 1C allow one to compare the "sharpness" of the double resonance condition with and without suppression of the homonuclear dipolar coupling. In Figure 1B both spin systems were subjected to simultaneous 90^{o}_{x}-t-90^{o}_{x}-t-90^{o}_{x}-t-90^{o}_{x}-t pulse cycles (t = 8 microseconds), a pulsed analog of the original Hartmann-Hahn experiment. Polarization was initially produced along the x-direction in the I frame with a 90^{o}_{-y} prepulse, and the signal was observed in both spin systems (along x-axis) only at the end of successive cycles. For the cases in which the double resonance condition is matched, one observes that the magnitude of the S spin polarization rises rapidly and then decays slowly as the I spin temperature rises. The behavior of the S spin polarization under a variety of mismatch conditions is illustrated and demonstrates the "diffuseness" of the double resonance criteria in this pulse analog of the Hartmann-Hahn experiment (1). In Figure 1C the multiple pulse sequences described in the discussion of Figure 1A were used with a phase alteration in the 90^{o}_{y} pulses to produce an I spin locking field along the x-axis (6) and a pulse length alteration of the 90^{o}_{-x} (s-system) pulses to produce an equivalent effect for the S spin system. One notes that an order of magnitude smaller mismatch of the double resonance condition is needed in the dipolar suppressed case to interfere with polarization transfer. In fact, the matching condition in the dipolar suppressed case is critical enough to require substantial care that experimental problems such as rf field inhomogeneity do not interfere with the polarization transfer. (Therefore, a single coil probe was used here.)

It has been demonstrated that polarization transfer can be induced and controlled under multiple pulse conditions. Thus, the full capability of the multiple pulse techniques, to control separately the form of various parts of the spin-spin interaction Hamiltonian, can be exploited to devise and investigate a broadened class of double resonance experiments, both involving and not involving polarization transfer. We are presently investigating the nature, interrelationships, and potential utility of the wide variety of experiments made possible with this approach (9).

REFERENCES

1. S. R. Hartmann and E. L. Hahn, Phys. Rev. 128, 2042 (1962).

2. A. Pines, M. G. Gibby, and J. S. Waugh, J. Chem. Phys. 59, 569 (1973), and many references therein.

3. L. Muller, A. Kumar, T. Baumann, and R. R. Ernst, Phys. Rev. Letters 32, 1402 (1974).

4. R. K. Hester, J. L. Ackerman, V. R. Cross, and J. S. Waugh, Phys. Rev. Letters 34, 993 (1975); J. Chem. Phys. 63, 3606 (1975).

5. W.-K. Rhim, D. D. Elleman, and R. W. Vaughan, J. Chem. Phys. 59, 3740 (1973).

6. W.-K. Rhim, D. D. Elleman, L. B. Schreiber, and R. W. Vaughan, J. Chem. Phys. 60, 4595 (1974), and references therein.

7. The crystal was kindly furnished by Professor Irving Lowe, Department of Physics, University of Pittsburg.

8. C. R. Dybowski and R. W. Vaughan, Macromolecules 8, 50 (1975).

9. To be published.

FIGURE CAPTION

Figure 1.
Time development of polarization for both ^{19}F and ^{207}Pb in βPbF_2. The magnitude of the observed magnetization in the x-direction of the respective rotating frames is plotted on the ordinate, with one unit representing the room temperature thermal equilibrium polarization. In part A the ^{19}F polarization (○) is shown with the ^{207}Pb transferred polarization (△) with ^{19}F homonuclear dipolar couplings suppressed and the ^{19}F polarization forced to precess. In part B the results of performing the pulsed analog of the Hartmann-Hahn experiment are plotted with the various symbols representing ^{207}Pb polarization transferred with different degrees of mismatch of the double resonance condition: (○) - matched, (△) - 4.06 kHz mismatch, (□) - 9.62 kHz mismatch, and (◇) - 18.75 kHz mismatch. In part C the ^{207}Pb polarization transferred with homonuclear dipolar couplings suppressed is plotted for: (○) - matched and (△) - 1.67 kHz mismatched conditions.

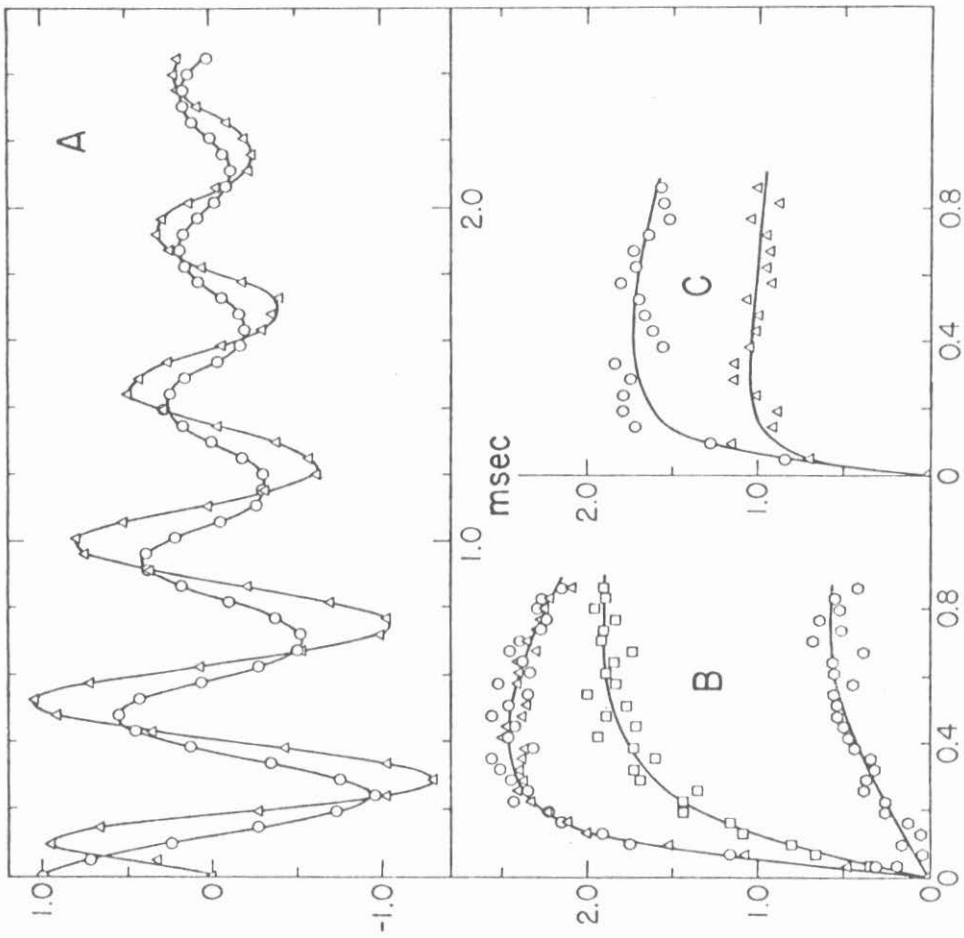

Fig. 1

CHAPTER 7

EXPERIMENTAL DETERMINATION OF STRUCTURAL INFORMATION IN POLYCRYSTALLINE SOLIDS USING HETERONUCLEAR DIPOLAR MODULATED CHEMICAL SHIFT SPECTRA

PART ONE

(Part One is essentially an article by M. E. Stoll, A. J. Vega, and R. W. Vaughan, entitled "Heteronuclear Dipolar Modulated Chemical Shift Spectra for Geometrical Information in Polycrystalline Solids". This article was published in the Journal of Chemical Physics, Vol. 65, No. 10, p. 4093, November 15, 1976.)

INTRODUCTION

Means of using the heteronuclear dipolar interaction between two spin ½ nuclei together with chemical shift information to furnish geometrical information have been widely discussed in the literature in the past year or two[1-4]. It is the purpose of this paper to present and demonstrate a scheme for combining multiple pulse NMR techniques[5,6] with dilute spin double resonance techniques[7] to furnish a particularly convenient scheme for determining local structural parameters near the dilute spin in solids including polycrystalline materials. The proposed scheme is an example of two-dimensional spectroscopy as recently discussed by Aue, et al.[8] and embodies concepts demonstrated by Hester, et al.[3,4] and discussed by Waugh[9] that one could obtain local structural information from the heteronuclear dipolar interaction by: (i) suppressing homonuclear dipolar couplings, and (ii) using the chemical shift tensor of a dilute spin species to orient the observed heteronuclear dipolar oscillations.

It was pointed out by Müller, et al.[1] that one could observe oscillations in the polarization transfer between two unlike spin ½ nuclei if a material were chosen in which the homonuclear dipolar interaction were reduced in size. VanderHart[2] has reported the use of initial cross-polarization rates, even in a case where the homonuclear dipole-dipole interaction is large, to orient the carbon chemical shift tensor in the molecular frame. Hester, et al.[3,4] have more recently reported that resolved heteronuclear dipolar polarization oscillations could be obtained by reducing homonuclear dipolar broadening with off-resonance irradiation at the magic angle, and Waugh[9] has discussed advantages of using the effective field heteronuclear dipolar interaction rather than polarization transfer heteronuclear dipolar interaction. Stoll, et al.[10]

demonstrated that multiple pulse techniques could be used to remove homonuclear dipolar broadening while simultaneously allowing polarization transfer between spin systems. The use of multiple pulse techniques is particularly attractive in this regard since they give the experimentalists control over the effective form of the various spin Hamiltonians, and thus give substantial flexibility for designing a variety of schemes to extract information from solid state NMR spectra. We have investigated, both theoretically and experimentally, a variety of such schemes and will present this information comprehensively in another paper[11].

The experimental scheme being presented here: (i) suppresses homonuclear dipolar interactions with multiple pulse techniques using an eight-pulse cycle[6]; (ii) allows the spin system to evolve under an effective Hamiltonian which has I_zS_z as the heteronuclear dipolar interaction and is, therefore, equivalent to the AX case of spin-spin coupling or J spectra; and (iii) refocuses the effects of chemical shifts and other static field inhomogeneities in the dilute spin system to allow separation of the time development due to dipolar oscillations. This latter step, in separating the time evolution due to the heteronuclear dipolar interaction from that produced by the spread in chemical shifts, makes the scheme particularly applicable to polycrystalline materials where otherwise the spread in the chemical shifts would prevent an accurate characterization of the dipolar frequencies.

While this manuscript was in the process of being refereed, two additional papers have been published which relate to the work reported here: J. S. Waugh[12] has discussed the use of the I_zS_z heteronuclear dipolar interaction, while Hester, et al.[13] have demonstrated a multiple pulse double resonance scheme for performing such experiments. This latter experiment[13] is

similar to the scheme proposed here but differs fundamentally in that no refocusing of the chemical shift effects in the dilute spin system is performed.

THE MULTIPLE PULSE DOUBLE RESONANCE TECHNIQUE

The multiple pulse double resonance scheme used here is illustrated in Figure 1 and can be separated into three sections. In the first, preparatory, period a transverse magnetization for the S (dilute) spin species is produced and any net magnetization in the I spin system is destroyed (the destruction of the I spin magnetization is not theoretically necessary but is an experimental precaution). The S spin transverse magnetization is created here by a Hartmann-Hahn[14] transfer of polarization from the I (abundant) spin system to make use of the signal-to-noise enhancement gained with this procedure, and the transverse magnetization in the I spin system is destroyed by turning off the I spin-locking field a millisecond or two before the initiation of the second, evolutionary, period.

In the second period an evolution of the I-S heteronuclear dipolar Hamiltonian is allowed to take place for a period, τ, while simultaneously suppressing the abundant spin dipole-dipole interaction with an eight-pulse sequence[6]. One notes that there are no rf fields on the S spin system during the period, τ, in which the eight-pulse sequence is being applied. Thus, since the total rf satisfies the cyclic and periodic conditions necessary for the application of the average Hamiltonian formulation[15], one can consider the zeroth order Hamiltonians present (all spin lattice effects are being ignored here as well as homonuclear dipolar interactions among the dilute (S) spins). For the I spin system, only a small chemical shift and off-resonance

Hamiltonian exists (besides the $\overline{H_{IS}^{(o)}}$) for a properly tuned cycle[6].

$$\overline{H_{oI}^{(o)}} = \sum_i \frac{\alpha(\Delta\omega + \omega_o \sigma_{zzi})}{3} (I_{xi} + I_{zi}) \qquad (1)$$

while the S spin system is evolving under the off-resonance and chemical shift Hamiltonian,

$$\overline{H_{oS}^{(o)}} = \sum_j (\Delta\omega + \omega_o \sigma_{zzj}) S_{zj} \qquad (2)$$

and the heteronuclear dipole-dipole interaction,

$$\overline{H_{IS}^{(o)}} = \sum_i \sum_j \frac{\alpha B_{ij}}{3} (I_{zi} + I_{xi}) S_{zj} \qquad (3)$$

where,

$$B_{ij} = \frac{\gamma_i \gamma_j \hbar}{r_{ij}^3} (1 - 3\cos^2\theta_{ij})$$

An important point for later interpretation is to note that these zeroth order Hamiltonians all commute, and thus the effective time evolution that occurs is simple to predict. Note also that the scaling factor[6], α, appearing in the $\overline{H_{IS}^{(o)}}$ term, is identical with that appearing in the off-resonance Hamiltonian in I spin system. This provides a convenient means of experimentally determining the numerical values for α by observing spectra of the I spin system as a function of the frequency offset, $\Delta\omega$.

After the desired amount of dipolar evolution, τ, has occurred, the eight-pulse sequence is replaced by a simple decoupling field on the I spin

system, and this causes the heteronuclear dipole-dipole interaction to go to zero. The S spin system is still evolving, however, under its off-resonance and chemical shift Hamiltonians. The next step within this evolutionary period is to refocus the time development of the off-resonance and chemical shift Hamiltonians in the S spin system by the application of a 180^{o} pulse to the S spin system, causing the production of a spin echo at a later time (the phase of the 180^{o} pulse was chosen parallel to the initial cross-polarizing field so that one gets an echo of the Carr-Purcell-Meilboom-Gill type).

The third period involves digitally recording the second half of the S system echo which provides the signal for further processing.

Thus, the total net time evolution of the S spin system that has occurred at the point where data collection is started, t=0, is due to the heteronuclear dipole-dipole interaction, Equation 3, for a time period τ. During the data collection period, t, however, only the off-resonance and chemical shift Hamiltonians are producing the time evolution of the S spin system. Thus, the data collected are easily interpreted since the heteronuclear dipolar information is in the initial amplitudes, and the chemical shift information is in the time evolution during the data collection time period, t. For the case of a single nearby I spin (applicable to both systems studied here), the S magnetization has the form:

$$\langle S_x \rangle \propto \sum_j (\cos \Omega_j \tau) \sin [(\sigma_{jzz} \omega_o + \Delta\omega) t] \tag{4}$$

$$\langle S_y \rangle \propto \sum_j (\cos \Omega_j \tau) \cos [(\sigma_{jzz} \omega_o + \Delta\omega) t] \tag{5}$$

$$\Omega_j = \frac{\alpha B_j}{3\sqrt{2}} \tag{6}$$

When the time decays of the magnetization are Fourier-transformed, one obtains powder patterns containing the heteronuclear dipolar evolution as a modulation. If the chemical shift powder patterns are assumed to be broadened by a Lorentzian broadening function and no broadening in the dipolar frequency spectrum is assumed, one obtains for a dipolar modulated spectrum:

$$f(\omega,\tau) = \int_0^{2\pi}\int_0^{\pi} \cos\,[\Omega(\theta,\phi)\tau]\,\{[\omega(\theta,\phi) - \omega]^2/w^2 + 1\}^{-1} \sin\theta\, d\theta\, d\phi \qquad (7)$$

where

$$\Omega(\theta,\phi) = \frac{\alpha\gamma_H\gamma_C}{3\sqrt{2}\, r^3}\,[1 - 3\,\{\sin\chi\,\sin\theta\,\cos(\phi - \psi) + \cos\chi\,\cos\theta\}^2] \qquad (8)$$

$$\omega(\theta,\phi) = \Delta\omega + \omega_o\,(\sigma_x\,\sin^2\theta\,\cos^2\phi + \sigma_y\,\sin^2\theta\,\sin^2\phi + \sigma_z\,\cos^2\theta) \qquad (9)$$

where $(\sigma_x, \sigma_y, \sigma_z)$ are the principal components of the S-chemical shift tensor, and (χ, ψ) designate the polar angles of the I-S vector with respect to the principal axis of the chemical shift tensor. Further, w is the half width of the chemical shift broadening function.

This expression was evaluated numerically by computer in order to generate the theoretical spectra discussed in the following sections of this paper. By collecting spectra for different values of the time, τ, of the dipolar evolution, detailed geometrical information can be obtained. This includes orientation of the I-S vector in the chemical shift principal axis system and a determination of the I-S vector length and, as is illustrated in some of the data presented here, information on the motion of the I-S vector in the laboratory frame.

This particular scheme has a number of advantages. Since no rf irradiation is on the S spins during the dipolar evolution, there is no rf matching condition which must be met and for which a mismatch could cause distortions[10] (in fact, one should generalize the Hartmann-Hahn matching condition for pulsed measurements such as these to the simple statement, $\overline{H_{IS}^{(o)}} \neq 0$).

Since the only remaining possible rf errors are those in the proton radiation, these can be removed, or calibrated out, separately by observing the proton magnetization. (In fact, small errors in the proton irradiation will not distort the S spin spectra to any appreciable extent[6,11]. Finally, the form of an interaction Hamiltonian, $\overline{H_{IS}^{(o)}}$, which commutes with both the I and S Hamiltonians simplifies the interpretation of the data obtained and allows a very simple extension to systems involving additional simultaneous I-S interactions or such complexities as the presence of molecular motion. For example, since the Hamiltonians commute, additional I spins near the S spin result in the observation of dipolar frequencies which are simply sum and difference frequencies of the individual I-S interactions.

EXPERIMENTAL DETAILS

The apparatus used is the one designed for the pulsed polarization transfer experiments previously published[10]. It consists of a low frequency multiple pulse spectrometer[16] which has been altered by replacing the original probe with a single-coil probe which is simultaneously tuned for both protons (56.4 MHz) and carbon (14.18 MHz), and by the addition of rf electronics at the carbon frequency (a James Millan amplifier capable of 150 watts at 14.18 MHz and a wideband Avantek receiver). This single-coil probe design made it possible to have good H_1 homogeneity (< 0.5%) and large H_1 field for both carbon and proton frequencies (40-50 gauss) with relatively low power rf transmitters.

Cross-polarization fields of 8.1 gauss on the protons and 33 gauss on the carbons were used, while a decoupling field of 20 gauss was applied to the protons. The proton-decoupling field was larger than necessary for decoupling

but was maintained at this high level to avoid matching the Hartmann-Hahn condition[14] during the 180° pulse applied to form the carbon-13 echo. The multiple pulse sequence used is the eight-pulse sequence discussed in detail elsewhere[6], and it was carefully tuned as described to keep error Hamiltonians[6] smaller than 200 Hz. The frequency-scaling factor, α (a number close to unity), was determined by observing a proton line as a function of frequency offset, $\Delta\omega$. Since the dipolar frequencies encountered are large (over 20 kilohertz) care was taken to measure the small nonlinear dependence of the scaling factor, α, on the size of the off-resonance field. A 5% effect in 10 kilohertz, and this was incorporated into the spectra synthesis program as a calibration factor.

Only absorption spectra are reported in the paper to conserve space; however, the dispersion spectra were available, and they did confirm the information obtained. A few comments on the procedure used to assure that phase and amplitude information would be comparable from spectrum to spectrum would appear to be in order, however. First, the 180° carbon pulse was set at a fixed delay (greater than the longest τ value desired) from the end of the carbon cross-polarization pulse, and it remained fixed throughout the experiment. Then the precise point to begin digitization ($t = 0$) was determined by summing several adamantane[17] decays taken at different offset frequencies (with $\tau = 0$) and adjusting the digitization point until no linear phase shift appeared in the spectrum. The phase was then set to observe the absorption spectrum and not changed throughout the experiment. Samples enriched in ^{13}C were used in this work, 15% for the benzene (one site/molecule @ 90%) and around 6% for the calcium formate.

A cross-polarization time of 12 milliseconds was used on the benzene,

but it was not possible to completely remove the distortion in the spectra caused by benzene rings oriented at the magic angle, and this slight distortion is observable in the experimental spectra. In all cases, a cycle time of 50 microseconds was used for the eight-pulse cycle, and the proton frequency was on resonance.

RESULTS AND DISCUSSION

a. Benzene

In order to experimentally test the concepts and techniques suggested above, experimental spectra were taken on a benzene sample where the proton serves as the abundant species and carbon-13 as the rare species.

Figure 2 illustrates the results expected theoretically from applying the pulsing sequence described above to a benzene sample in its rotator phase, that is, in the temperature range where the molecule is spinning rapidly around its sixfold symmetry axis. The results are a function of two independent variables and form a surface in a three-dimensional space. In Figure 2 two projections of three-dimensional plots are shown for the integration of Equation 7 for benzene in its rotator phase. This is a convenient frame of reference since single experiments (i.e., the collection of data as a function of t for a fixed τ and Fourier transformed) produce sets of data points in the f-ω plane corresponding to that value of τ. The spectrum for $\tau = 0$ is thus the normal C^{13} chemical shift powder pattern for benzene.

In this case of a benzene molecule spinning rapidly around its sixfold symmetry axis, both the dipolar and chemical shift tensors exhibit axial symmetry around the rotation axis, and the only parameters needed to specify

the full surface in Figure 1 are: the chemical shift components, $\sigma_{\perp}$ and $\sigma_{\parallel}$, the carbon-proton distance, r (1.09 Å), the chemical shift scaling factor, α[6], and experimental broadening functions. In order to be able to compare this theoretical plot with our experiments, a broadening function for the chemical shift axis was taken from a computer fit to a normal ^{13}C powder pattern, and we assumed that only the nearest C-H dipolar interaction need be considered. The chemical shift scaling factor, α, was determined experimentally as described above from the proton multiple pulse spectra. Thus, the surface plotted in Figure 2 is fully determined. While the surface is complex, for the special case of benzene simple oscillations are observed if one takes planes in the f, τ plane for fixed ω since the dipolar and chemical shift tensors have the same symmetry axis and map isomorphically onto one another. Experimental data were taken over the full range of τ considered in Figure 2 (600 microseconds), and the first half is shown in Figure 3 along with an expanded version of the bottom projection from Figure 2. The experimental three-dimensional plot in the top half of Figure 3 was obtained by simply connecting all data points with straight lines to their neighbors, and thus each intersection of two lines is a data point, and the ripple noted in the surface is a measure of the experimental scatter in the data. One notes that there is good quantitative agreement with the predicted spectra for the structural features appearing in the experimental data. A quantitative comparison can also be made by comparing the calculated and experimental data as plotted in Figure 4. In Figure 4 the spectra (Fourier transforms of the time decays) for the various experimental values of τ are plotted beside the predicted spectra for the same τ. Care has been

taken to be sure that the relative magnitudes of each of the experimental spectra have been reproduced quantitatively. Amplitude comparisons can be made between the corresponding experimental and theoretical spectra (i.e., the theoretical spectra have been normalized to the experimental at only the τ = 0 spectra, and all other amplitudes are as predicted or as measured). Thus, one obtains good quantitative agreement as well as qualitative agreement over the range of τ considered in Figure 3 (0-250 microseconds). The only lack of agreement occurs in the portion of the spectra near $\omega = \sigma_{||}$, where a reduction in amplitude is noted which gets progressively worse as τ gets larger until in the bottom spectra the last oscillation in the far right of the theoretical spectra is almost completely absent in the experimental spectra. If one compares the regions corresponding to ($\omega = \sigma_{||}$) in the projections of Figure 3, one notes that this corresponds to the reduced amplitude of the depression closest to the observer in the experimental 3-D plot, by comparison with the theoretical 3-D plot. One notes that this corresponds to the region of the highest dipolar frequencies and might be expected to suffer from our assumption of a single C-H dipolar frequency before other portions of the spectra.

This kind of quantitative comparison begins to fail at longer τ values, and the amplitude of the oscillation in both wings of the spectra begins to decay below the predicted values until at τ = 600 microseconds only the center third of the spectrum remains, as is indicated in Figure 5. The observed frequency of oscillations in this remaining center portion corresponds accurately to what is predicted but the amplitude has decayed to approximately half of what is predicted. It is to be noted that it is that portion of the spectra containing the smaller dipolar oscillations that has lasted the

longest, and there appears experimentally to be a broadening function on the dipolar frequencies proportional to their magnitude. The cause for this degradation at long times is presently under study, and it is not yet clear whether it will be attributable to secondary C-H dipolar interactions, low-frequency motion in the solid benzene at this temperature (-90^{o} C) or due to some broadening mechanism involving so-far-neglected interactions.

It is clear, however, that an excellent agreement is obtained for shorter decay times and that this technique furnishes a potentially useful and accurate method for extracting geometrical information in polycrystalline solids.

b. Calcium Formate

Experimental and theoretical results were also obtained for calcium formate since it represents a more complicated situation than that found in benzene. There is still only a single carbon-proton vector to deal with, but one does not see the unique situation in benzene where the dipolar and chemical shift tensors have the same symmetry. However, the room temperature results obtained illustrate another potential use for these techniques in the study of molecular motion and its characterization.

Ackerman, et al.[18] have reported values for the carbon-13 chemical shift tensors in calcium formate and found that there are two slightly inequivalent tensors. The polycrystalline powder patterns we obtained at room temperature were not compatible, however, with the reported results, ours giving a pattern 20% too narrow. This pattern was well fit with the powder pattern for a single tensor with the following principal values: $\sigma_{11} = -92$, $\sigma_{22} = -59$, $\sigma_{33} = +18$, which give an anisotropy roughly twenty percent smaller than reported by Ackerman, et al.[18]: $\sigma_{11a} = -106$,

$\sigma_{11b} = -105$, $\sigma_{22a} = -61$, $\sigma_{22b} = -57$, $\sigma_{33a} = \sigma_{33b} = 24$ ppm. Since the center of mass of the patterns reported here was similar to that of Ackerman, et al.[18], one could speculate that our echo spectra are exhibiting the effects of motional averaging of the chemical shift tensor at room temperature. Powder patterns were taken as the temperature was lowered to the minimum presently possible in our probe, -170^{o} C; while the powder pattern grew broader, it did not reach the reported values of Ackerman, et al.[18].

To observe what effect such molecular motion might have, theoretical spectra were calculated by using the fitted values of the chemical shift tensor and a broadening function from the conventional powder pattern ($\tau = 0$) and assuming a single dipolar frequency corresponding to a C-H distance of 1.12 Å. The lower portion of Figure 6 is a projection of the three-dimensional plot of one such calculation in which the least-shielded tensor component was assumed to be parallel to the C-H vector. The projection in the top portion of Figure 6 is the experimental data taken at room temperature, and one sees rather large qualitative differences between the two projections. These differences are illustrated in Figure 7, where the theoretical and experimental spectra for the same value of τ are compared. We did a large number of simulations varying the orientation of the C-H vector and its length, attempting to fit the experimental pattern and could not do better than the spectra shown in Figure 7. In fact, one can make a simple argument to show that it will not be possible to fit this spectra with any realistic assumptions, so long as one ignores the molecular motion present. We have already assumed an unrealistically long C-H vector in the spectra calculated,

1.12 Å, and no matter which direction we point the C-H vector, it will invert a portion of the powder pattern by the first observation point (τ = 50 microseconds). Since our experimental spectra have substantially larger area than the predicted spectra, they will not fit. Thus, one can, by using only the top two experimental spectra (τ = 0 and τ = 50 microseconds) from Figure 6, conclude that substantial molecular motion is present.

Presently we are in the process of building into our theoretical synthesis program means to model such molecular motion and hope to be able to fit a series of spectra such as shown in Figure 7 to characterize the molecular motion present.

SUMMARY AND CONCLUSIONS

A double resonance, multiple pulse scheme has been proposed, and has been demonstrated, that will allow the extraction of geometrical, orientational, and motional information from polycrystalline chemical shift powder patterns. The particular scheme developed embodies concepts recently discussed by Hester, et al.[3,4] and has been designed and developed to solve a number of problems: it allows increased signal to noise by first providing an initial cross-polarization period; it does not involve dipolar evolution with polarization transfer since such schemes as we can devise are sensitive to small errors and mismatch condition of the rf fields; it provides for a separate means of calibrating the chemical shift scaling factor; and it produces spectra in which the dipolar modulation appears in a particularly simple form for data analysis, and the requirements for rf fields on the S spin are the minimal required for normal cross-polarization powder pattern experiments. As discussed

in the Introduction, while this manuscript has being refereed two papers appeared in print[12,13] which relate to the work reported here, and in particular, the single crystal, double Fourier transform experiment described by Hester, et al.[13] has many of the advantages of the scheme reported here, although no attempt is made in that work[13] to refocus the chemical shift effects.

The results reported here clearly indicate that the experimental scheme proposed for observing dipolar modulated chemical shift spectra can produce results in agreement with theoretical expectations. The rather drastic changes that occur in the spectra even for short times of dipolar evolution, τ, make it possible to orient C-H vectors in the chemical shift frame accurately from polycrystalline powder samples and, even in cases where single crystals can be obtained, will provide an attractive alternative to the laborious collection of rotation spectra. Since the dipolar modulated chemical shift spectra orient the I-S bond vectors in the chemical shift principal axis frame in contrast to single crystal rotation studies which orient the chemical shift tensor in the crystalline unit cell, two types of measurements can be used to supplement one another when detailed crystal structures are not available.

This particular scheme should find particularly fruitful application in areas of solid state chemistry where systems without long-range order (surface adsorbed species and polymers, for example) require characterization of geometrical and electronic properties.

REFERENCES

1. L. Müller, A. Kumar, T. Baumann, and R. R. Ernst, Phys. Rev. Lett. 32, 1402 (1974).
2. D. L. VanderHart, J. Chem. Phys. 64, 830 (1976).
3. R. K. Hester, J. L. Ackerman, V. R. Cross, and J. S. Waugh, Phys. Rev. Lett. 34, 993 (1975).
4. R. K. Hester, V. R. Cross, J. L. Ackerman, and J. S. Waugh, J. Chem. Phys. 63, 3606 (1975).
5. J. S. Waugh, L. M. Huber, and U. Haeberlen, Phys. Rev. Lett. 20, 180 (1968).
6. W-K. Rhim, D. D. Elleman, L. B. Schreiber, and R. W. Vaughan, J. Chem. Phys. 60, 4595 (1974) and references therein.
7. A. Pines, M. G. Gibby, and J. S. Waugh, J. Chem. Phys. 59, 569 (1973) and many references therein.
8. W. P. Aue, E. Bartholdi, and R. R. Ernst, J. Chem. Phys. 64, 2229 (1976).
9. J. S. Waugh, private communication of work presented at the Second Specialized Colloque Ampere, Budapest, Hungary, August, 1975 (unpublished).
10. M. E. Stoll, W-K. Rhim, and R. W. Vaughan, J. Chem. Phys., 64, 4808 (1976).
11. M. E. Stoll, A. J. Vega, W-K. Rhim, and R. W. Vaughan, in preparation.
12. J. S. Waugh, Proc. Natl. Acad. Sci. 73, 1394 (1976).
13. R. K. Hester, J. L. Ackerman, B. L. Neff, and J.S. Waugh, Phys. Rev. Lett. 36, 1081 (1976).
14. S. R. Hartmann and E. L. Hahn, Phys. Rev. 128, 2042 (1962).

15. J. S. Waugh, C. H. Wang, L. M. Huber, and R. L. Vold, J. Chem. Phys. 48, 662 (1968); U. Haeberlen and J. S. Waugh, Phys. Rev. 175, 453 (1968).

16. R. W. Vaughan, D. D. Elleman, L. M. Stacey, W-K. Rhim, and J. W. Lee, Rev. Sci. Instr. 43, 1356 (1972).

17. A slightly ^{13}C enriched sample of adamantane was kindly provided by Professor A. Pines of the University of California at Berkeley.

18. J. L. Ackerman, J. Tegenfeldt, and J. S. Waugh, J. Am. Chem. Soc. 96, 6843 (1974).

FIGURE CAPTIONS

Figure 1. Schematic representation of the pulsing scheme used.

Figure 2. Theoretical dipolar modulated ^{13}C chemical shift spectra for benzene undergoing rapid rotation around its six-fold axis. The spectra were calculated by numerical integration of Equation 7. The height, or value, along the f axis corresponds to the intensity expected for a given value of the length of the dipolar evolution period, τ, at a particular resonance frequency, ω, in the adsorption spectrum. The surface is viewed from an angle of 45^{o} away from the f axis and at -45^{o} (top projection) and $+45^{o}$ (bottom projection) from the τ axis. The lines of constant τ are at 50 microsecond intervals, while the lines of constant ω are at intervals of 3.45 ppm (corresponding to an experimental sampling rate of 50 KHz).

Figure 3. Theoretical and experimental (-90^{o} C) spectra for benzene undergoing rapid rotation around its six-fold axis. Nomenclature is the same as in Figure 2, but results are only shown for τ out to 300 microseconds. The top spectra are a plot of the experimental data obtained by making straight-line connections between each data point and its nearest neighbor in both τ and ω. Thus, each intersection is the location of a single experimental data point. The theoretical calculation was done for the same points on the surface f (ω, τ) for which data were available so a direct point-by-point comparison could be made.

Figure 4. Sections through the surface f (ω, τ) for planes of constant τ for both theoretical (left portion of figure) and experimental spectra

(right portion of figure) of benzene rotating rapidly around its six-fold axis. The values of τ (in microseconds) corresponding to each spectra are: A,0; B,50; C,100; D,150; E,200; and F,250. The experimental and theoretical spectra were normalized at $\tau = 0$ only, and quantitative comparisons can be made of the theoretical vs. experimental amplitudes in the remaining spectra. The horizontal scale is 3.45 ppm/point.

Figure 5. The experimental spectra for benzene obtained with τ = 600 microseconds. The abscissa covers the same total range as the spectra in Figure 4 and each point is 3.45 ppm.

Figure 6. Theoretical and experimental spectra for dipolar modulated ^{13}C chemical shift of calcium formate. The lower spectrum represents the result of numerically integrating Equation 7, while the upper stereographic projection is a plot of the experimental results produced by making straight-line connections between each data point and its nearest neighbor in both τ and ω. The scales are the same as in Figures 2 and 3 (50 microseconds between lines of constant τ, and 3.45 ppm between lines of constant ω).

Figure 7. Sections through the surface $f(\omega, \tau)$ on planes of constant τ for both theoretical (left portion of figure) and experimental spectra (right portion of figure) for the calcium formate results in Figure 6. The values of τ (in microseconds) corresponding to each spectra are: A,0; B,50; C,100; D,150; E,200; and F,250. The abscissa scale is 3.45 ppm/point.

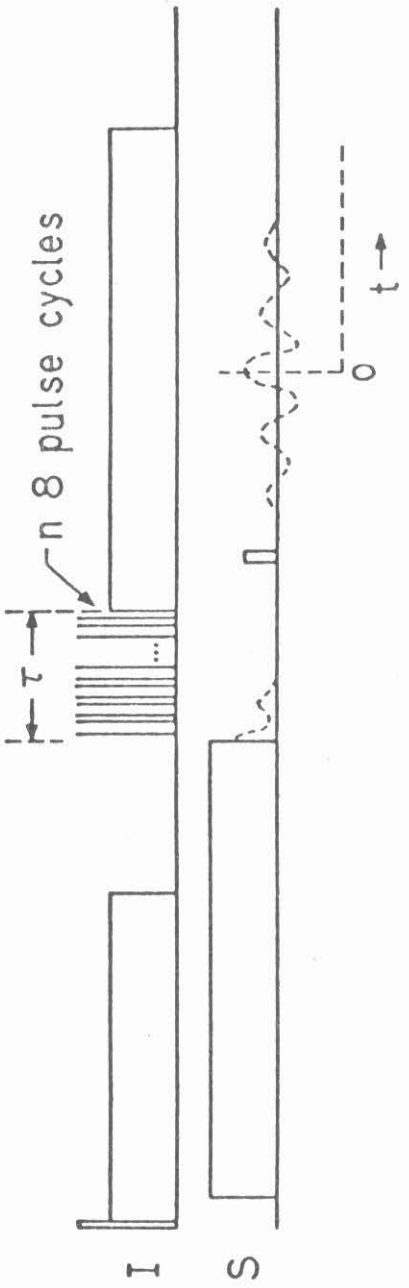

Fig. 1

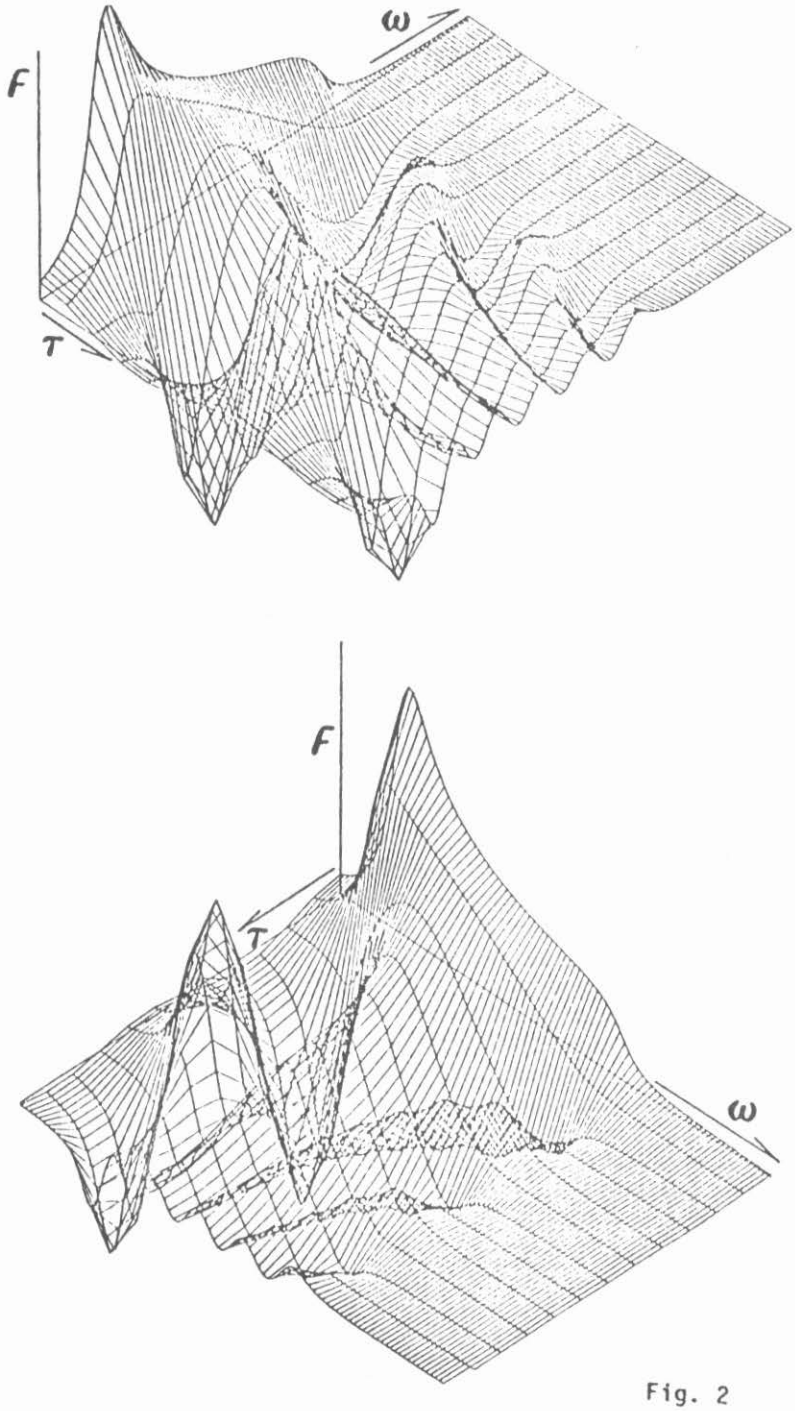

Fig. 2

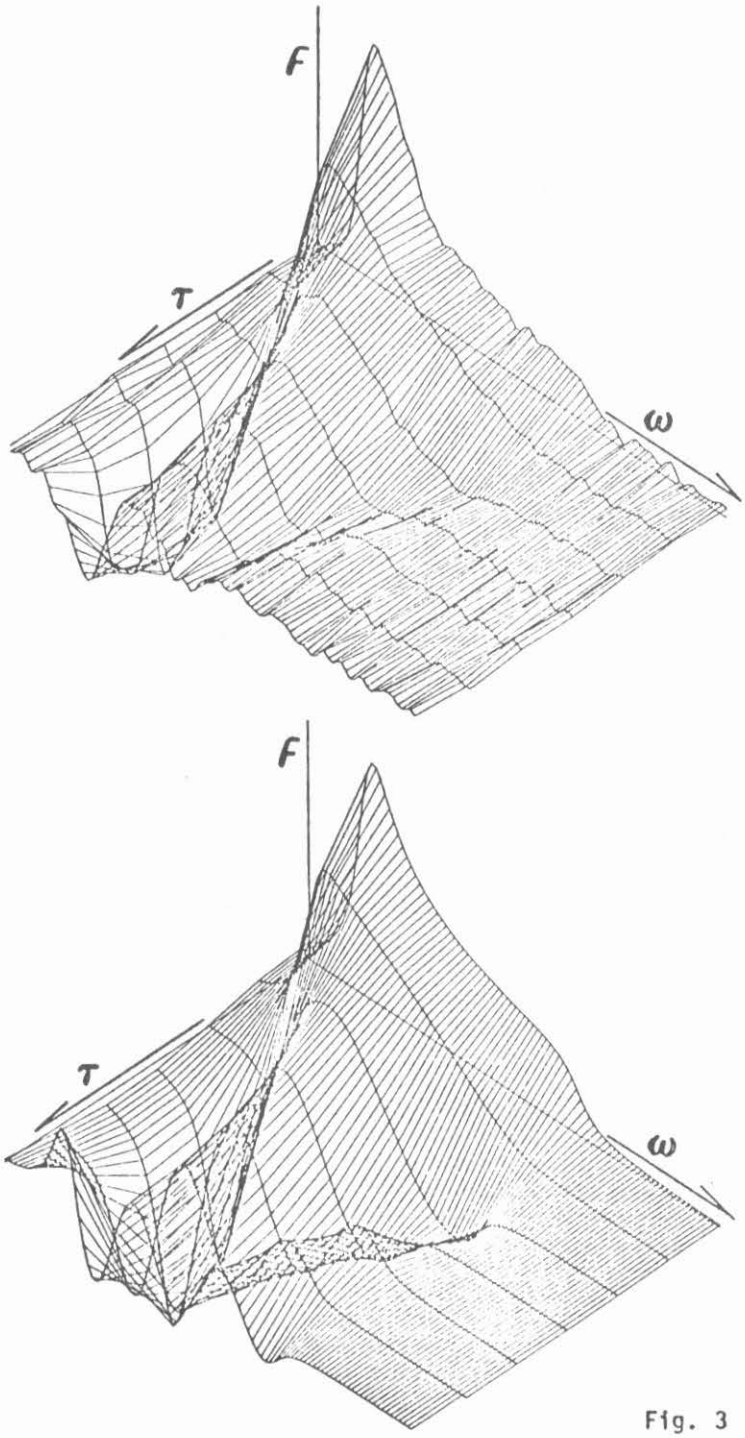

Fig. 3

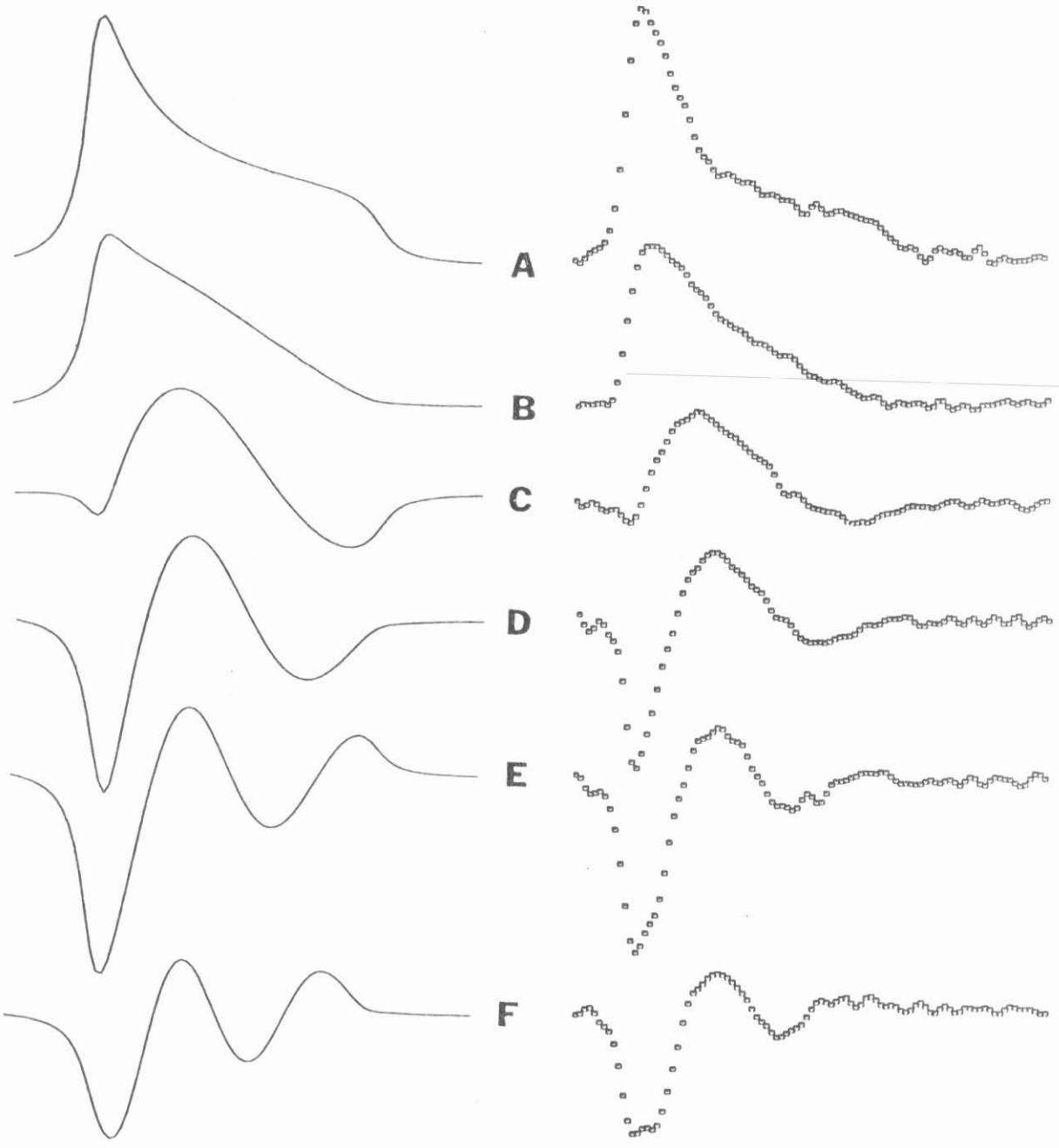

Fig. 4

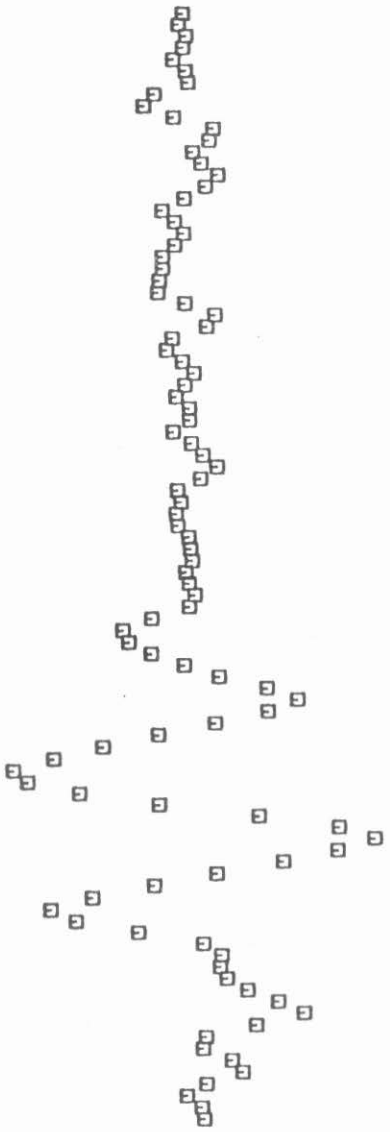

Fig. 5

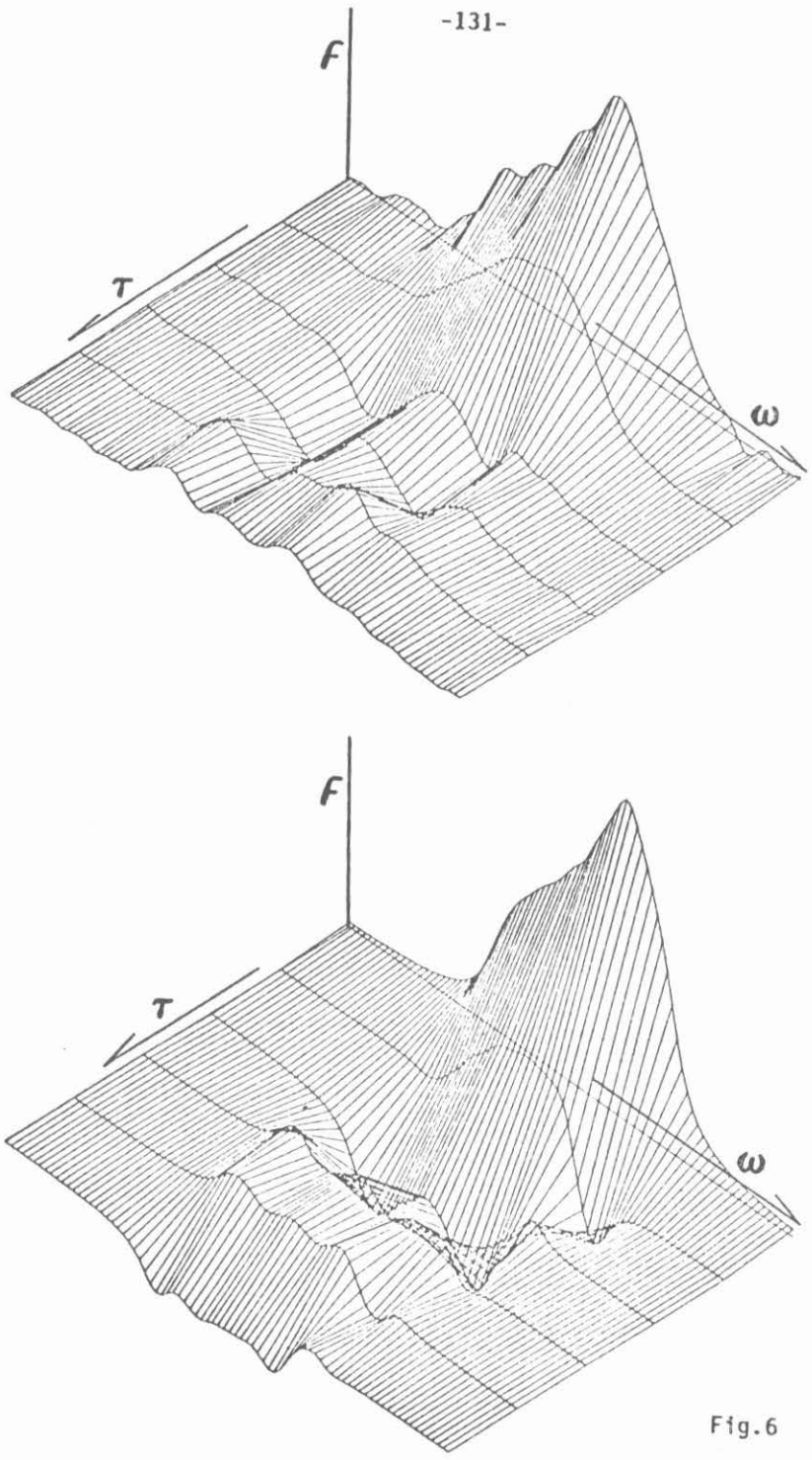

Fig.6

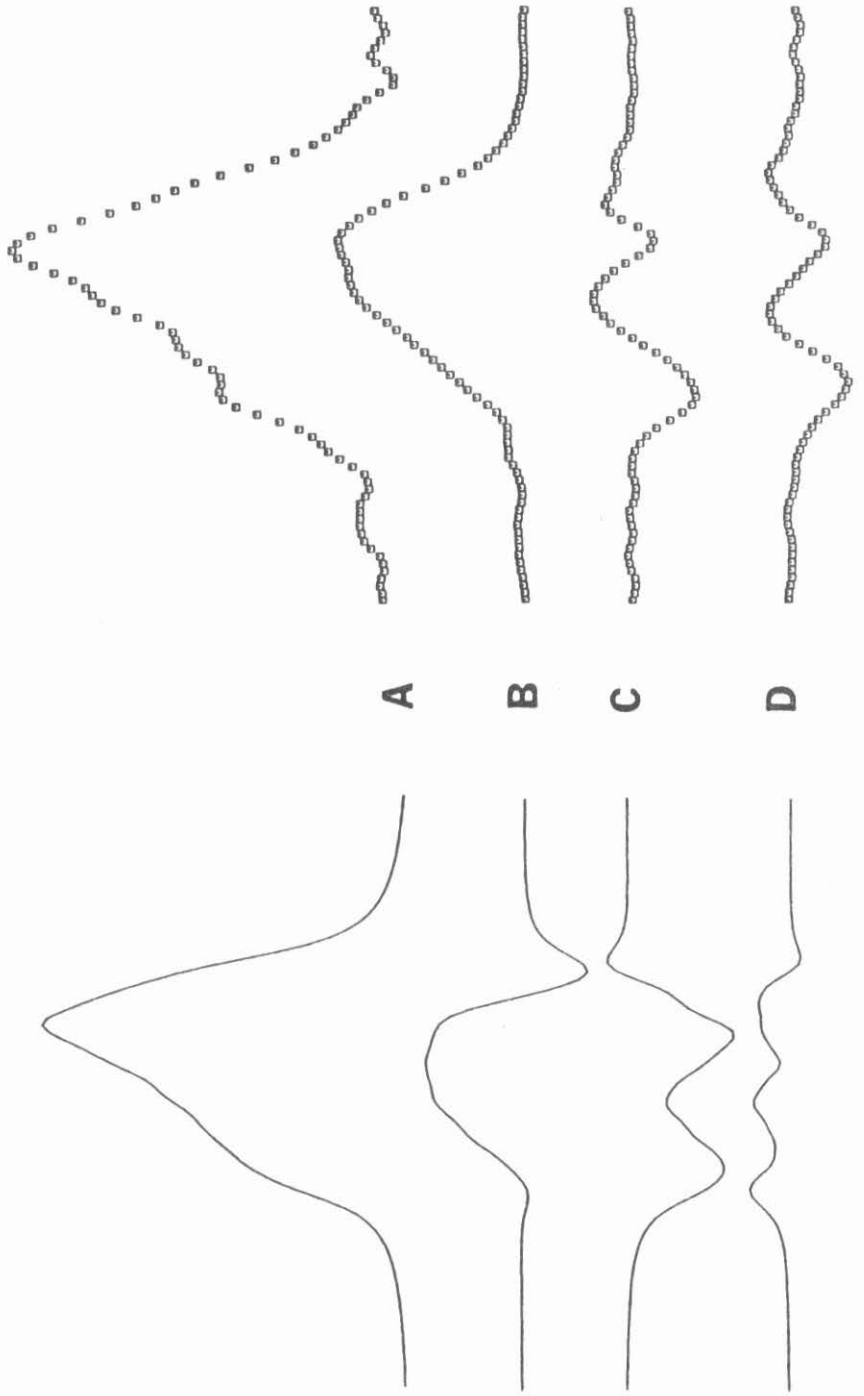

Fig. 7

PART TWO

(The material in Part Two represents a continuation and update of the work in Part One. This material is drawn from an article by M. E. Stoll, A. J. Vega, and R. W. Vaughan, entitled "Structural Information in Polycrystalline Systems Via Dipolar Modulated Chemical Shift Spectra". This article was published in the Proceedings of the XIXth Congress Ampere, p. 429, Heidelberg, 1976.)

I. INTRODUCTION

In Part Two of Chapter 7, we present the results of a continuation of the work of Part One. The nature of this additional work is largely theoretical, meaning that we have attempted to improve our understanding of the data taken in Part One, and no new experiments were performed. Although the results of the benzene studies in Part One are encouraging, the agreement between theory and experiment still is not totally satisfying. So in this section we consider the effects of a system with one S spin and more than one I spin, with the goal of getting better experimental and theoretical agreement. Since we were using benzene enriched to 90% at a single site, it is a good approximation that we have only one S(^{13}C) spin in our system. There are a total of six I(^{1}H) spins in a ring, however, and the inclusion of the effects of all six changes the theoretical spectra substantially from those of Part One, which include only the effects of the nearest neighbor I spin. These new calculated spectra agree both qualitatively and quantitatively with experimental results of Part One. It is crucial that we have confidence in the validity of the heteronuclear dipolar modulation technique, because we can then speak with more authority in the case of the calcium formate which does not exhibit good agreement at all between theory and experiment.

A second important aspect of the dipolar modulated chemical shift spectra is explored. By merely determining the areas of the series of spectra with different periods of modulation time, τ, one can determine the I - S bond distance, although one then loses all orientational information.

We present theoretical and experimental comparisons of the areas of such modulated spectra in benzene and calcium formate.

II. Effects of Six Protons on ^{13}C Dipolar Modulated Spectra in Benzene

Since we are using the experimental results of Part One of this chapter, we refer the reader to that section for the details of the experiment. Equation 3 of Part One shows that the I - S average Hamiltonian during the period of dipolar evolution, τ, is of the form $I_z S_z$. We know from the discussion of Chapter 5 that such a Hamiltonian causes linear oscillation of the magnetization. This is reflected in Equations 4, 5 and 6 of Part One, which show the S magnetization to be linear oscillating with a modified dipolar frequency. We now take into account that there are in fact six I spins in the benzene, and not just one. In order to do this we refer to the theoretical discussion of Chapter 5. We recall that Equation 35 of Chapter 5 showed that the effect on the S magnetization of more than one I spin was to cause it to oscillate as a product of cosines, each I spin contributing one cosine factor. Thus rather than exhibiting a single dipolar frequency, the S magnetization oscillates with sums and differences of all the various I - S dipolar frequencies. We can then include these effects by modifying Equations 4, 5 and 6 of Part One to read

$$\langle S_x \rangle \propto \sum_j \prod_{i=1}^{6} \cos(\Omega_{ji}\tau)\sin\left((\sigma_{jzz}\omega_o + \Delta\omega)t\right) \qquad (1)$$

$$\langle S_y \rangle \propto \sum_j \prod_{i=1}^{6} \cos(\Omega_{ji}\tau)\cos\left((\sigma_{jzz}\omega_o + \Delta\omega)t\right) \tag{2}$$

$$\Omega_j = \frac{\alpha B_{ji}}{3\sqrt{2}} \tag{3}$$

where the subscript j refers to the S spins, and the subscript i, running over the values 1 through 6, refers to the six I spins on the same benzene ring.

Figure 1 shows a comparison of the experimental data with the results of theoretical calculations based on Equation 1, 2 and 3 of Part Two and Equations 7, 8 and 9 of Part One, for heteronuclear dipolar modulated chemical shift spectra of benzene in its rotor phase near -90°C. The agreement is both qualitative and quantitative. Figure 4 of Part One shows a comparison of experiment and theory, taking only the nearest I spin into account. Note that for τ = 250 μsec, Figure 4F, there is already substantial discrepancy. However, for the case of all six I spins considered, Figure 1 of this section shows good agreement for times as long as τ = 500 sec. These theoretical plots were based on the accepted value of 1.09Å for the C–H bond length, as well as other accepted geometrical constants for the benzene ring. The plots were made with just two adjustable parameters, the ultimate linewidth (the parameter w of Equation 7 of Part One) for various isochromats summed to get the powder pattern, and the normalization of the spectra. These two parameters were fixed by the spectra for τ = 0, and there are no adjustable parameters for the theoretical spectra for τ>0. We feel that these results confirm the validity of the heteronuclear dipolar modulation technique.

Figure 2 shows a comparison of theoretical dipolar modulated chemical shift spectra for benzene with only one I spin included (left side) and with all six I spins included (right side). The top and bottom are just different views of the same spectra. These plots are similar to the ones found in Part One of this chapter. Note that the effect of the extra I spins is to "wash out" some of the detail of the spectra by making the valleys and troughs not as deep and the peaks and ridges not as high. In general the details are not as pronounced. This can be understood as the many sum and difference dipolar frequencies begin to destructively interfere for longer values of τ, thus leading to the greatest discrepancies in the two spectra for the longest values of τ.

III. Areas of Heteronuclear Dipolar Modulated Spectra

It is a well-known fact that the area of a Fourier transform (FT) frequency spectra is proportional to the size of the corresponding time signal at t = 0. Thus we can see from Equations 1, 2 and 3 that the area, A, for our spectrum should be

$$A(\tau) \propto \sum_{j} \prod_{i=1}^{6} \cos(\Omega_{ji}\tau) \tag{4}$$

By normalizing our areas to the area for $\tau = 0$, and by assuming an isotropic distribution of crystals in our sample, we get

$$\frac{A(\tau)}{A(o)} = \frac{1}{4\pi} \int \prod_{i=j}^{6} \cos(\Omega_i \tau) \sin\theta d\theta d\phi \tag{5}$$

where the i refers to the various I spins, and the j has been dropped because it is now implicit in the sum over all solid angles. The $\sin\theta d\theta d\phi$ is just the usual differential element of solid angle.

Figure 3A shows experimental and theoretical comparison of this area ratio in benzene as a function of τ. The solid line is the area ratio from Equation 5 taking all six protons into account, while the dashed line is the theoretical area ratio including the effects of only the nearest proton. The experimental points seem to fit the six-proton theory very well. Note that for values of τ greater than 500 μsec, we expect no net area. This does not mean that we cannot see a spectrum anymore, but it does mean that the spectrum will have equal amounts of positive and negative area.

By examining Equation 5, we see that observation of the area ratio yields no orientational information because it is all integrated out. However, the answer still depends strongly on the internuclear C–H distance. The theoretical plots in Figure 3A used a C–H bond length of 1.09Å. If one does not have isotropically distributed crystals, then one measures the appropriately weighted average

$$< \frac{1}{r^3}(1 - 3\cos^2\theta) > \qquad (6)$$

So actually, even in our isotropic case we really measured the average

$$< \frac{1}{r^3} > \qquad (7)$$

Thus we actually determine a measure of the bond length by finding the quantity in Equation 7 from the area ratio. This quantity may be very sen-

sitive to thermal expansion and could conceivably be used to study changes in bond length as a function of temperature.

Figure 3B shows the theoretical and experimental area ratios for calcium formate. The solid line corresponds to the accepted value of the bond length, r, of 1.09Å, while the dashed line is for r = 1.19Å. Neither of these curves fits well. In fact, one can show that there is no value for r which will fit well. We can rule out the effects of other I spins as a source of this enigma by noting that in Figure 3A the result of several I spins is to cause the area ratio to damp out much more quickly as a function of τ. But Figure 3B shows that the experimental area ratio for τ = 250 μsec is still quite large, thus indicating that there is little destructive interference and hence only one important I spin. (Note: we have plotted the benzene and calcium formate data with τ scales differing by a factor of two. We did this because the spinning benzene rings reduce the dipolar interaction by a factor of two.)

IV. Conclusion

From the close agreement between theory and experiment of the benzene dipolar modulated spectra and their area ratios, we conclude that the dipolar modulation technique is sound and can be used as a tool to measure bond angles and bond distances in polycrystalline solids. Our total failure in calculating the calcium formate spectra and area ratios, even including effects of other I spins, seems to indicate that the suspicions we raised in Part One of this chapter are correct. We assume that there is some molecular motion

causing major changes in the dipolar modulated spectra. We hope that further work on this anomaly will prove that these techniques can be very useful in the determination of molecular motions in solids.

Figure Captions

Figure 1. Experimental (left) and theoretical (right) heteronuclear dipolar modulated chemical shift spectra in benzene, taking all six protons into account. The spectra are for values of the dipolar modulation time, τ, of 0, 100, 200, 300, 400 and 500 sec from top to bottom. Each channel in the experimental plots is 3.45 ppm for the horizontal scale.

Figure 2. Calculated dipolar modulated chemical shift spectra comparing one-proton theory (left) with six-proton theory (right). The top and bottom represent two different views of the same spectra. Each figure incorporates spectra with values of τ from 0 to 600 μsec at 50 μsec intervals. These pseudo 3-dimensional plots are similar to those in Figures 2, 3 and 6 of Part One of Chapter 7.

Figure 3. Theoretical and experimental area ratios of dipolar modulated chemical shift spectra as a function of τ, in (A) benzene and (B) calcium formate. (A) The solid line is the six-proton theory and the dashed line is the one-proton theory. (B) The solid line is for the C–H bond length, $r = 1.09\text{Å}$. The dashed line is for $r = 1.19\text{Å}$. Both these curves are for a one-proton theory.

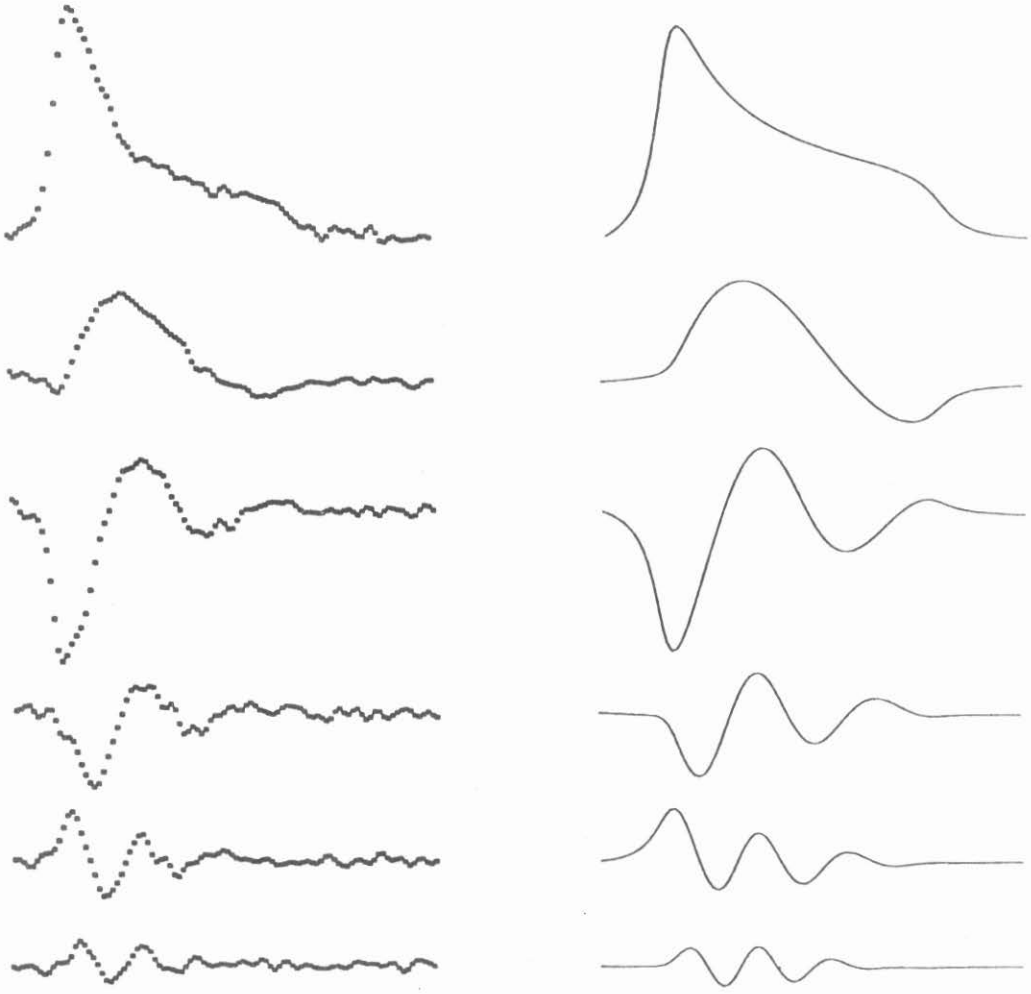

Fig. 1

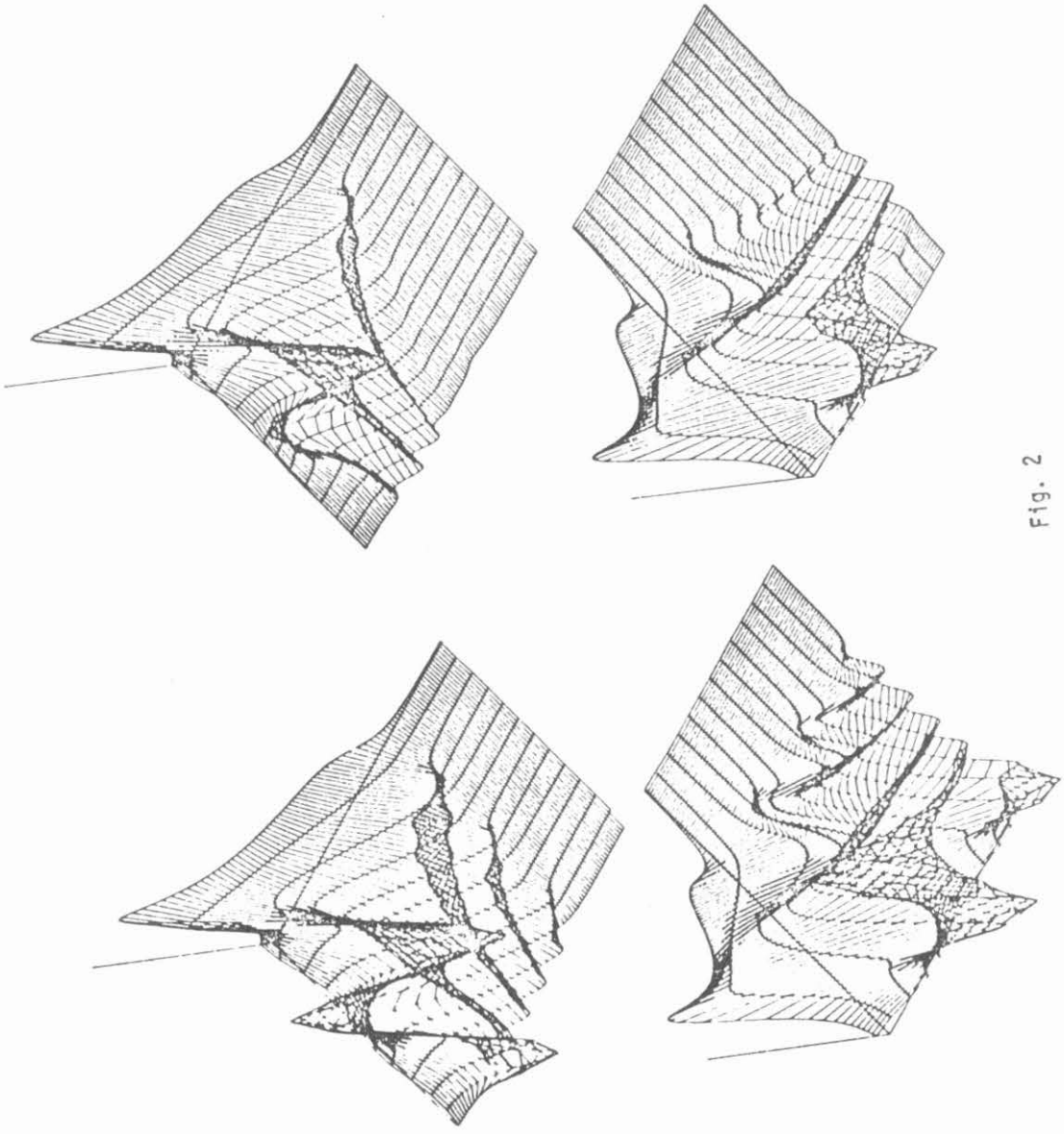

Fig. 2

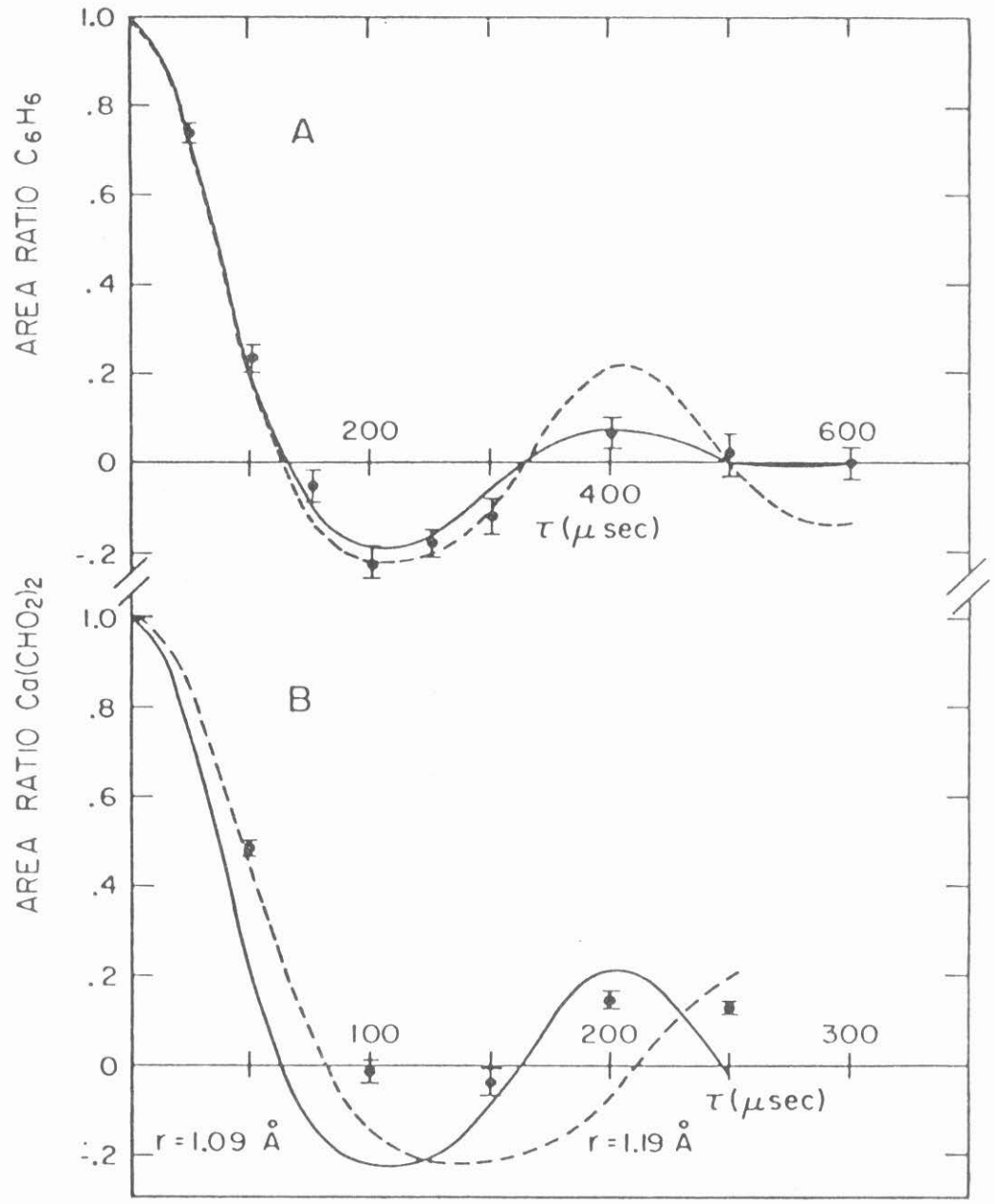
AREA RATIO C_6H_6
1.0
.8
.6
.4
.2
0
-.2
A
200
400
600
τ (μ sec)
AREA RATIO $Co(CHO_2)_2$
1.0
.8
.6
.4
.2
0
-.2
B
100
200
300
τ (μsec)
r = 1.09 Å
r = 1.19 Å

Fig. 3

CHAPTER 8

EXPERIMENTAL DETERMINATION OF STRUCTURAL INFORMATION IN A POLYCRYSTALLINE SOLID USING HOMONUCLEAR DIPOLAR MODULATED CHEMICAL SHIFT SPECTRA

(Some of the material in Chapter 8 is drawn from an article by M. E. Stoll, A. J. Vega, and R. W. Vaughan, entitled "Structural Information in Polycrystalline Systems Via Dipolar Modulated Chemical Shift Spectra". This article was published in the proceedings of the XIXth Congress Ampere, p. 429, Heidelberg, 1976. The rest of the material in Chapter 8 is taken from an article being prepared for publication.)

I. Introduction

In this chapter we present the results of a homonuclear dipolar modulated chemical shift experiment which determines geometrical parameters of trichloroacetic acid (TCAA) from a polycrystalline sample. This experiment is the homonuclear analogue of the heteronuclear dipolar modulated chemical shift experiment of Chapter 7, and thus the motivation is also analogous. We would like to have a method for determining structural parameters without the necessity of having a single crystal sample and accumulating many rotation spectra. To achieve this goal we make use of the orientationally dependent dipolar interaction to modulate the conventional high resolution chemical shift powder pattern. By computer simulations of the spectra for various parameters, we are able to determine a proton-proton bond length and its orientation with respect to the principal axis chemical shift reference frame. Unlike the experiments of Chapters 6 and 7, we do not suppress any dipolar interactions during the modulation period. We instead rely on the natural crystal structure to provide us with the necessary dipolar structure to see long-lived dipolar oscillations. This is similar to the work of Müeller, et al. [1], in which transient oscillations in $^{1}H-^{13}C$ cross polarization experiments in ferrocene were seen only because of the high degree of natural fine structure in the dipolar spectrum.

The spin dynamics of the relevent average Hamiltonian was discussed in Chapter 5, in the section dealing with the homonuclear dipolar Hamiltonian. To aid in the understanding of the details of our experiment, we shall refer the reader to that section.

II. Experimental

Trichloroacetic acid (CCl_3COOH) is known to dimerize in the solid state. This leads to ^1H (proton) pairs which are well isolated, and Goldman first reported seeing well-resolved dipolar split doublets in the proton NMR spectra of single crystals of TCAA [2]. The high degree of isolation of the I - I pairs ensures that the normal polycrystalline proton NMR powder pattern will be rich in detail also. Figure 1 shows a Fourier transform (FT) spectrum we obtained from a normal free-induction decay (FID) of a powdered sample of TCAA. The spectrum is a classic doublet, axially symmetric tensor powder pattern [3], and the crispness of outer shoulders indicates the high degree of isolation of the proton pairs.

In Figure 2 we show a diagram of the relevant part of the TCAA solid structure. The ring formed by the two carboxyl groups is flat to within .01Å. Hydrogen bonding between the two carboxyl groups is responsible for the dimerization. These hydrogen bonds are shown schematically by dotted lines. The splitting between the peaks in a spectrum like that of Figure 1 is

$$\Delta\nu = \frac{1}{2\pi}\frac{3}{2}\frac{\gamma_I^2 \hbar}{r^3} \qquad (1)$$

where $\Delta\nu$ is the splitting (in H_z), γ_I is the proton magnetogyric ratio, and r is the proton-proton distance. From Equation 1 and Figure 1 we conclude that r = 2.56 ± .04Å, in agreement with the literature [3]. So from the standard FT spectrum we can already determine the I - I separation, and in

order to be useful, our homonuclear dipolar modulation experiment must give us additional information.

In Figure 3 we show schematically the r.f. pulse sequence applied during the dipolar modulation experiment. First, a transverse proton magnetization is created by the application of a 90° pulse. A period of time, τ, follows in which nothing is done to the I spins. During this dipolar evolution period, the I - I pairs are strongly coupled by the dipole-dipole Hamiltonian. At time t = 0, we apply a standard eight-pulse cycle [4] which uses the techniques of coherent averaging [5] to remove the I - I dipolar interaction. By viewing the magnetization stroboscopically at the frequency of the eight-pulse cycle, we are able to acquire a signal which we Fourier transform to yield a solid state high resolution chemical shift powder pattern. We then collect these FT spectra for various values of τ. Figure 4 shows just such a series of spectra. The number on the spectra are the values of τ in units of 4.17 μsec, so the last spectrum has had a dipolar evolution time of almost 300 μsec. The eight-pulse cycle time was 50 μsec.

During the period τ, the total average Hamiltonian that is acting on each proton pair is

$$\bar{H}^{(0)} = B(3I_{1_z}I_{2_z} - \underset{\sim}{I}_1 \cdot \underset{\sim}{I}_2) + \Delta\omega_1 I_{z_1} + \Delta\omega_2 I_{z_2}$$

$$B = \frac{1}{2}\frac{\gamma_I^2}{r^3}(1 - 3\cos^2\beta) \qquad (2)$$

where factors of $\hbar$ are ignored, $\underset{\sim}{I}_1$ and $\underset{\sim}{I}_2$ are the dimensionless spin angular momentum operators for the two protons; β is the angle between the proton-

proton vector, $\underset{\sim}{r}$, and the z-axis, and $\Delta\omega_1$ and $\Delta\omega_2$ are the off-resonance frequencies. We note that the off-resonance terms commute with the dipolar term. This is crucial because it means that the developments due to each can be separated. Although we did not do so, one could, in principle, refocus the effects of the off-resonance Hamiltonian with a short 180° pulse placed at ½ τ. This could be very important if the chemical shift anisotropy were large and the inherent signal-to-noise were small, because without refocussing, only a fraction of the proton magnetization remains a time t = 0. Since neither of these was a problem for us, we did not use such a spin echo. Linear phase effects in our spectra resulting from the off-resonance Hamiltonian not being refocussed were calibrated and compensated for, by empirically measuring the proper phase corrections in proton H_2O spectra taken off-resonance by various amounts, for each value of τ. Thus we can confine our attention to only the dipolar term

$$\bar{H}_{II}^{(0)} = B(3I_{1_z}I_{2_z} - \underset{\sim}{I}_1 \cdot \underset{\sim}{I}_2) \qquad (3)$$

according to Equation 45 of Chapter 5.

Equation 48 of Chapter 5 shows that this Hamiltonian leads to linear oscillation of the magnetization at the frequency 3 B/2. As in Chapter 7, we synthesize a theoretical powder pattern by numerically summing the pattern from a series of Lorentzian broadened isochromats, representing an isotropic distribution of crystals. The equation for the actual theoretical spectrum is

$$f(\omega, \tau) = \int_0^{2\pi} \int_0^{\pi} \cos\,(\Omega(\theta, \phi)\tau) \qquad (4)$$

$$\times \{\left(\omega(\theta, \phi) - \omega\right)^2/w^2 + 1\}^{-1} \sin\,\theta d\theta d\phi$$

where we have

$$\Omega(\theta, \phi) = \frac{3}{2} \frac{\gamma_I^2}{r^3} \qquad (5)$$

$$\times \{1 - 3(\sin\,\chi\,\sin\,\theta\,\cos\,(\phi - \psi) + \cos\,\chi\,\cos\,\theta)^2\}$$

and also

$$\omega(\theta, \phi) = \{\Delta\omega + \omega_0(\sigma_x \sin^2\theta\,\cos^2\phi + \sigma_y\,\sin^2\theta\,\sin^2\phi + \sigma_z \cos^2\theta)\}\,\frac{\sqrt{2}}{3}\,\alpha \qquad (6)$$

where α is the empirically determined off-resonance scaling factor of the eight-pulse cycle [6], $\Delta\omega$ is the off-resonance frequency, ω_0 is the Larmor frequency of the protons, $(\sigma_x, \sigma_y, \sigma_z)$ are the principal components of the proton chemical shift tensor, (χ, ψ) are the polar angles of the I - I vector with respect to the chemical shift frame, and (θ, ϕ) are the polar angles of external magnetic field, also in the chemical shift frame. The parameter w, in Equation 4, is the half-width of the Lorentzian broadening function.

From symmetry we know that the chemical shift tensors of the two protons (see Figure 1) are identical and that these protons have the same local

environment. Thus we have identical spectra from each of the two I spins.

III. Results and Discussion

Using Equations 4, 5 and 6, we have synthesized theoretical spectra for comparison with experimental spectra. Figure 5 shows such a comparison for spectra corresponding to value of τ = 1, 7 and 10 units of 4.17 μsec. The agreement is quite close, and all spectra used the values for the parameters of Equation 4, 5 and 6 of $\chi = 76° \pm 1°$, $\psi = 22° \pm 5°$, and $(\sigma_x, \sigma_y, \sigma_z)$ = (-21.8, -18.2, -.9) ppm. with respect to TMS.

We feel that these results confirm the validity of the homonuclear dipolar modulated chemical shift technique. By using it we have determined the orientation in the chemical shift frame of a proton-proton vector in a polycrystalline material. This type of experiment could prove very useful in certain metallic hydrides or in other samples which have a small group of isolated spins.

Using the dipolar modulated experiments, we can determine, from a powder, some information about the relationships of the molecular frame and the chemical shift frame, i.e., internuclear vector angles and lengths. Single crystal rotation experiments can provide information about relationship of the crystallographic frame to the molecular frame, however the presence of more than one site can lead to ambiguities. By using the two techniques in tandem, one should be able to resolve some of those ambiguities.

References

1. L. Müeller, A. Kumar, T. Baumann, and R. R. Ernst, Phys. Rev. Lett. 32, 1402 (1974).
2. M. Goldman , J. Phys. Chem. Solids, 7, 165 (1958).
3. A. Abragam, "The Principles of Nuclear Magnetism", Oxford University Press, London, 1961, pp. 220, 221.
4. W.-K. Rhim, D. D. Elleman, and R. W. Vaughan, J. Chem. Phys. 58, 1772 (1973).
5. J. S. Waugh, L. M. Huber, and U. Haeberlen, Phys. Rev. Lett. 20, 180 (1968).
6. W.-K. Rhim and D. D. Elleman, L. B. Schreiber and R. W. Vaughan, J. Chem. Phys. 60, 4595 (1974).

Figure Captions

Figure 1. Fourier transform of proton free-induction decay in polycrystalline trichloroacetic acid. Each horizontal channel represents 488 H_z.

Figure 2. Diagram of carboxyl groups of dimerized TCAA. The hydrogen bonds are represented by dashed lines. The distances shown are in Å.

Figure 3. Schematic diagram of r.f. pulse sequence used. A 90° prepulse is given and followed by the period of dipolar evolution, τ. From time t = 0, the eight pulse cycle is applied to the protons to remove the homonuclear dipolar interaction.

Figure 4. Homonuclear dipolar modulated proton chemical shift spectra in polycrystalline TCAA. The numbers indicate the length of dipolar evolution time, τ, in units of 4.17 μsec. The spectra on the right have been vertically magnified for convenience. On the horizontal axis, each channel represents .71 ppm. The proton resonance was at 56.4 M Hz.

Figure 5. Experimental (points) and theoretical (solid) TCAA comparison of homonuclear dipolar modulated chemical shift spectra. The numbers represent values for τ in units of 4.17 μsec. On the horizontal axis, each channel is .71 ppm. Spectra for τ = 7 and τ = 10 have been vertically magnified by factors of 2 and 5, respectively.

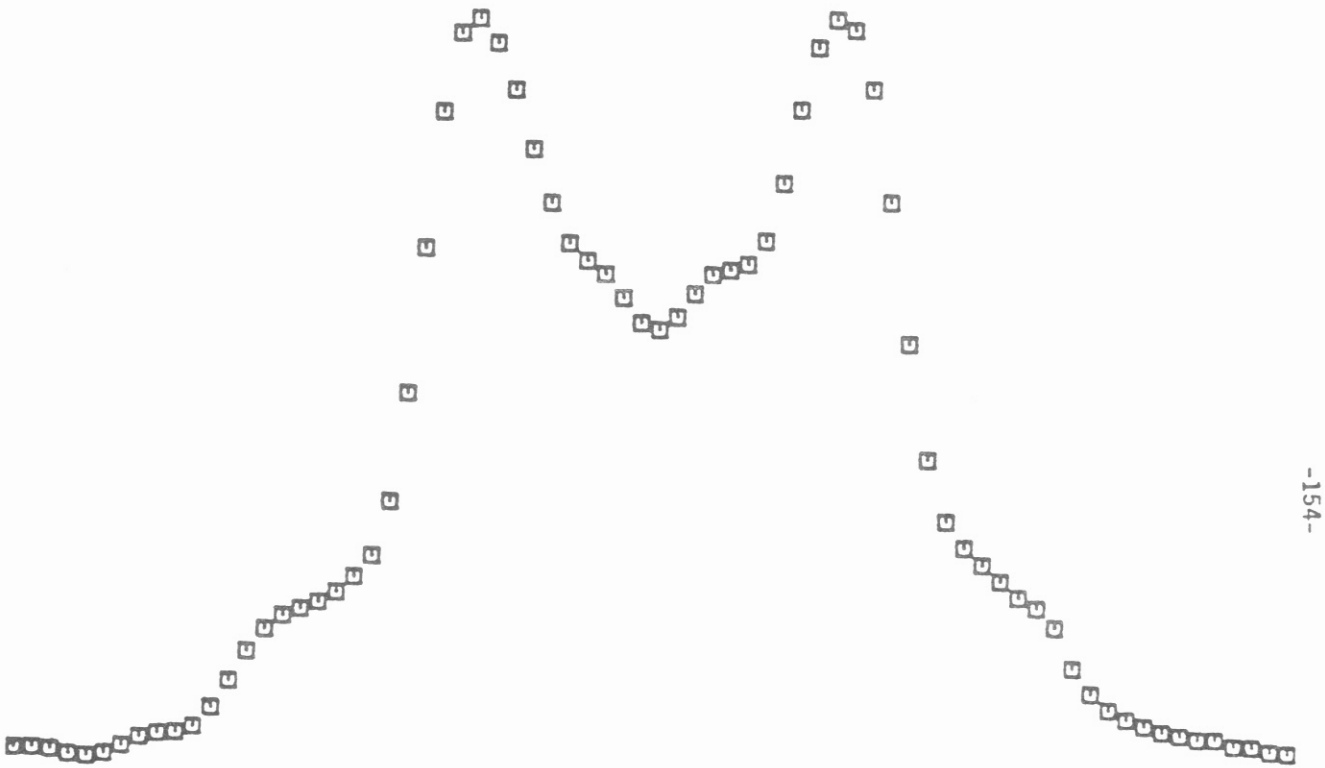

TCAA FID

Fig. 1

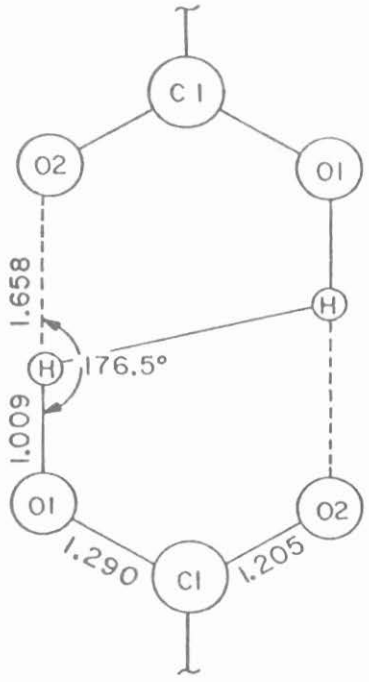

Fig. 2

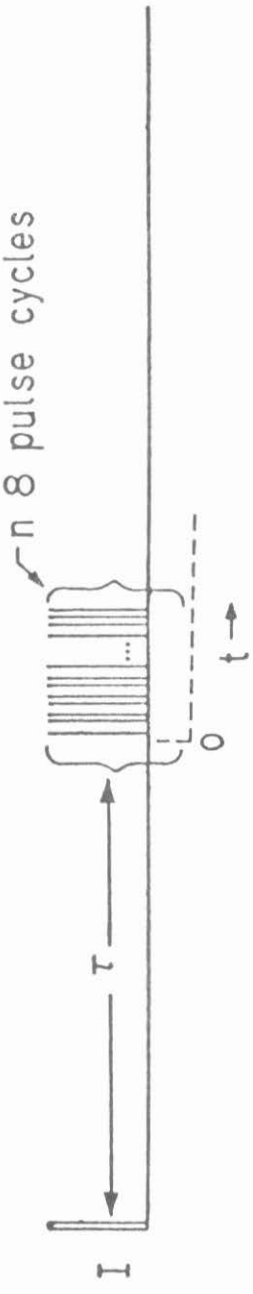

Fig. 3

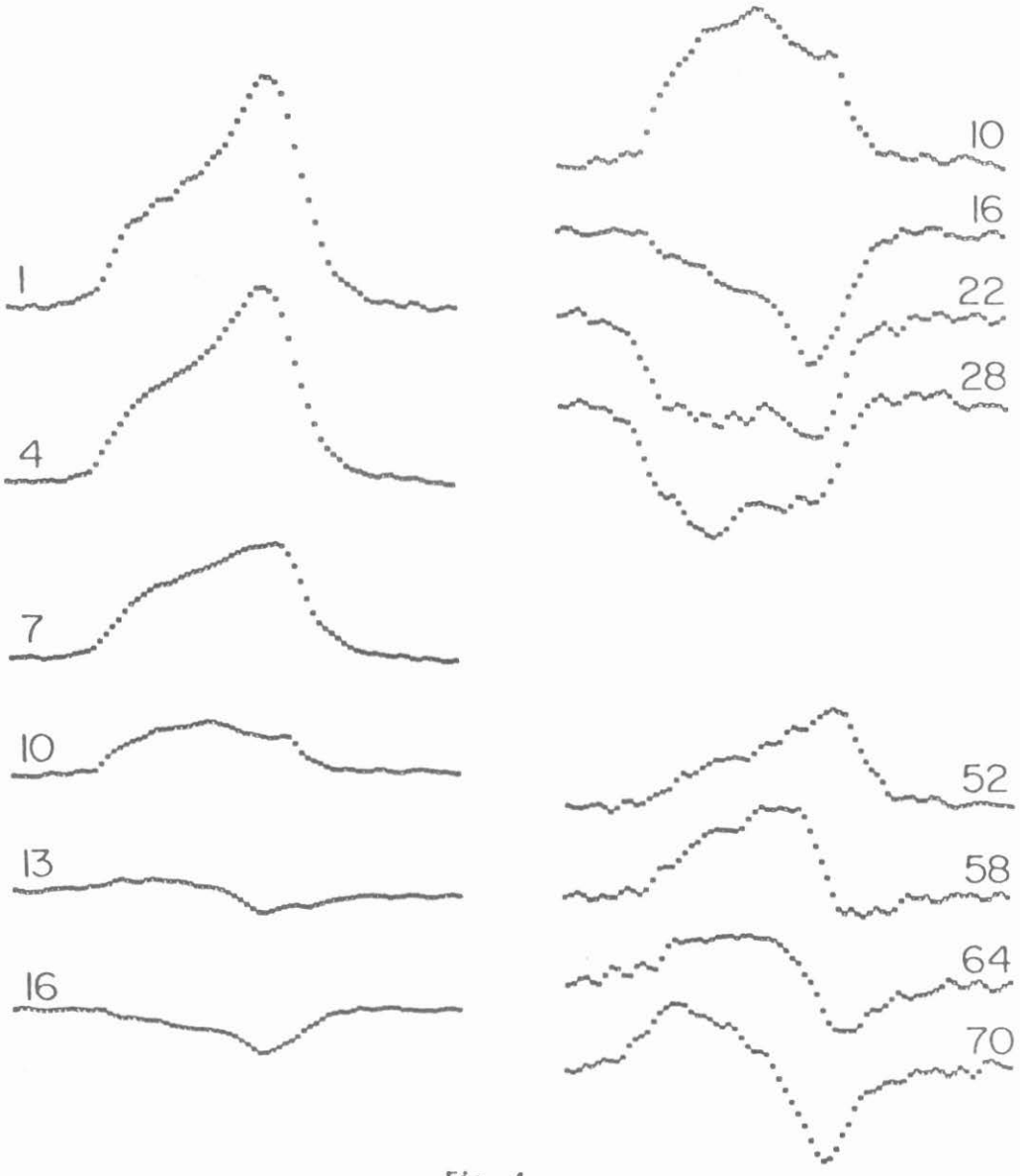

Fig. 4

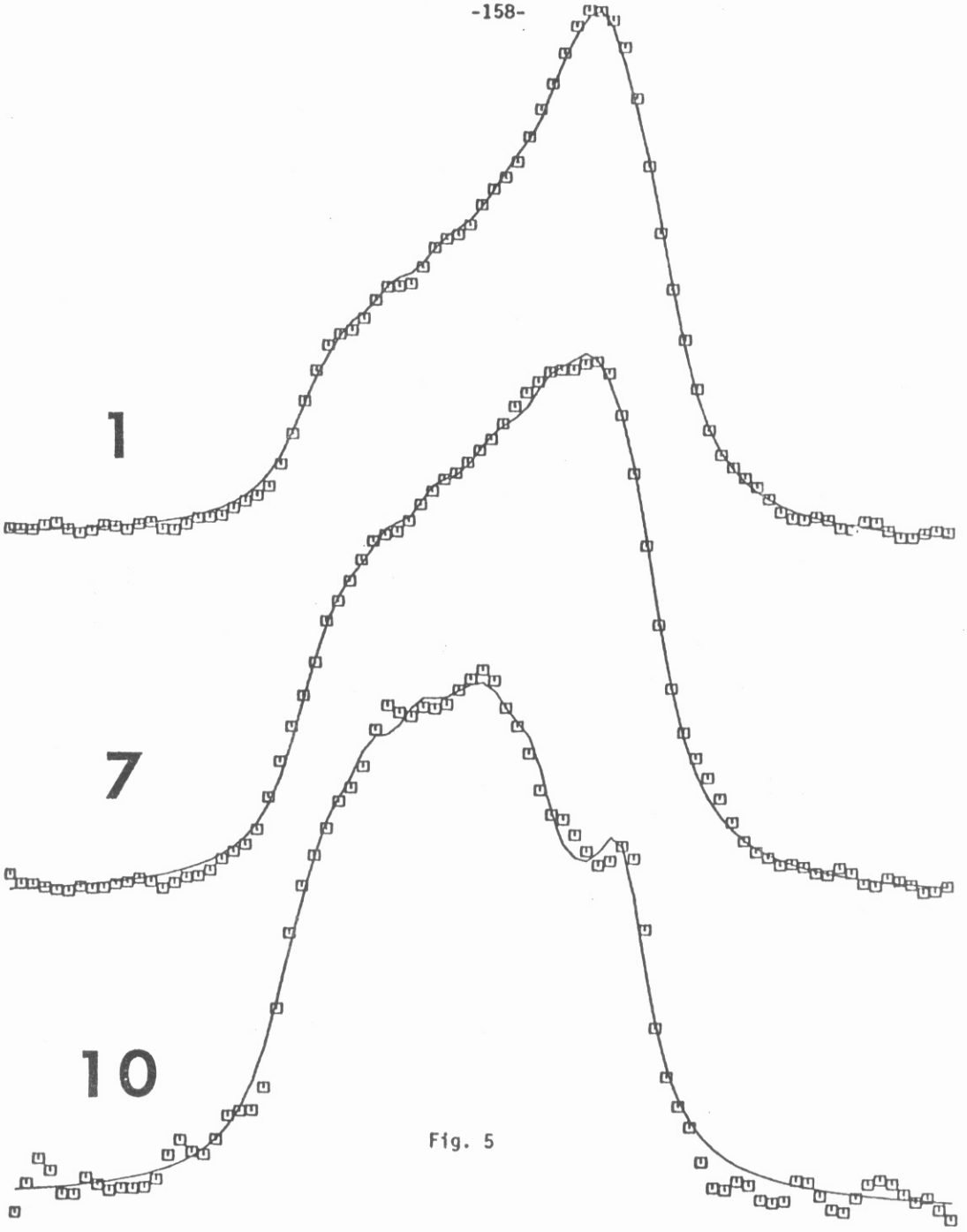

Fig. 5

CHAPTER 9

EXPERIMENTAL DETERMINATION OF THE ^{13}C CHEMICAL SHIFT TENSOR IN $K_2Pt(CN)_4Br_{0.3}\cdot 3H_2O$ USING HETERONUCLEAR DIPOLAR AND QUADRUPOLAR INTERACTIONS

(Chapter 9 is essentially an article by M. E. Stoll and R. W. Vaughan, R. B. Saillant and Terry Cole, entitled "^{13}C Chemical Shift Tensor in $K_2Pt(CN)_4Br_{0.3}\cdot 3H_2O$". This article was published in the Journal of Chemical Physics, Vol. 61, No. 7, p. 2896, October 1, 1974.)

We wish to report measurement of the ^{13}C chemical shift tensor within $K_2Pt(CN)_4Br_{0.3}\cdot 3H_2O$. Because of the anisotropy in its transport properties (it behaves as a one-dimensional conductor) this compound has been of considerable interest and has been the subject of numerous investigations (1). Controversy still exists over the mechanism responsible for the high conductivity in materials of this type, and knowledge of the carbon chemical shift tensor of the cyanide ligands can furnish information about the electronic structure of the platinum complex. In addition, although recently developed NMR techniques are being presently used to measure carbon chemical shift tensors in solids (2,3), there have been no reported measurements of transition metal complexes. The results reported here furnish information on the anisotropy in the electronic structure of the cyanide in this square planar platinum complex and can be compared, for example, with measurements of the ^{13}C chemical shift tensor in HCN.

In order to have sufficient sensitivity for conventional pulsed NMR studies, single crystals of the compound were grown from cyanide 60% enriched in ^{13}C by a process previously reported (4). Crystals grown by this method have been extensively analyzed and are well characterized (5). Spectra were obtained by conventional pulsed NMR at 14.2 MHz with some signal averaging ($\sim$ 500 scans per spectra). The crystal orientations were determined from the anisotropic optical properties of the crystal along with the NMR spectra.

X-ray studies by K. Krogmann and H. D. Hausen (6) have characterized the structure of this compound, and Figure 1 schematically illustrates the relevant part of the structure and identifies the orientations of the

coordinate systems used in this work. Due to a high degree of symmetry at each carbon site, one can fix the orientation of the principal axis of the chemical shift tensor (7) as indicated in Figure 1. The σ_{11} axis is taken parallel to the C-N bond axis, σ_{33} is parallel to the Pt-Pt axis, and σ_{22} is perpendicular to both σ_{11} and σ_{33}. The square planar platinum complexes are stacked in columns with the Pt atoms on the column axis to produce the solid structure. Each alternate layer, i.e. platinum complex, is rotated 45°, and since the crystal structure is tetragonal, there are two inequivalent carbons. K. Krogmann and H. D. Hausen (6) report C-N distances of 1.19 $\pm$ 0.12 Å for the cyanides parallel to the a or b axes and 1.13 $\pm$ 0.12 Å for those at 45° angles to the a and b axes. It was not possible to detect any differences in the chemical shift tensors of the two carbons, and analysis of the NMR spectra yields an effective C-N distance of 1.14 $\pm$ 0.01 Å, ignoring possible spin-spin interactions.

The NMR spectra exhibit, in addition to the desired chemical shift tensor, the effects of dipolar interactions between the various nuclei with non-zero magnetic moments. Since the ^{13}C-^{14}N and ^{13}C-^{195}Pt nearest neighbor dipolar interactions are by far the largest dipolar interactions present, they were treated explicitly and all other dipolar couplings were incorporated into a Gaussian broadening function.

The treatment of the ^{13}C-^{14}N dipolar interaction has some novel features not normally encountered and deserves some special discussion. The ^{14}N nuclei have electric quadrupole interactions in this material which are of comparable size to their Zeeman interactions. Consequently, there is an orientationally dependent mixing of the normal ^{14}N Zeeman eigenfunctions, and these new eigenfunctions must be used in calculating

the dipolar splitting of ^{13}C by the ^{14}N. One must solve for these new eigenfunctions by diagonalization of a combined Zeeman-quadrupolar Hamiltonian. This was done for the case of an axially symmetric electric field gradient with its symmetry axis along the C-N bond. A value of e^2qQ of 3.467 MHz for the quardupole interaction was obtained from the work of Ikeda et al. (8) on a similar compound, $K_2Pt(CN)_4 \cdot 3H_2O$. Thus the Hamiltonian given in Equation 1 was used to determine the ^{14}N energy levels as a function of the angle, η, between the magnetic field direction and the symmetry axis of the electric field gradient. The resulting energy levels are plotted in Figure 2a (solid lines) along with the levels for a pure Zeeman Hamiltonian (dotted lines), ignoring the quadrupolar interaction.

$$H_{ZQ} = -\gamma_N \hbar H_0 I_z + \frac{3}{4} e^2qQ \left\{ \left[I_Z^2 - \frac{1}{4}\left[I_+I_- + I_-I_+\right] \right] \frac{1}{3}\left(3\cos^2\eta - 1\right) + \left[I_+^2 + I_-^2\right]\frac{1}{4}\sin^2\eta + \left[I_+I_z + I_zI_+ + I_-I_z + I_zI_-\right]\frac{1}{4}\sin(2\eta) \right\} \quad (1)$$

Using the eigenfunctions of Equation 1, the ^{13}C energy level splittings expected from the ^{13}C-^{14}N dipolar interaction are calculated as a function of η, and these are plotted in Figure 2b (solid lines) along with splittings expected had there been no quadrupole effects on the ^{14}N (dotted lines). Equation 2 is the final expression needed to calculate the ^{13}C dipolar splittings caused by ^{14}N, where a, b, and c are the coefficients (determined from the Hamiltonian in Equation 1) for the nitrogen Zeeman states, $m_z = 1, 0, -1$ respectively.

$$\Delta E = + \frac{\gamma_c \gamma_N \hbar^2}{r_{cN}^3} \left\{ \left(a^2 - c^2\right)\left(1 - 3\cos^2\eta\right) - \frac{3\sqrt{2}}{2}(a + c)b \sin(2\eta) \right\} \quad (2)$$

A point to be noted in the derivation of Equation 2 is that one obtains a secular (first order) contribution from terms in the dipolar Hamiltonian which normally make no such contribution. That is, one normally expands the dipolar Hamiltonian into six terms, A-F (9), and in cases of unlike spins, one obtains a secular contribution from only the A term. However, since the appropriate ^{14}N levels are now linear combinations of the nitrogen Zeeman levels, two additional terms, C and D, make first order contributions as well. This accounts for the gross difference between the two solutions plotted in Figure 2b and illustrates how the presence of the nitrogen quadrupolar interaction produces large qualitative effects in the ^{13}C spectra. Note, for instance, that the solutions ignoring the effects of the nitrogen quadrupolar interaction always produce a symmetric triplet for the carbon spectra, while with the nitrogen quadrupolar interaction taken into account, one can obtain highly asymmetric doublets, and symmetric triplets at only three angles. It should also be pointed out that the dipolar interaction can only split the spectra, thus the center of mass of the spectra remains a function only of the chemical shift tensor.

Because 33.7% of the platinum nuclei are ^{195}Pt with a spin of 1/2, the effect of the ^{195}Pt-^{13}C dipolar interaction will be to generate a pair of satellite lines around each of the ^{14}N-^{13}C lines with approximately 1/4 the intensity of the main line. Thus the final ^{13}C spectra consists of peaks, the center of mass of which are determined by the chemical shift tensor, and which are split according to the solid lines in Figure 2b with, in addition, a pair of satellite lines around each of the ^{13}C-^{14}N lines caused by ^{13}C-^{195}Pt dipolar interactions. The position of the platinum split lines was calculated using the reported (6) C-Pt distance.

To obtain a spectrum for comparison with experimental data,it is then necessary to add the appropriate chemical shift, σ (Equation 3) (9), to the calculated dipole split spectrum and to then superimpose such spectra for each carbon in the structure. The chemical shift can be expressed in terms of three principal values, σ_{11}, σ_{22} and σ_{33} and the angles, θ and ϕ, which specify (see Figure 1) the orientation of the magnetic field.

$$\sigma = \sigma_{33}\cos^2\theta + \sigma_{22}\sin^2\theta\sin^2\phi + \sigma_{11}\sin^2\theta\cos^2\phi \qquad (3)$$

Figures 3a-f reproduce three of the experimental and calculated spectra. Although the procedure for determining the effects of dipolar interactions on the carbon spectra appear complex, there are few adjustable parameters in the final equations. The spectrum in Figure 3a (taken very close to $\theta = 0$) was used to determine: (A) σ_{33}, (B) the effective C-N interatomic distance (from the splitting of the two outside peaks), and (C) the effective line width (by adjustment until a fit with the spectra was obtained). All of the remaining two dozen spectra, taken as a function of θ and ϕ, were synthesized by adjusting <u>only</u> the remaining two components of the chemical shift tensor, σ_{22} and σ_{11}. Good qualitative agreement between experimental and calculated spectra were obtained in all cases,thereby furnishing strong justification for the validity of the analysis presented here. Figures 3c-f have been included to give some feeling for how sample rotation affects the observed spectra. The asymmetric nature of the spectra generated by the presence of the ^{14}N quadrupolar interaction is evident in Figure 3c, while the asymmetry in Figure 3e is being generated by the large difference in the chemical shift components σ_{11} and σ_{22} as well as ^{14}N quadrapolar effects.

Because of the sensitivity of the NMR spectra to the value given the C-N interatomic distance and the fact that the x-ray values contain rather large error limits, an effective value for the C-N distance was determined from the spectra in Figure 3a and used in all remaining spectral calculations. This value of 1.14 $\pm$ 0.01 Å is more precisely known than the x-ray values; however, it may be in error due the presence of anisotropy in electronically coupled spin-spin interactions (9), which have been ignored in this analysis.

The values obtained for the principal values of the carbon chemical shift tensor are σ_{11} = + 261 $\pm$ 10 ppm, σ_{22} = - 48 $\pm$ 10 ppm, and σ_{33} = - 10 $\pm$ 5 ppm, relative to the carboxyl carbon in a concentrated acetic acid solution. This gives an isotropic average, $\bar{\sigma}$ of 68 ppm, an anisotropy, $\Delta\sigma = \sigma_{11} - \frac{1}{2}\left(\sigma_{22} + \sigma_{33}\right)$ of 290 ppm, and an asymmetry, $\left(\sigma_{33} - \sigma_{22}\right)/\left(\sigma_{11} - \bar{\sigma}\right)$, of 0.2. The isotropic value is the same, within the accuracy of the measurement, to the trace value of HCN (10), and liquid crystal measurements of the HCN carbon chemical tensor have yielded an anisotropy of 280 $\pm$ 20 ppm (11) which is equivalent to the value reported here. Thus, the effect of the cyanide bonding to the platinum, and all associated effects due to the particular solid state structure, primarily affect the carbon chemical shift tensor by producing a nonzero asymmetry (0.2) around the C-N bond.

REFERENCES

1. For review articles see K. Krogmann, Angew. Chem. Internat. Edit. 8, 35 (1969); I. F. Shchegolev, Phys. Status Solidi (a) 12, 9 (1972); H. R. Zeller, in "Festkorperprobleme" (Ed. by H. J. Queisser) Pergamon Press (1973), Vol. 13, New York; J. Miller and A. Epstein, Prog. in Inorg. Chem. 20 (1975).

2. A. Pines, M. G. Gibby, and J. S. Waugh, J. Chem. Phys. 56, 1776 (1972); Chem. Phys. Letters 15, 373 (1972); J. Chem. Phys. 59, 569 (1973); C. S. Yannoni and H. E. Bleigh, J. Chem. Phys. 55, 5406 (1971); C. S. Yannoni, J. Chem. Phys. 58, 1773 (1973); P. Mansfield and P. V. Grannall, J. Phys. C. 4, L197 (1972); J. Phys. C. L226 (1972); P. K. Grannell, P. Mansfield, and M. A. B. Whitaker, Phys. Rev. B8, 4149 (1974).

3. R. W. Vaughan, "Annual Reviews in Materials Science" (Ed. by R. A. Huggins, R. H. Bube, R. W. Roberts), Vol. 4 (1974), Annual Reviews, Palo Alto, and references therein.

4. R. B. Saillant, R. C. Jaklevic, and C. D. Bedford, Materials Research Bulletin 9, 289 (1974).

5. R. B. Saillant, R. C. Jaklevic and J. Jaklevic, in preparation for Materials Research Bulletin.

6. K. Krogmann and H. D. Hausen, Z. Anorg. Allg. Chem. 358, 67 (1968).

7. A. D. Buckingham and S. M. Malin, Mol. Phys. 22, 1127 (1971).

8. R. Ikeda, D. Nakamura, and M. Kubo, J. Phys. Chem. 72, 2982 (1968).

9. A. Abragam, "The Principles of Nuclear Magnetism", Oxford University Press, London (1961).

10. J. B. Stothers, "Carbon-13 NMR Spectroscopy", Academic Press, New York, 1972; G. A. Olah and T. E. Kiowsky, J. Am. Chem. Soc. 90, 4666 (1968).

11. F. Millett and B. P. Dailey, J. Chem. Phys. 54, 5434 (1971).

FIGURE CAPTIONS

Figure 1 A portion of the structure of $K_2Pt(CN)_4Br_{0.3}\cdot 3H_2O$ is illustrated, as determined by K. Krogmann and H. D. Hausen (6). The principal axes for one of the carbon atoms is illustrated, as is the nomenclature (θ and ϕ) used to specify the crystal orientation with respect to the external magnetic field, H_0.

Figure 2(a) The energy levels for ^{14}N are shown as a function of η (the angle between the Zeeman axis and the symmetry axis of the quadrupole tensor). The solid lines are the levels determined for the combined Zeeman-quadrupolar Hamiltonian, while the dashed lines are the levels for a pure Zeeman interaction. (One vertical unit equals $3e^2qQ/4 = 2.60$ MHz).

(b) The dipolar splitting of the carbon by the nitrogen is shown as a function of η (note that the symmetry axis of the nitrogen quadrupole interaction was assumed to be parallel to the C-N internuclear vector). The solid lines were obtained by using the combined Zeeman-quadrupolar Hamiltonian for the nitrogen, while the dashed lines were obtained by assuming the nitrogen states were determined from a pure Zeeman Hamiltonian. (One vertical unit equals $\gamma_C\gamma_N\hbar^2/\left(r^3_{CN}\right) = 1.48$ kHz.)

Figure 3 Comparison of experimental and theoretical ^{13}C spectra. The vertical scale is arbitrary but the same for all spectra, and the horizontal scale is 3.91 kHz per division. The dashed vertical line represents the location of the carboxyl carbon in CH_3COOH which was used as a reference. Figures (a) and (b) are the corresponding experimental and calculated spectra for $\theta = 3^{\circ}$ and $\phi = 0^{\circ}$, Figures (c) and (d) are the corresponding experimental and calculated spectra for $\theta = 30^{\circ}$ and $\phi = 0^{\circ}$, while Figures (e) and (f) are the corresponding experimental and calculated spectra for $\theta = 90^{\circ}$ and $\phi = 22.5^{\circ}$.

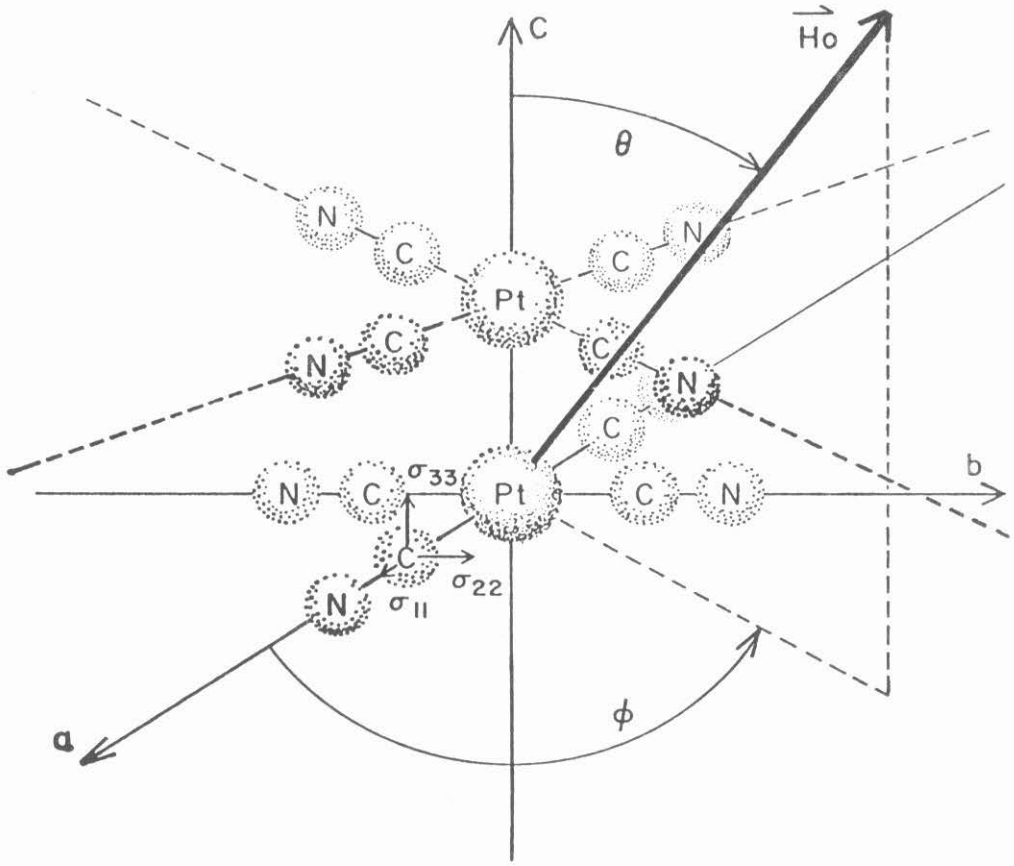

Fig. 1

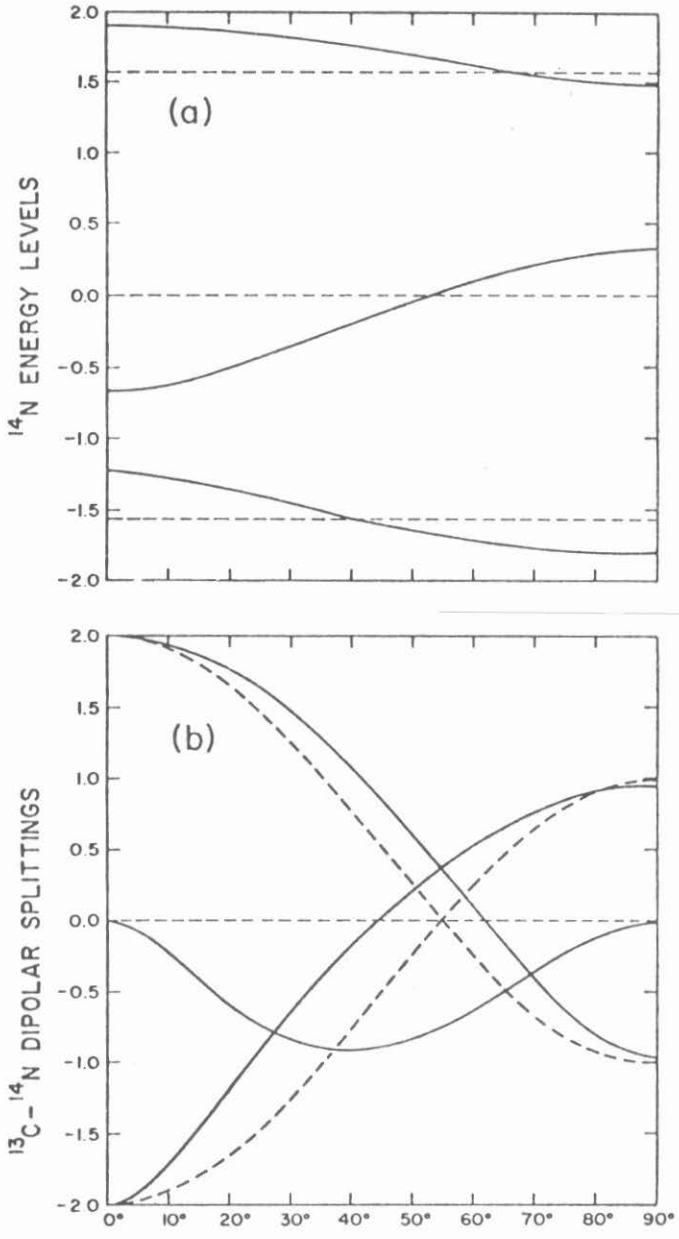
(a)
^{14}N ENERGY LEVELS
2.0
1.5
1.0
0.5
0.0
-0.5
-1.0
-1.5
-2.0
(b)
^{13}C-^{14}N DIPOLAR SPLITTINGS
0°
10°
20°
30°
40°
50°
60°
70°
80°
90°

Fig. 2

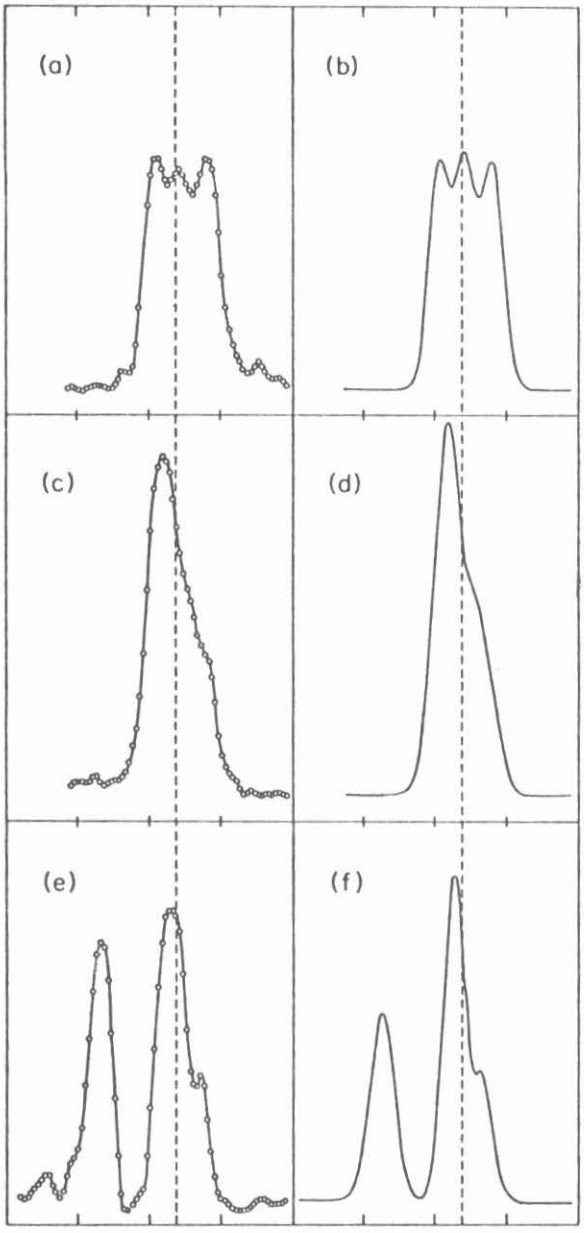

Fig. 3

APPENDIX

A SIMPLE SINGLE-COIL NUCLEAR MAGNETIC DOUBLE RESONANCE PROBE FOR SOLID STATE STUDIES

(The Appendix is essentially an article by M. E. Stoll, A. J. Vega, and R. W. Vaughan, entitled "A Simple Single-Coil Double Resonance NMR Probe for Solid State Studies". This article has been accepted for publication in Reviews of Scientific Instruments.)

I. Introduction

A critical element of a pulsed nuclear magnetic resonance (NMR) spectrometer suitable for work in solids is the sample probe, a unit designed for application of intense rf magnetic fields to the sample and for detection of the resulting weak rf magnetic fields generated by the sample. This paper will describe a single coil, double resonance sample probe which has been used for a variety of NMR experiments, including both high resolution solid state studies[1,2,3] and liquid studies[4]. While primarily designed for these experiments, which require the generation of rf fields in the sample with rotating components of ~50 gauss amplitude at two different frequencies simultaneously, as well as the ability to observe weak NMR signals at both frequencies, this probe should be useful for a wide variety of solid state double resonance experiments[5-10].

Since the probe characteristics often set the practical limitations on the performance of an NMR spectrometer, there have been numerous discussions of probe design in the literature in recent years[11-22], and we will limit our discussion to a presentation of the criteria needed for the recently developed solid state, double resonance experiments and a discussion of a particular design we have found convenient and satisfactory over a wide frequency range (from 12-270 MHz). This design is useful when the two rf frequencies are sufficiently separated (a factor of four in our experiments).

II. The Sample Probe

The high resolution, solid state double resonance NMR schemes developed require: (a) the generation of rf field strengths of near 50 gauss in the rotating frame at each of two widely separated frequencies, (b) a low degree of rf field inhomogeneity (less than 0.5% over the sample volume) at both frequencies, (c) the spatial pattern of rf field inhomogeneity within the

coil to be identical at both frequencies, and (d) the capability of detecting microvolt-level signals in the solid at each of the rf frequencies while subjecting, or within several microseconds after subjecting, the solid to a high-level (100 watt) irradiation at the second frequency. Essentially, all of these criteria are most easily satisfied by using a single coil for transmitting and receiving both frequencies[11-22], although it does require some electronic means of isolating, or separating, the two frequencies. A single coil configuration is particularly compatible with the restricted space available in the high field magnets.

The design we have found most useful is illustrated in Figure 1. A piece of coaxial cable, one-fourth of a wavelength ($\lambda/4$) at the higher frequency serves a critical isolation role[15,23] by enabling the single coil L to be the inductance in two resonance circuits, each of which can be tuned and impedance matched at its own frequency. It also prevents high-frequency power loss into the low-frequency source while the loss of low-frequency power into the high-frequency source is prevented by keeping C_3 small. This system allows both frequencies to have high Q response and yet furnishes the needed frequency isolation. This scheme has been used over the past two years at a variety of frequencies, and the detailed discussion of the probe circuit will be divided into two sections: one to describe the lower frequency version used for ^{13}C (14.2 MHz) - ^{1}H(56.4 MHz) and ^{207}Pb(12.5 MHz) - ^{19}F(56.4 MHz) double resonance in 14 kilogauss fields, and the other to describe the high-frequency version for ^{13}C(68MHz) - ^{1}H(270 MHz) experiments in a 63-kilogauss superconducting magnet.

A rather standard system of equations needs to be solved to estimate the component values for a particular case. Tuning and impedance-matching conditions

on the low-frequency circuit require, respectively:

$$\frac{1}{\omega_\ell C_1} + \frac{1}{\omega_\ell C_2} \sim \omega_\ell L \tag{1}$$

$$\frac{1}{\omega_\ell C_2} \sim \sqrt{R\ R_{o\ell}} \tag{2}$$

and similar conditions for the high-frequency circuit require:

$$\frac{1}{\omega_h C_3} + \frac{1}{\omega_h C_4} \sim \omega_h L \tag{3}$$

$$\frac{1}{\omega_h C_4} \sim \sqrt{R\ R_{oh}} \tag{4}$$

ω_ℓ and ω_h are the low and high frequencies in radians per second; $R_{o\ell}$ and R_{oh} are the desired input impedances; and R is the effective series resistance of the coil. These equations were obtained from an essentially zeroth order approximation that involves ignoring small residual effects of C_1 and C_2 on the high-frequency response and of C_3 and C_4 on the low-frequency response of the probe. As long as the inequalities

$$R_{oc}{}^2 \omega_h C_2 >> \omega_h L \tag{5}$$

$$C_1, C_2 >> C_3 \tag{6}$$

(where R_{oc} is the coaxial cable characteristic impedance)

are maintained, this appears to be an adequate description, particularly since one must expect that the effective, in circuit, values will be affected (strongly at high frequencies) by the geometrical configuration of the probe, and thus the final values of all components must be empirically adjusted[24]. A proper choice of coil inductance, L, allows one to maintain inequalities, (5) and (6),

as long as the two frequencies are sufficiently different. The low-frequency impedance matching capacitor, C_2, and the high-frequency impedance matching capacitor, C_4, are shown as fixed capacitors since impedance matching is not so critical as to require continuously adjustable capacitors at those points, and the practice was to add in parallel small fixed ceramic capacitors[25] to arrive within a few percent of the desired impedance. C_1 served as the low-frequency tuning capacitor while C_3 maintained the high-frequency tuning condition, and although both capacitors affect the tuning of both high and low frequency resonance, the large difference in the size of the capacitors $C_1/C_3 \sim \omega_h^2/\omega_\ell^2$ allowed nearly independent tuning. Point B is the high-impedance (high voltage) point for the higher frequency, while point D is the high-impedance point for the lower frequency, and, consequently, both capacitors C_1 and C_3 must be able to withstand the several kilovolts present at 100 watts of applied rf power.

A. Low-Frequency Version

For the situation where the probe was tuned for $\frac{\omega_\ell}{2\pi}$ = 14.2 MHz and $\frac{\omega_h}{2\pi}$ = 56.4 MHz and with R_{oh} = 200 Ω and $R_{o\ell}$ = 50 Ω, we obtained a circuit with Q_h = 80, and Q_ℓ = 60 when we used a solenoidal sample coil 1.5 cm long and 6 mm in diameter consisting of 14 turns of flattened #20 copper wire (measured inductance of 0.36 μH). The nominal (low-frequency) values of the capacitors used were: C_1 = 230 pf, C_2 = 820 pf, C_3 = 28 pf, and C_4 = 94 pf. The actual effective, in circuit, values of these capacitive elements differed substantially, particularly for the larger values of capacitance, from the nominal values as can be seen in comparing the reported values with the results of Equations 1-4.

The coil was designed to both furnish the desired inductance, L, and an intense, uniform H_1 field (H_1 inhomogeneity was measured to be 0.3% over a 4 mm diameter spherical sample, and with 100 watts of input power on both high and low frequencies, H_1 field strengths of 50 gauss were obtainable).

This version of the probe was designed for operation within a 4.8 cm wide gap of a conventional electromagnet, and consequently, no severe space problems

were encountered, and it was possible, for example, to use a conventional variable vacuum capacitor as part of C_1. A simple variable ceramic trimmer in parallel with a fixed ceramic capacitor was used for C_3. Temperature regulation capability was obtained by encasing the sample coil in a glass dewar (unsilvered) and simply passing the coil leads through the dewar walls. In addition, the probe was designed for use with an already existing rotational device for use in single crystal studies.

It was found necessary to take care to remove all dielectric materials containing protons when the proton signal was to be observed. In particular, a teflon dielectric $\lambda/4$ cable was used in this case, and likewise when the fluorine signal was to be observed, no fluorine-containing material was allowed as a dielectric.

B. High-Frequency Version

Because of the inherent difficulty of working with the high rf frequency used in this version (270 MHz), special care had to be taken in the physical construction of the probe and its components to avoid additional and undesirable inductances and capacitances. The solenoidal sample coil was again constructed from flattened copper wire (#16 flattened to a width of 2 mm) which was wound into a 9-turn, 1.4 cm long coil of 6 mm diameter. The measured inductance of the coil was near 0.16 μH and stayed frequency independent to well beyond 270 MHz. The high-frequency tuning and impedance-matching capacitors C_3 and C_4 were combined into a single cylindrical unit which is illustrated in Figure 2. The capacitor C_3 was formed by the central copper rod (which is connected directly to the coil at point B) and the adjustable inner cylinder. This capacitor has a restricted, but usable tuning range of from 1.5 to 3.5 pf. The capacitance between the outer two cylinders is near

40 pf, and since the outer cylinder is grounded, it constitutes the main part of the matching capacitor, C_4. Final adjusting of C_4 was accomplished by adding small fixed ceramic capacitors[25] between point C and the outer cylinder. This geometrical configuration allowed effective shielding of the bulky C_3 capacitor and furnished a low inductance ground connection between the incoming cable shielding and the ground side of the coil L (the incoming cable was soldered to the bolt at point C and the ground to the outer cylinder at that point). In this geometry it was necessary to add 36 pf of additional capacitance between point C and the outer cylinder for a 50 ohm impedance match with the incoming 270 MHz signal. For capacitor C_1 a variable capacitor identical in construction to that used for the C_3 part of the cylinderical unit illustrated in Figure 2,was used with additional fixed ceramic[25] capacitors in parallel to give a total capacitance of 32 pf. The $\lambda/4$ cable was a teflon-dielectric coaxial cable. The low-frequency matching capacitor, C_2, was large, 350 pf, and care had to be taken in its placement in order to maintain its value because even short leads could add sufficient inductance to alter its impedance radically. The exact length of the co-axial cable was determined experimentally such that the connection of the cable did not change the resonance frequency of the 270 MHz portion of the probe. With the $\lambda/4$ cable disconnected the Q of the 270 MHz resonant circuit was 300, and upon connection of the $\lambda/4$ cable, this figure dropped to 150. The Q of the 67.9 MHz portion was measured to be near 80, and no measurable power loss could be attributed to the $\lambda/4$ cable at this frequency.

The application of 330 watts of 270 MHz power was required to produce H_1 field strengths of 33 gauss, indicating some additional loss mechanism still unaccounted for in comparison to the low-frequency version. It was found necessary to use three ceramic capacitors[25] in series for the padding capacitor in parallel with the adjustable portion of C_1 since the application of 300 watts was sufficient to cause arcing across a single capacitor in this position.

III. Operational Characteristics

The actual operational configuration for the probe is illustrated in Figure 1. A power-activated diode (PAD) switch[26] was used to couple the transmitter and receiver to the probe circuit for the lower frequencies, and a $\lambda/4$ arrangement[14,22] was used for coupling at the higher frequency. Commercially available filters[27] were used at the probe inputs as illustrated in Figure 1. A wideband receiver (5-300 MHz), which has been previously described[28], was used for observing both frequencies by simply connecting the appropriate signal line to the receiver. The ability to use the same wideband receiver for both high and low frequency signals emphasizes the frequency isolation obtained with the combination of probe and commercial filters.

The probe was operated in two modes. In one case it was necessary to observe one frequency in the midst of a complex pulse cycle where, during a window of a few microseconds, no rf was being applied at either frequency. In this case the commercial filters were not used since they hindered recovery times. A 100-watt signal applied to either input of the probe resulted in a 10-15 volt peak-to-peak leakage signal at the opposite input, and this was

further reduced to less than one volt by the time it arrived at the receiver. The receiver was designed to handle volt-level transients[28], and signals could be observed, for example, from either protons or carbon-13 in the normal 4 microsecond sampling window of the eight-pulse cycle with a cycle time of 48 microseconds. In the second mode, it was necessary to observe one signal while simultaneously applying high rf power to the probe at the second frequency. The use of both of the commercial filters was necessary in this case in order to: (a) protect the receiver from overloading due to the high power rf signal at the second frequency, and (b) prevent the high-power input signal from containing any rf component at the detection frequency (once a signal of this sort reached the probe, it could not be removed by any filtering without also filtering out the NMR signal to be observed).

An example of the performance of the probe in this second mode is illustrated in Figure 3, which is an oscilloscope photograph of the ^{207}Pb NMR signal observed in PbF_2, with (bottom) and without (top) decoupling the ^{19}F. In the upper trace no fluorine decoupling power has been applied and the ^{207}Pb signal decays too rapidly (due to heteronuclear dipolar interactions) to be observed on this timescale (5 msec total scan), while in the lower trace fluorine decoupling power has been applied and the ^{207}Pb signal is clearly visible. One notes that the presence of the high-power level of fluorine irradiation has not produced any noticeable increase in the noise observed at the ^{207}Pb frequency. Other examples of the quality of data obtained can be found in recently published papers[2,3,4].

References

1. M. E. Stoll, W-K. Rhim, and R. W. Vaughan, J. Chem. Phys. 64, 4808 (1976).
2. M. E. Stoll, A. J. Vega, and R. W. Vaughan, J. Chem. Phys. 65, 4093 (1976).
3. M. E. Stoll, A. J. Vega, and R. W. Vaughan, Proceedings of the XIXth Congress Ampere, Heidelberg, Germany, 1976. In press.
4. M. E. Stoll, A. J. Vega, and R. W. Vaughan, submitted for publication.
5. M. Mehring, "High Resolution NMR Spectroscopy in Solids," Volume 11, pp. 1-246. NMR Basic Principles and Progress (Eds.: P. Diehl, E. Fluck, R. Kosfeld), Springer-Verlay, New York, 1976.
6. W. P. Aue, E. Bertholdi, and R. R. Ernst, J. Chem. Phys. 64, 2229 (1976).
7. L. Müller, A. Kumar, T. Baumann, and R. R. Ernst, Phys. Rev. Lett. 32, 1402 (1974).
8. M. Alla and E. Lippmaa, Chem. Phys. Letters 37, 260 (1976).
9. R. K. Hester, J. L. Ackerman, V. R. Cross, and J.S. Waugh, Phys. Rev. Letters 34, 993 (1975); J. Chem. Phys. 63, 3606 (1975).
10. R. K. Hester, J. L. Ackerman, B. L. Neff, and J. S. Waugh, Phys. Rev. Letters 36, 1081 (1976).
11. W. G. Clark, Rev. Sci. Instrum. 35, 316 (1964).
12. W. G. Clark and J. A. McNeil, Rev. Sci. Instrum. 44, 844 (1973).
13. I. J. Lowe and M. Engelsberg, Rev. Sci. Instrum. 45, 631 (1974).
14. I. J. Lowe and C. E. Tarr, J. Phys. E1, 320 (1968).
15. V. R. Cross, R. K. Hester, and J. S. Waugh, Rev. Sci. Instrum. 47, 1486 (1976).

16. J. D. Ellett, M. G. Gibby, U. Haeberlen, L. M. Huber, M. Mehring, A. Pines, and J. S. Waugh, Advances in Magnetic Resonance (Ed.: J. S. Waugh). Vol. V, p. 117, Academic Press, New York, 1971.

17. K. W. Gray, W. N. Hardy, and J. D. Noble, Rev. Sci. Instrum. 37, 631 (1966).

18. R. A. McKay and D. E. Woessner, J. Sci. Instrum. 43, 838 (1966).

19. N. Trappeniers, N. J. Gerritsma, P. H. Oosting, Physica 30, 997 (1964).

20. M. Mansfield, J. G. Powles, J. Sci. Instrum. 40, 232 (1963).

21. I. J. Lowe and D. E. Barnaal, Rev. Sci. Instrum. 34, 143 (1963).

22. U. Haeberlen, Ph.D. Thesis, Tech. Hochschule, Stuttgart, 1967.

23. The use of a $\lambda/4$ cable for frequency isolation within the probe was initially suggested to us by Prof. M. Mehring (unpublished material).

24. Empirical characterization of circuit behavior was accomplished with a Hewlett-Packard impedance meter below 100 MHz and a vector voltmeter (Model 8405A) above 100 MHz.

25. American Technical Ceramics, 1 Norden Lane, Huntington Station, New York, high voltage ATC Model B capacitors.

26. J. E. Piott, D. L. Husa, and M. Lipsicas, submitted for publication.

27. Cir-Q-tel Inc., 10504 Wheatley Street, Kensington, Maryland 20795.

28. R. W. Vaughan, D. D. Elleman, L. M. Stacey, W.-K. Rhim, and J. W. Lee, Rev. Sci. Instrum. 43, 1356 (1972).

Figure Captions

Figure 1: (A) Schematic diagram of double resonance probe. The high-frequency connection is at point C , while the low-frequency connection is at point A . Inductor, L, represents the sample coil, R represents losses in the coil and remaining circuit, and ℓ is the length ($\lambda/4$ at the high frequency) of a piece of coaxial cable.

(B) Connection of probe to receiver and transmitter. The optional filters (F_l and F_h) are shown with dotted outline, and the connection of either frequency to the broadband receiver is made through a conventional $\lambda/4$ arrangement or a PAD switch (P).

Figure 2: Cross section of unit which comprises capacitors C_3 and C_4 in higher frequency version of probe. Points B and C correspond to those in Figure 1. Respective diameters are: a = 0.32 cm, b = 1.11 cm, c = 1.59 cm, d = 2.22 cm, e = 2.38 cm, and f = 0.64 cm. A similarly constructed unit, without the outer metal ground (d and e), served as the adjustable portion of capacitor C_1.

Figure 3: Free-induction decay of ^{207}Pb in solid PbF_2 without (top trace) and with (bottom trace) ^{19}F decoupling. The horizontal axis is 5 msec fullscale, and no ^{207}Pb NMR signal is observed in the top trace on this timescale due to heteronuclear dipolar broadening, while the decoupled ^{207}Pb signal is apparent in the lower trace. Comparison of the two traces shows no observable increase in the noise level on the 12.5 MHz channel (^{207}Pb) when high power is applied to the 56.4 MHz channel (^{19}F).

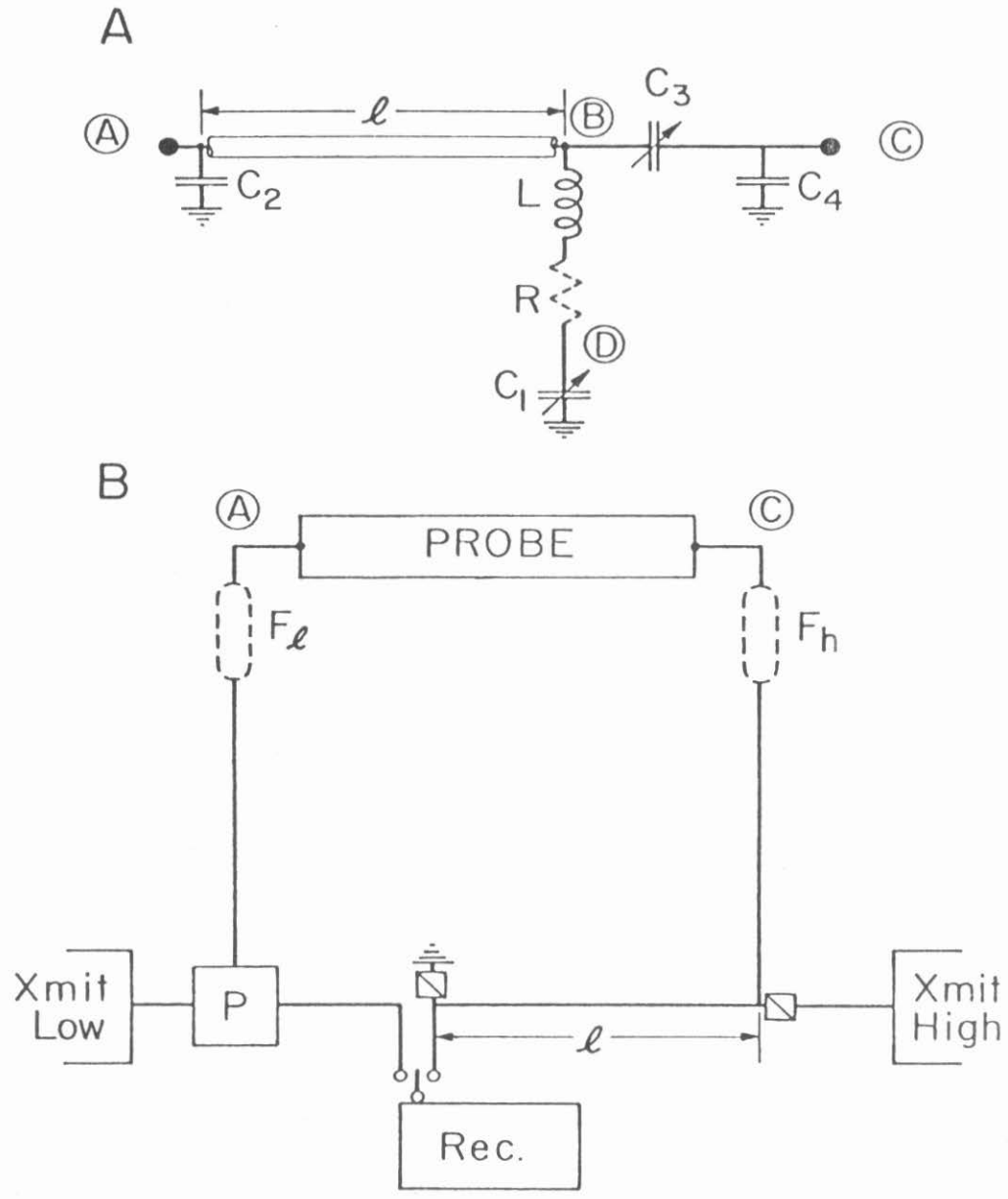

Fig. 1

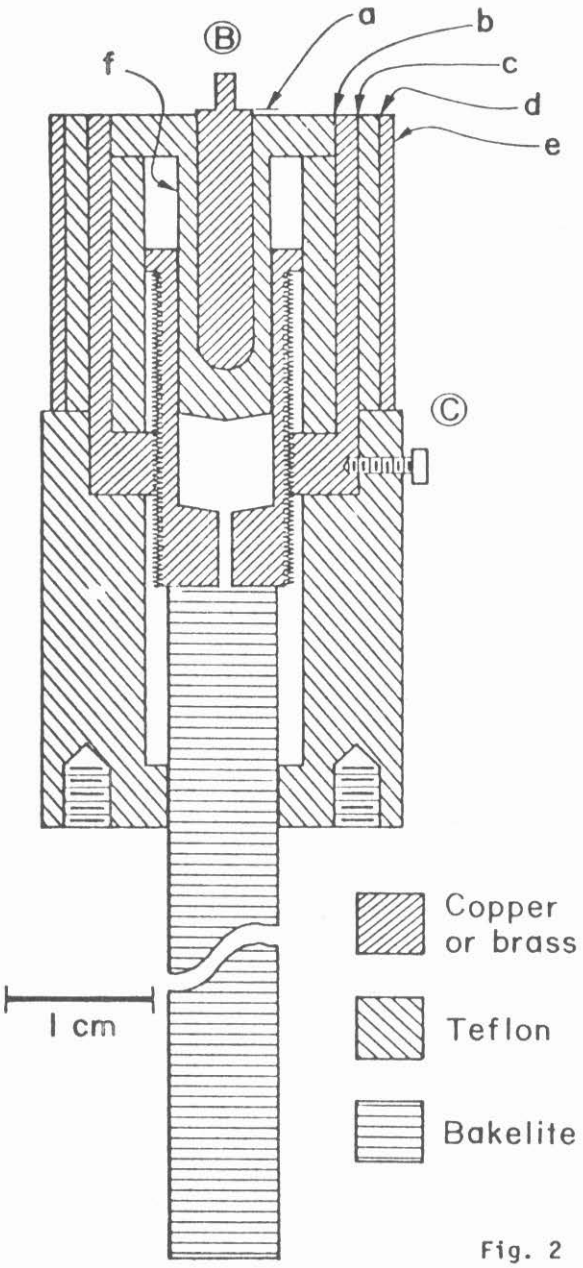

Fig. 2

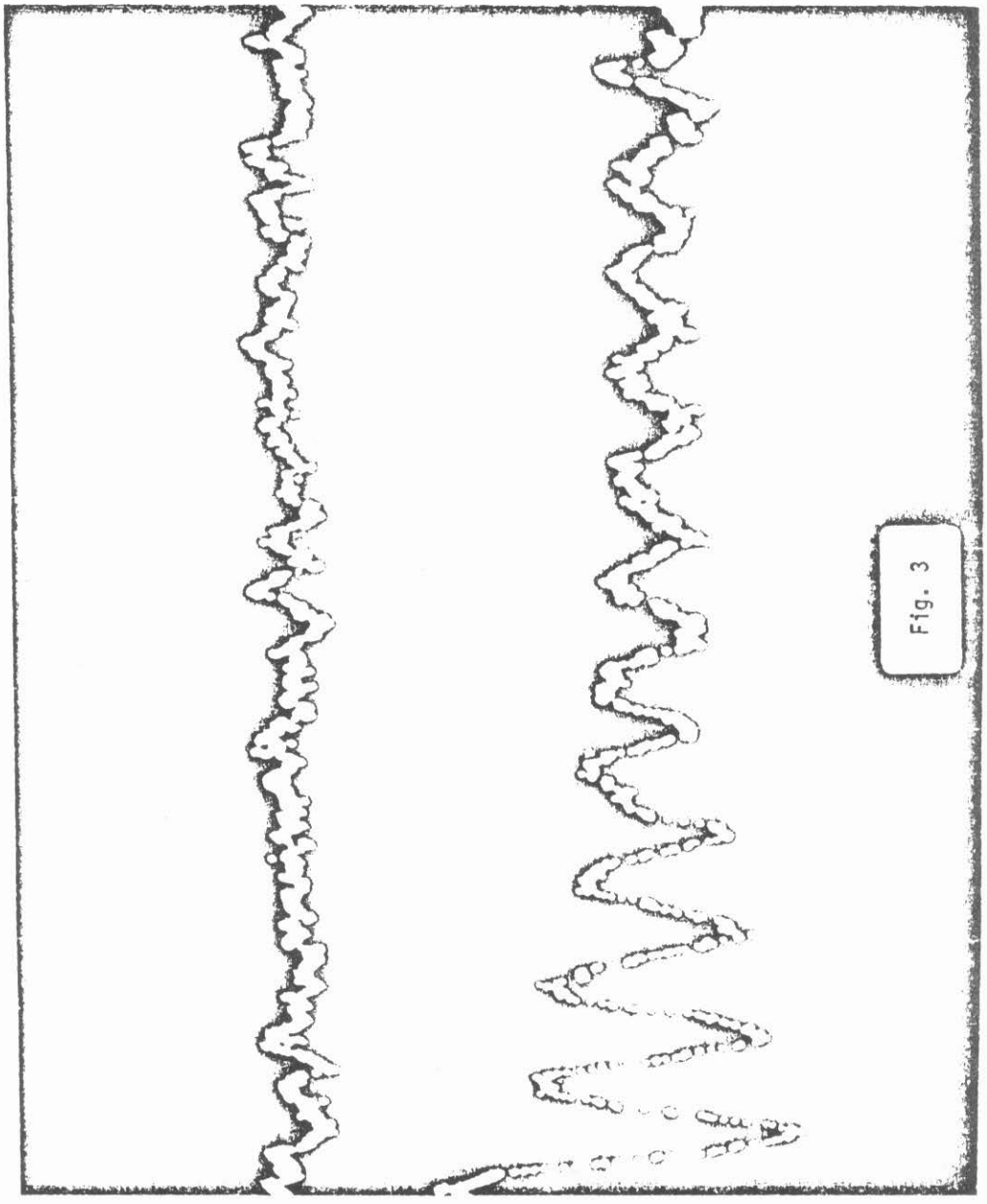

Fig. 3

THE END